REPUBLIQUE ALGERIENNE DEMOCRATIQUE ET POPULAIRE

MINISTERE DE L'ENSEIGNEMENT SUPERIEUR ET DE LA RECHERCHE SCIENTIFIQUE

Ecole Nationale Polytechnique

المدرسة الوطنية المتعددة التقنيات
Ecole Nationale Polytechnique

Département d'Electronique

MÉMOIRE de Magister

Option :
Systèmes d'analyse et traitement de signal

Par : Mr TOUHAMI Mohamed Seddik
Ingénieur d'Etat en électronique

Ecole Nationale Polytechnique (E.N.P) – Alger.

Estimation des directions d'arrivée dans le domaine temps-fréquence

Soutenu le 21 Mai 2007 devant un jury composé de :

Président :	H. BOUSBIA-SALAH	Maître de conférences (ENP)
Rapporteur :	A. BELOUCHRANI	Professeur (ENP)
Examinateurs :	Z. TERRA	Chargé de cours (ENP)
	A. LABED	Chargé de cours (EMP)
	I. KACHA	Maître de conférences (ENP)

Promotion 2007
E.N.P. 10, Avenue Hassen-Badi, El Harrach, ALGER

DEDICATION

TO MY DEAR PARENTS
TO MY BROTHERS AND SISTERS
TO ALL MY FRIENDS

ACKNOWLEDGEMENTS

All praise is due to Allah, the Almighty and the Most Gracious, the Most Merciful for providing me his guidance, help and blessings.

In the completion of this work, a number of people rendered invaluable assistance and support and I would like to hereby acknowledge such aid.

Unending gratitude goes to my supervisor, Pr. Adel BELOUCHRANI who gave me the benefit of his considerable experience, patience and invaluable advice.

I would also thank a great number of friends and colleagues: Ali, Allaoua, Amine, Muslem, Lani, Youcef and surely others for their support, encouragement and love.

Finally, I would like to thank my parents, brothers and sisters for supporting me all along in my studies and for really helping me finalize this work. Studying has been a big project for me, and definitely would not have been possible without you. I owe you a lot.

ملخص

هذا العمل يتطرق الى تقدير زوايا الوصول الذي يعتبرذا اهمية بالغة في ميدان معالجة الاشارة المعاصراذ له تطبيقات في انظمة الرادار, السونار, الاتصالات المتنقلة, معالجة الاشارات الفلكية, التشخيص الطبي, المراقبة الالكترونية...الخ. نهتم باستعمال التوزيعات الزمنية التواترية في هذا التقدير وذلك عن طريق استغلال خصائصها المفيدة في تحليل الاشارات غير المستقرة. تحديدا نتعرض لادخال المفهوم الزمني التواتري الى طرق التقديرالموجودة كما نتطرق الى الطرق المستعملة في كشف و تجميع auto-terms وcross-terms. نستعمل المحاكات لقياس اداءات الخوارزميات المقترحة بمقارنتها مع الطرق الموجودة وحد Cramer-Rao.

كلمات مفتاحية: زوايا الوصول, توزيع Wigner-Ville ,MUSIC , Min-Norm ,ESPRIT ,ML ,SSF, الزمني التواتري, auto- and cross-terms, joint block-diagonalisation , bootstrap.

Abstract

This work deals with the estimation of directions of arrival which is a key problem in modern signal processing and has found applications in radar, sonar, mobile communications, radio astronomy, medical diagnostic, electronic surveillance…etc. We are interested in the use of quadratic time-frequency distributions in this estimation through the exploitation of their interesting properties for the analysis of nonstationary signals. It is about the introduction of time-frequency concept to the existing estimators, the examination of the methods used for the incorporation and detection of auto- and cross-terms. Simulations are used to asses the basic performances of the presented algorithms through comparison with the existing ones and Cramer-Rao bound.

Keywords: directions of arrival, MUSIC, Min-Norm, ESPRIT, ML, SSF, time-frequency, Wigner-Ville distribution, auto- and cross-terms, joint block-diagonalisation, bootstrap.

Résumé

Ce travail traite l'estimation des directions d'arrivée, un problème central du traitement de signal moderne rencontré dans les domaines du radar, sonar, communications mobiles, radio astronomie, diagnostic médical, surveillance électronique…etc. On s'intéresse à l'utilisation des distributions temps-fréquence quadratiques dans cette estimation en profitant de leurs propriétés intéressantes dans l'analyse des signaux non stationnaires. Il s'agit d'introduire l'aspect temps-fréquence aux estimateurs existants et examiner les méthodes d'intégration et détection des auto- et cross-termes. Les performances élémentaires des algorithmes présentés sont illustrées par des simulations à travers des comparaisons avec les méthodes existantes et la borne de Cramer-Rao.

Mots clés : directions d'arrivée, MUSIC, Min-Norm, ESPRIT, ML, SSF, temps-fréquence, distribution de Wigner-Ville, auto- et cross-termes, bloc-diagonalisation conjointe, bootstrap.

Notations and Abbreviations

$E\{.\}$	expectancy
L	number of sources
M	number of sensors
N	number of snapshots
P_D	probability of detection
P_{FA}	probability of false alarm
P_R	probability of resolution
$P_{CAP}(\theta)$	spectrum of Capon's beamformer
$P_{CF}(\theta)$	spectrum of the conventional beamformer
$Q_{MU}(z)$	MUSIC polynomial
SNR	signal to noise ratio
$\Im\{.\}$	imaginary part
$\Pi_{\mathbf{A}}^{\perp}$	orthogonal projection onto the null space of $\mathbf{A}^H$
$\Re\{.\}$	real part
$\mathbf{W}$	whitening matrix
$\mathbf{a}(\theta)$	steering vector
λ	wavelength
$\mathcal{FT}\{.\}$	Fourier transform
$\mathcal{H}[.]$	Hilbert transform
$\mathcal{R}(t,\tau)$	instantaneous autocorrelation function
ν	Doppler variable
$\odot$	Hadamard product
σ^2	variance
τ	delay
θ	angle of arrival
d	distance between two sensors of the antenna
f_c	central frequency
$sgn\{.\}$	sign
$\mathbf{A}(\theta)$	matrix of directions of arrival
$\mathbf{A}^{\dagger}$	Moore-Penrose pseudo-inverse of $\mathbf{A}$
$\mathbf{I}_M$	identity matrix of dimension M
$\mathbf{P}_{MN}(\theta)$	spectrum of Min-Norm algorithm

$\mathbf{P}_{MU}(\theta)$	MUSIC spectrum
$\mathbf{R_{nn}}$	autocorrelation matrix of noise
$\mathbf{R_{ss}}$	autocorrelation matrix of sources
$\mathbf{R_{xx}}$	autocorrelation matrix of snapshots
$\mathbf{n}(t)$	noise vector
$\mathbf{s}(t)$	sources vector
$\mathbf{w}_{CAP}$	weighting vector of Capon's beamformer
$\mathbf{w}_{CF}$	weighting vector of the conventional beamformer
$\mathbf{x}(t)$	snapshot vector
BBM	bootstrap based method
BJD	Born-Jordan distribution
CRLB	Cramer-Rao lower bound
CWD	Choi-Williams distribution
DF	direction finding
DML	deterministic maximum likelihood
DOA	direction of arrival
ESPRIT	estimation of signal parameters using rotational invariance techniques
FM	frequency modulated
IF	instantaneous frequency
JBD	joint block-diagonalisation
LFM signal	linear modulated signal
LS-ESPRIT	least-square ESPRIT
ML	maximum likelihood
MUSIC	multiple signal classification
MVDR	minimum variance distortionless response
Min-Norm	minimum norm
NSF	noise subspace fitting
PBM	projection based method
PWVD	pseudo Wigner-Ville distribution
RID	reduced interference distribution
RMSE	root mean-squared error
ROC	receiver operating characteristic
SML	stochastic maximum likelihood

SSF	signal subspace fitting
STFD	spatial time-frequency distribution
SVD	singular value decomposition
TF	time frequency
TFA	time-frequency averaging
TFD	time-frequency distribution
TFSAP	time frequency signal analysis and processing
TLS-ESPRIT	total least-square ESPRIT
ULA	uniform linear array
VCBM	vector clustering based method
WSF	weighted subspace fitting
WVD	Wigner-Ville distribution

List of Figures

General introduction

The estimation of the angle of arrival of a plane wave (or multiple plane waves) is commonly referred to as the direction finding (DF) or direction of arrival (DOA) estimation and it is one of the central problems in modern signal processing. It has found application in many fields such as radar, mobile communications, sonar, seismic systems, electronic surveillance, medical diagnosis and treatment, and radio astronomy.

Most of the conventional DOAs estimation methods such as beamforming, subspace based, subspace fitting and maximum likelihood methods are based on the assumption that the impinging signals are stationary. When the signals are nonstationary, these methods can still be used but their performances decrease.

One of the solutions to improve the performance in such scenario is to use the time-frequency analysis tools. The quadratique time-frequency distributions were first introduced by A. Belouchrani and M. Amin to the field of array signal processing leading to the definition of Spatial Time-Frequency Distributions (STFDs) [10]. The STFDs have been widely used for the separation of nonstationary sources [6, 7, 8, 10, 15, 29] and the estimation of DOAs of nonstationary sources [9, 14, 18, 19, 31, 32].

The STFD techniques are most appropriate to handle sources of nonstationary waveforms that are localised in the time-frequency domain. By spreading the noise power while localising the sources in time-frequency domain, the DOAs estimation performance and the robustness against noise are improved.

The application of the quadratic time-frequency distributions in the problem of DOAs estimation is the main subject of this report. We focus our attention on the selection of the most appropriate STFDs and auto- and cross-terms detection and integration methods.

In the first chapter the conventional DOAs estimation methods, which are based on the second-order statistics and assume the stationarity of the signals, are introduced and compared in nonstationary scenario.

The second chapter introduces the concept of time-frequency distributions. Their virtues are explored using some illustrative examples.

We deal with the time-frequency DOAs estimation methods in chapter three where the algorithms involved are given.

To validate the effectiveness of the time-frequency methods and compare their performance with the conventional ones, simulation results for nonstationary signals are presented in chapter four.

In chapter five, we present the Graphical User Interface *CTF-DOAs Tool* which is the implementation of all the conventional and time-frequency algorithms used in this report. The user can use them in

convenient way by changing the type and the parameters of the impinging signals, the configuration of the array as well as the parameters of the selected algorithm to perform the DOAs estimation and visualise the results. For the implementation of TFD, use used the TFD package developed by François Auger and others under the auspices of CNRS [3].

Table of Contents

Chapter 1

Directions of arrival estimation

1.1 Introduction

In this chapter, we present the conventional DOAs estimation methods, which are based on the second-order statistics, along with the concepts of nonstationarity and Cramer-Rao bounds. Some of these methods are also compared in nonstationary scenario.

1.2 Nonstationarity

1.2.1 Nonstationary signals

A deterministic signal is said to be *stationary* if it can be written as a discrete sum of sinusoids:

$$x(t) = \sum_{k \in \mathbf{N}} A_k \cos[2\pi w_k t + \phi_k] \quad \texttt{for a real signal} \tag{1.1}$$

$$x(t) = \sum_{k \in \mathbf{N}} A_k \exp[j(2\pi w_k t + \phi_k)] \quad \texttt{for a complex signal} \tag{1.2}$$

i.e. as a sum of elements which have constant instantaneous amplitude and instantaneous frequency.

In the random case, a signal $x(t)$ is said to be *wide-sense stationary* (or stationary up to the second order) if its expectation $E\{x(t)\}$ is independent of time and its autocorrelation function defined as

$$\mathcal{R}(t,\tau) = E\{x(t+\frac{\tau}{2})x^*(t-\frac{\tau}{2})\} \tag{1.3}$$

depends only on the lag, τ which is the difference in time between $t_1 = t + \tau/2$ and $t_2 = t - \tau/2$.

So a signal is said to be nonstationary if one of these fundamental assumptions is no longer valid. Nonstationary signals can be found in many areas including radar, sonar, astrophysics, seismology, vibration analysis, communications, speech, and biological signal processing.

1.2.2 Analytic signals and Hilbert transform

We recall some useful definitions related to the analytic signals and the Hilbert transform.

Definition 1.2.1 (Analytic signal[12]). A signal $z(t)$ is said to be analytic *iff*:

$$Z(f) = 0 \texttt{ for f < 0} \tag{1.4}$$

where $Z(f)$ is the Fourier transform $(\mathcal{FT})$ of $z(t)$

In other words, an analytic signal contains no negative frequencies; it may have a spectral component at zero frequency (DC).

Theorem 1.2.1 (Analytic signal[12]). *The signal*

$$z(t) = s(t) + jy(t) \tag{1.5}$$

where $s(t)$ *and* $y(t)$ *are real, is analytic with a real DC component,* iff*:*

$$Y(f) = (-jsgnf)S(f) \tag{1.6}$$

where $S(f)$ *and* $Y(f)$ *are the* $\mathcal{FT}'s$ *of* $s(t)$ *and* $y(t)$*, respectively, and where*

$$sgn\xi \triangleq \begin{cases} -1 & if \quad \xi < 0 \\ 0 & if \quad \xi = 0 \\ +1 & if \quad \xi > 0 \end{cases} \tag{1.7}$$

If the $\mathcal{FT}$ of $s(t)$ and $y(t)$ are related according to Eq. 1.6, $y(t)$ is the *Hilbert transform* of $s(t)$.

$$y(t) = \mathcal{H}[s(t)] \tag{1.8}$$

Where $\mathcal{H}[.]$ denotes the Hilbert transform of the signal, such that

$$\mathcal{H}[s(t)] = s(t) \star \frac{1}{\pi t}$$

$$\mathcal{H}[s(t)] = \frac{1}{\pi} p.v.\{\int_{-\infty}^{\infty} \frac{s(\tau)}{t-\tau} d\tau\}$$

where $p.v.\{.\}$ is the Cauchy principle value of the improper integral given in this case by

$$\lim_{\delta \to 0}[\int_{-\infty}^{t-\delta} \frac{s(\tau)}{t-\tau} d\tau + \int_{t+\delta}^{\infty} \frac{s(\tau)}{t-\tau} d\tau] \tag{1.9}$$

For a given real signal $s(t)$, we can construct the complex signal

$$z(t) = s(t) + j\mathcal{H}[s(t)] \tag{1.10}$$

This $z(t)$ is analytic and is called the analytic signal "corresponding to" or "associated with" the real signal $s(t)$.

1.2.3 FM signals

Many nonstationary signals encountered in radar, sonar, telecommunications, seismology, or biomedical engineering can be expressed in the general form of a complex analytic signal

$$z(t) = a_0 \exp\{j\varphi(t)\} \tag{1.11}$$

where a_0 and $\varphi(t)$, $t \in [T_1, T_2], T_1, T_2 < \infty$, are the amplitude and the phase of the signal, respectively. If certain regularity conditions are fulfilled [20], the phase $\varphi(t)$ of the signal $z(t)$ can be modeled using some distinct basis sequences, which leads to

$$z(t) = a_0 \exp\{j \sum_{q=0}^{Q} b_q \psi_{t,q}\} \tag{1.12}$$

Where $b_q, q = 0, ..., Q$, are unknown real valued parameters, and $\psi_{t,q}$ is an arbitrary set of basis sequences. The signal modeled by Eq. 1.12 is referred to as a frequency modulated (FM) signal.

In the special case where $\psi_{t,q} = t^q$, $z(t)$ is called polynomial phase signal. Some interesting polynomial phase signals include linear FM (chirp) signals obtained for $Q = 2$ and quadratic FM signals obtained for $Q = 3$.

Chirp signals are encountered in many area of engineering including sonar, radar, oceanography, and ultrasound imaging. For instance, they have been widely used in sonar applications for range and Doppler estimation, as well as in radar systems for pulse compression. They were suggested for signaling in communication systems [28]. Chirp signals are also used in military communications applications where they are sent out as hostile signals to destroy other communications. The quadratic FM model can be applied to radar [25] and some biological signals [2], [24]. Polynomial phase signals of order higher than three is usually used as an approximation of FM signals with arbitrary nonlinearity, provided the phase in continuous in a given interval.

In this work we use mainly the chirp and quadratic FM signals for the purpose of modeling nonstationary signals.

1.3 Data model and assumptions

We assume that the L narrowband signals, whose directions of arrival need to be estimated, have the same central frequency f_c and are received as plane waves by a Uniform Linear Array (ULA) whose M $(M > L)$ elements are separated by a distance equal to half a wavelength $(d = \lambda/2)$. The propagation medium is linear which implies the validity of the superposition principle.

An element of the array receives a real-valued bandpass signal with central frequency f_c

$$z(t) = \Re(s(t)e^{j2\pi f_c}) = s_p(t)cos(2\pi f_c t) - s_q(t)sin(2\pi f_c t) \tag{1.13}$$

the baseband signal(the complex envelope of $z(t)$) is

$$s(t) = s_p(t) + js_q(t) \tag{1.14}$$

$s(t)$ is recovered from $z(t)$ by demodulation: multiplying the received signal with $cos(2\pi f_c t)$ and $sin(2\pi f_c t)$ followed by low-pass filtering.

We now show the effect of small delays of $z(t)$ on the baseband signal $s(t)$

$$z_\tau(t) = z(t-\tau) = \Re(s(t-\tau)e^{-j2\pi f_c \tau}e^{j2\pi f_c}) \tag{1.15}$$

Then the complex envelope of the delayed signal is

$$s_\tau(t) = s(t-\tau)e^{-j2\pi f_c \tau} \tag{1.16}$$

Let W be the bandwidth of $s(t)$. If $e^{j2\pi f\tau} \approx 1$ for all frequencies $\mid f \mid \leq \frac{W}{2}$ (narrowband signal), then

$$s(t-\tau) = \int_{-W/2}^{W/2} S(f)e^{j2\pi f(t-\tau)}df \approx \int_{-W/2}^{W/2} S(f)e^{j2\pi ft}df = s(t) \tag{1.17}$$

Thus, for $W\tau \ll 1$

$$s_\tau(t) = s(t)e^{-j2\pi f_c \tau} \tag{1.18}$$

Let $a(\theta)$ be the directional response of a single antenna element (antenna gain pattern). For omnidirectional antenna: $a(\theta) = a(constant)$. We call $s(t)$ the baseband signal at the first antenna: $x_1(t) = a(\theta)s(t)$.

The signal received by the next element experiences an additional delay $\tau = \frac{d}{c}sin(\theta)$ (see Fig. 1.1), where c is the propagation speed of the wave (light velocity).

If τ is small compared to the inverse bandwidth of $s(t)$ then

$$x_2(t) = s_\tau(t) = s(t)e^{-j2\pi f_c \tau} = s(t)e^{-j2\pi f_c \frac{d}{c} sin(\theta)} \tag{1.19}$$

If the delays experienced by all the elements are small comparable to the inverse bandwidth

$$(M-1)\frac{d}{\lambda}sin(\theta) \ll \frac{f_c}{W}$$

the received signal by the k^{th} element can be written as

$$x_k(t) = s_{(k-1)\tau}(t) = s(t)e^{-j2\pi f_c (k-1)\tau} = s(t)e^{-j2\pi f_c (k-1)\frac{d}{c}}$$

The received signals $x_1(t), x_2(t), \cdots, x_M(t)$ collected into a vector $\mathbf{x}(t)$ are then given by

$$\mathbf{x}(t) = \begin{bmatrix} x_1(t) \\ x_2(t) \\ \vdots \\ x_M(t) \end{bmatrix} = \begin{bmatrix} 1 \\ e^{-j\phi} \\ \vdots \\ e^{-j(M-1)\phi} \end{bmatrix} a(\theta)s(t) = \mathbf{a}(\theta)s(t) \tag{1.20}$$

where $\phi = 2\pi\frac{d}{\lambda}sin(\theta)$ is the electrical angle, $\mathbf{a}(\theta)$ is the steering vector, and $\mathbf{x}(t)$ is called snapshot. For more than one source, the model takes the following form

$$\mathbf{x}(t) = \mathbf{a}(\theta_1)s_1(t) + \mathbf{a}(\theta_2)s_2(t) + \cdots + \mathbf{a}(\theta_L)s_L(t) \tag{1.21}$$

$$= [\mathbf{a}(\theta_1)\mathbf{a}(\theta_2)\cdots\mathbf{a}(\theta_L)] \begin{bmatrix} s_1(t) \\ s_2(t) \\ \vdots \\ s_L(t) \end{bmatrix} = \mathbf{A}(\theta)\mathbf{s}(t) \tag{1.22}$$

Where

$$\mathbf{A}(\theta) = [\mathbf{a}(\theta_1)\mathbf{a}(\theta_2)\cdots\mathbf{a}(\theta_L)]$$

$$\theta = [\theta_1\theta_2\cdots\theta_L]$$

$$\mathbf{s}(t) = [s_1(t)s_2(t)\cdots s_L(t)]^T$$

In the presence of additive noise $\mathbf{n}(t)$ we get the model commonly used in array processing

$$\mathbf{x}(t) = \mathbf{A}(\theta)\mathbf{s}(t) + \mathbf{n}(t) \tag{1.23}$$

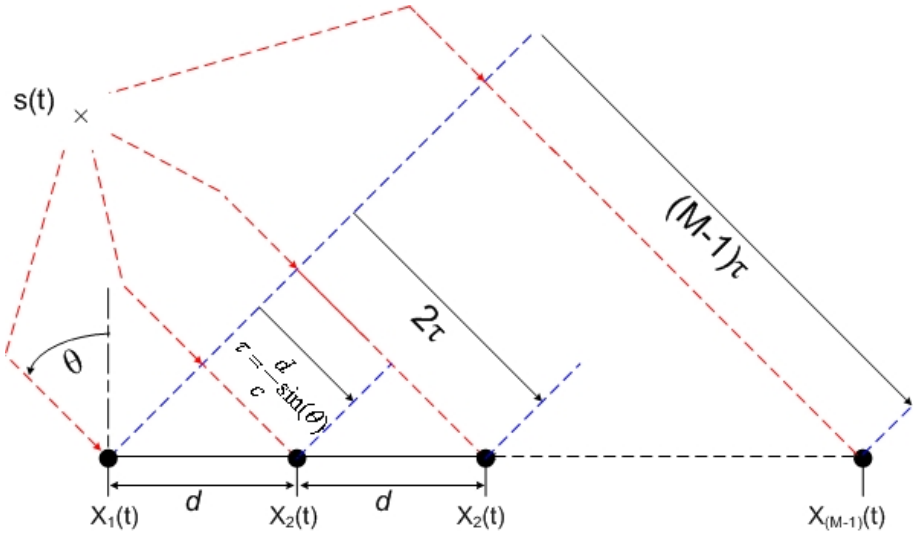

Figure 1.1: Baseband model for DOAs estimation

we assume that the noise is temporally and spatially white zero-mean process, i.e.

$$E\{\mathbf{n}(t)\mathbf{n}^H(s)\} = \sigma_n^2 \mathbf{I}_M \delta_{t,s}$$

1.3.1 Cramer-Rao lower bounds

The Cramer-Rao Lower Bound (CRLB) is a lower bound on the variance of any unbiased estimator for a given data model.

Two different types of data model are currently used in the applications concerned with estimating the DOAs of narrowband signals using sensor arrays:

1. Deterministic (Conditional) model which assumes the source signals to be deterministic and unknown.
2. Stochastic (Unconditional) model which assumes the source signals to be random.

These two models lead to different Cramer-Rao Bounds (CRB) on DOAs estimation accuracy ($CRLB_D$ and $CRLB_S$).

The following formula for $CRLB_D(\theta)$, has been derived in [27] (see also appendix A)

$$CRLB_D(\theta) = \frac{\sigma^2}{2N}\{\Re[\mathcal{D} \odot \hat{\mathbf{R}}_{\mathbf{ss}}^T]\}^{-1} \tag{1.24}$$

where

$$\mathcal{D} = \mathbf{D}^H[\mathbf{I} - \mathbf{A}(\mathbf{A}^H\mathbf{A})^{-1}\mathbf{A}^H]\mathbf{D} \tag{1.25}$$

$$\mathbf{D} = [\mathbf{d}_1, \mathbf{d}_2, ..., \mathbf{d}_n] \tag{1.26}$$

$$\mathbf{d}_i = d\mathbf{a}(\theta)/d\theta|_\theta = \theta_i \tag{1.27}$$

and

$$\hat{\mathbf{R}}_{\mathbf{ss}} = \frac{1}{N}\sum_{t=1}^{N}\mathbf{s}(t)\mathbf{s}(t)^H$$

The asymptotic (for $N \gg 0$) stochastic Cramer-Rao Lower Bound is given in [27] as:

$$CRLB_S(\theta) = \frac{\sigma^2}{2N}\{\Re[\mathcal{D}\odot(\mathbf{R}_{\mathbf{ss}}\mathbf{A}^H\mathbf{R}_{\mathbf{xx}}^{-1}\mathbf{A}\mathbf{R}_{\mathbf{ss}}]\}^{-1} \tag{1.28}$$

1.4 Directions of arrival estimation methods

All the methods described in this chapter are based on the second-order statistics, and assume the stationarity of the source signals. The narrowband snapshots model in the time domain is considered.

1.4.1 Beamforming techniques

The first attempt to localise signal sources using antenna array was through beamforming techniques [21]. The idea is to steer the array in one direction at the time and to measure the output power. The steering locations which result in maximum power yield the DOAs estimates. The array response is steered by forming a linear combination of the sensor outputs.

$$\mathbf{y}(t) = \sum_{m=0}^{M} w_m^* x_m(t) = \mathbf{w}^H\mathbf{x}(t) \tag{1.29}$$

Given samples $\mathbf{y}(1), \mathbf{y}(2), ..., \mathbf{y}(N)$, the output power is measured by

$$P(\mathbf{w}) = \frac{1}{N}\sum_{t=1}^{N} \mid \mathbf{y}(t) \mid^2 = \frac{1}{N}\sum_{t=1}^{N}\mathbf{w}^H\mathbf{x}(t)\mathbf{x}(t)^H\mathbf{w} = \mathbf{w}^H\hat{\mathbf{R}}_{\mathbf{xx}}\mathbf{w} \tag{1.30}$$

Where

$$\hat{\mathbf{R}}_{\mathbf{xx}} = \frac{1}{N}\sum_{t=1}^{N}\mathbf{x}(t)\mathbf{x}(t)^H \tag{1.31}$$

is an estimate of the spatial covariance matrix $E\{\mathbf{x}(t)\mathbf{x}^H(t)\}$.

Different beamformers corresponding to different choices of the weighting vector $\mathbf{w}$ exist in the literature.

1.4.1.1 Conventional beamformer

For an array of arbitrary geometry, the conventional (or Bartlett) beamformer maximises the power of the beamforming output for a given input signal. Suppose we wish to maximise the output power from a certain direction θ. Given a signal emanating from direction θ, a measurement of the array output corrupted by additive noise is written as

$$\mathbf{x}(t) = \mathbf{a}(\theta)s(t) + \mathbf{n}(t). \tag{1.32}$$

The problem of maximising the output power is then formulated as,

$$\max_{\mathbf{w}} E\{\mathbf{w}^H\mathbf{x}(t)\mathbf{x}(t)^H\mathbf{w}\} = \max_{\mathbf{w}} \mathbf{w}^H E\{\mathbf{x}(t)\mathbf{x}(t)^H\}\mathbf{w} \tag{1.33}$$

$$= \max_{\mathbf{w}} E\{\mid s(t) \mid^2 \mid \mathbf{w}^H\mathbf{a}(\theta) \mid^2 + \sigma_n^2 \mid \mathbf{w} \mid^2\} \tag{1.34}$$

where the assumption of spatially white noise is used. To obtain a non-trivial solution, the norm of $\mathbf{w}$ is constrained to $\mid \mathbf{w} \mid^2 = 1$ when carrying out the above maximisation. The resulting solution is then

$$\mathbf{w}_{CF} = \frac{\mathbf{a}(\theta)}{\sqrt{\mathbf{a}^H(\theta)\mathbf{a}(\theta)}} \tag{1.35}$$

The above weight can be interpreted as spatial filter which has been matched to the impinging signal. The array weighting equalizes the delays and attenuation experienced by the signal on various sensors to maximally combine their respective contributions. Inserting the weighting vector (Eq. 1.35) into Eq. 1.30, the classical spatial spectrum is obtained

$$P_{CF}(\theta) = \frac{\mathbf{a}^H(\theta)\hat{\mathbf{R}}_{\mathbf{xx}}\mathbf{a}(\theta)}{\mathbf{a}^H(\theta)\mathbf{a}(\theta)} \tag{1.36}$$

This spatial spectrum has a resolution threshold. Waves arriving with electrical angle separation less than the beamwidth $(2\pi/M)$ can not be resolved with this method regardless of N and SNR. For example, using a ten-element ULA with an element separation of $d = \lambda/2$ results in a resolution threshold of $\Delta = 12^o$ (an illustrative example is given in Fig. 1.2 where the DOAs of two sources are separated by 10^o)

1.4.1.2 Capon's beamformer

The Capon's beamformer attempts to alleviate the limitations of the conventional beamformer, such as its resolving power. This beamformer minimises the power contributed by noise and any signals coming from other directions than θ, while maintaining a fixed gain in the direction θ. This type of beamformer is sometimes also referred to as Minimum Variance Distortionless Response (MVDR) filter. The optimisation problem was posed as

$$\min_{\mathbf{w}} P(\mathbf{w}) \tag{1.37}$$

$$\text{subject to } \mathbf{w}^H\mathbf{a}(\theta) = 1$$

where $P(\mathbf{w})$ is as defined in Eq. 1.30. The Capon weighting vector is

$$\mathbf{w}_{CAP} = \frac{\hat{\mathbf{R}}_{\mathbf{xx}}^{-1}\mathbf{a}(\theta)}{\mathbf{a}^H(\theta)\hat{\mathbf{R}}_{\mathbf{xx}}^{-1}\mathbf{a}(\theta)} \tag{1.38}$$

Inserting the above weight into Eq. 1.30 leads to the following spatial spectrum

$$P_{CAP}(\theta) = \frac{1}{\mathbf{a}^H(\theta)\hat{\mathbf{R}}_{\mathbf{xx}}^{-1}\mathbf{a}(\theta)} \tag{1.39}$$

Although more complex than the conventional beamformer, Capon's method offers significantly reduced resolution threshold than the conventional beamformer (see Fig. 1.2).

Although neither the Bartlett's beamformer nor Capon's beamformer are efficient parameter estimators, they can play a useful role as a preliminary processor to indicate the number of plane waves impinging on the array, their approximate location, and their approximate signal power.

Many other beamforming methods have been presented in the literature but their resolution threshold still quite high and that was one of the motivations for the interest in the subspace methods that are described next.

1.4.2 Subspace based methods

The subspace methods [21] (also called eigenstructure methods) exploit the eigendecomposition of the array covariance matrix $\mathbf{R}_{\mathbf{xx}}$ given by

$$\mathbf{R}_{\mathbf{xx}} = E\{\mathbf{x}(t)\mathbf{x}^H(t)\} = \mathbf{A}(\theta)\mathbf{R}_{\mathbf{ss}}\mathbf{A}^H(\theta) + \mathbf{R}_{\mathbf{nn}} \tag{1.40}$$

Where $\mathbf{R}_{\mathbf{ss}} = E\{\mathbf{s}(t)\mathbf{s}^H(t)\}$ is the $L \times L$ source covariance matrix and $\mathbf{R}_{\mathbf{nn}} = E\{\mathbf{n}(t)\mathbf{n}^H(t)\}$ is the $M \times M$ noise covariance matrix. When the noise is temporally and spatially white zero-mean process, $\mathbf{R}_{\mathbf{nn}} = \sigma_n^2\mathbf{I}_M$. If the noise is colored and its covariance matrix is known or can be estimated the measurement can be whitened by multiplying the measurement from the left by the matrix $\Lambda^{-1/2}\mathbf{E}_{\mathbf{n}}^H$ obtained by the orthogonal eigendecomposition $\mathbf{R}_{\mathbf{nn}} = \mathbf{E}_n\Lambda\mathbf{E}_n^H$. In practice, $\mathbf{R}_{\mathbf{xx}}$ is unknown and an estimate $\hat{\mathbf{R}}_{\mathbf{xx}}$ is used instead. The array spatial covariance matrix can be estimated by Eq. 1.31.

To see the implications of the eigendecomposition of $\hat{\mathbf{R}}_{\mathbf{xx}}$, we first state the properties of $\mathbf{R}_{\mathbf{xx}}$.

1. If the sources are uncorrelated or partially correlated, $rank(\mathbf{R}_{\mathbf{ss}}) = L$. If there are coherent sources, $rank(\mathbf{R}_{\mathbf{ss}}) < L$.

2. If the column of $\mathbf{A}$ are independent, which is generally true when the DOAs are different, then $\mathbf{A}$ is of full-rank L.

3. Properties 1 and 2 imply $rank(\mathbf{A}\mathbf{R}_{\mathbf{ss}}\mathbf{A}^H) = L$; therefore $\mathbf{A}\mathbf{R}_{\mathbf{ss}}\mathbf{A}^H$ must have L nonzero eigenvalues and $(M - L)$ zero eigenvalues. Let the eigendecomposition of $\mathbf{A}\mathbf{R}_{\mathbf{ss}}\mathbf{A}^H$ be $\mathbf{A}\mathbf{R}_{\mathbf{ss}}\mathbf{A}^H = \sum_{i=1}^{M} \alpha_i \mathbf{e}_i \mathbf{e}_i^H$; then $\alpha_1 \geq \alpha_2 \geq ... \geq \alpha_L \geq \alpha_{L+1} = ... = \alpha_M = 0$ are the rank-ordered eigenvalues, and $\{\mathbf{e}_i\}_{i=1}^{M}$ are the corresponding eigenvectors.

4. Since $\mathbf{R}_{\mathbf{nn}} = \sigma_n^2 \mathbf{I}_M$, the eigenvectors of $\mathbf{R}_{\mathbf{xx}}$ are the same as those of $\mathbf{A}\mathbf{R}_{\mathbf{ss}}\mathbf{A}^H$, and its eigenvalues are $\lambda_i = \alpha_i + \sigma_n^2$ for $1 \leq i \leq L$ and $\lambda_i = \sigma_n^2$ for $L+1 \leq i \leq M$. The eigenvectors can be partitioned into two sets: $\mathbf{E}_s \triangleq [\mathbf{e}_1, \mathbf{e}_2, ..., \mathbf{e}_L]$ forms the *signal subspace*, whereas $\mathbf{E}_n \triangleq [\mathbf{e}_{L+1}, \mathbf{e}_{L+2}, ..., \mathbf{e}_M]$ forms the *noise subspace*. These subspaces are orthogonal. The signal eigenvalues matrix is $\Lambda_s = diag\{\lambda_1, \lambda_2, ..., \lambda_L\}$, and the noise eigenvalues matrix is $\Lambda_n = diag\{\lambda_{L+1}, \lambda_{L+2}, ..., \lambda_M\}$. Hence, we can write

$$\mathbf{R}_{\mathbf{xx}} = \mathbf{E}\Lambda\mathbf{E}^H = \mathbf{E}_s\Lambda_s\mathbf{E}_s^H + \mathbf{E}_n\Lambda_n\mathbf{E}_n^H = \mathbf{E}_s\Lambda_s\mathbf{E}_s^H + \sigma_n^2\mathbf{E}_n\mathbf{E}_n^H \tag{1.41}$$

   Where $\mathbf{E} \triangleq [\mathbf{e}_1, \mathbf{e}_2, ..., \mathbf{e}_M]$ and $\Lambda = diag\{\lambda_1, \lambda_2, ..., \lambda_M\}$.

5. The eigenvectors corresponding to zero eigenvalues satisfy $\mathbf{A}\mathbf{R}_{\mathbf{ss}}\mathbf{A}^H\mathbf{e}_i = 0$ for $L + 1 \leq i \leq M$; hence, $\mathbf{A}^H\mathbf{e}_i = 0$ for $L + 1 \leq i \leq M$ because $\mathbf{A}$ and $\mathbf{R}_{\mathbf{ss}}$ are full rank.

The last property means that the steering vectors are orthogonal to the noise subspace eigenvectors. It further implies, because of the orthogonality of the signal and noise subspace, that the signal eigenvectors and the steering vectors span the same subspace.

The signal and noise subspaces can also be obtained by performing a Singular Value Decomposition (SVD) directly on the received data matrix without having to calculate the array covariance matrix.

$$\mathbf{X} = \begin{pmatrix} x_1(1) & x_1(2) & \cdots & x_1(N) \\ x_2(1) & x_2(2) & \cdots & x_2(N) \\ \vdots & \vdots & \ddots & \vdots \\ x_M(1) & x_M(2) & \cdots & x_M(N) \end{pmatrix} = \hat{\mathbf{E}}\Sigma_1\mathbf{V}_1^H \tag{1.42}$$

Because $\hat{\mathbf{R}}_{\mathbf{xx}} = \mathbf{X}\mathbf{X}^H = \hat{\mathbf{E}}\Sigma_1\mathbf{V}_1^H\mathbf{V}_1\Sigma_1\hat{\mathbf{E}}^H = \hat{\mathbf{E}}\Sigma_1^2\hat{\mathbf{E}} = \hat{\mathbf{E}}\Lambda\hat{\mathbf{E}}^H$.

It is stated that the properties of DOA estimates do not depend on which method used; However, SVD must then deal with a data matrix that increases in size as the new snapshots are received. Thus we will estimate the signal and the noise subspaces by performing an eigendecomposition on the estimated covariance matrix $\hat{\mathbf{R}}_{\mathbf{xx}}$.

The eigendecomposition of $\hat{\mathbf{R}}_{\mathbf{xx}}$, and eigenvector partition into signal and noise subspaces, lead to a number of subspace based direction finding methods. Some of these methods are described next. The use of subspace based methods results in better resolution performance than conventional methods.

1.4.2.1 MUSIC algorithm

The **MU**ltiple **SI**gnal **C**lassification method is relatively simple but efficient subspace based DOA estimation method [26]. This method assume that the response of the array to a single source, *the array manifold* $\mathbf{a}(\theta)$, is either known analytically as a function of θ, or is obtained through the calibration of the array.

Since the eigenvectors in $\mathbf{E}_n$ are orthogonal to $\mathbf{A}(\theta)$, we have for $\theta \in \{\theta_1, \theta_2, ..., \theta_L\}$

$$\mathbf{E}_n^H \mathbf{a}(\theta) = 0 \tag{1.43}$$

There are two versions of the MUSIC algorithm, namely spectral MUSIC and root-MUSIC. The first one is applicable to arbitrary array geometry whereas the second one is applicable to ULA.

1. Spectral MUSIC

Once the noise subspace has been estimated, a search for the L directions of arrival is made by looking for steering vectors that are as orthogonal to the noise subspace as possible. This is normally accomplished by searching for peaks in the MUSIC spectrum given by

$$\mathbf{P}_{MU}(\theta) = \frac{1}{\mathbf{a}^H(\theta)\mathbf{E}_n\mathbf{E}_n^H\mathbf{a}(\theta)} = \frac{1}{\|\mathbf{E}_n^H\mathbf{a}(\theta)\|^2} \tag{1.44}$$

It should be noted that instead of using the noise subspace and searching for directions with steering vectors orthogonal to this subspace, one could also use the signal subspace and search for directions with steering vectors contained in this subspace. This amounts to searching for peaks in

$$\mathbf{P}_{MU}(\theta) = \|\mathbf{E}_s^H\mathbf{a}(\theta)\|^2 \tag{1.45}$$

The MUSIC algorithm has better performance than the beamforming algorithms. The performance of the MUSIC, Capon and Bartlett estimators is illustrated in Fig. 1.2 where a ten-element array receives two chirp signals from the directions $(\theta_1, \theta_2) = (-5^o, 5^o)$, $SNR = 0dB$ and $N = 100$ snapshots.

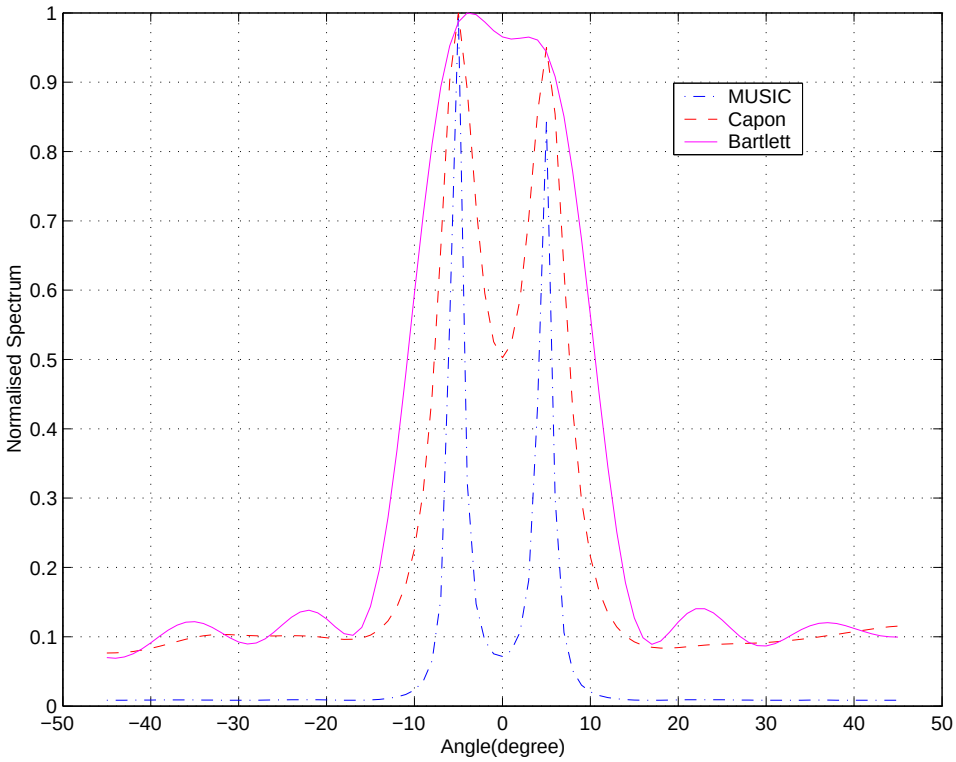

Figure 1.2: MUSIC, Capon and Bartlett algorithms: normalised spectrum versus DOA

2. Root-MUSIC

For a uniformly spaced linear array, the MUSIC spectrum can be expressed such that the search for DOA can be made by finding the root of a polynomial.

Let us define the polynomials

$$Q_i(z) = \mathbf{u}_i^H \mathbf{p}(z), i = L+1, L+2, ..., M. \tag{1.46}$$

where $\mathbf{u}_i$ is the i^{th} eigenvector of $\mathbf{R_{xx}}$ and

$$\mathbf{p}(z) = [1, z, z^2, ..., z^{M-1}]^T \tag{1.47}$$

From the problem formulation, one can makes the basic observation that $Q_i(z)$ has L of its zeros at $e^{-j\phi_k}$, $k = 1, 2, ..., L$ provided that $\mathbf{R_{ss}}$ is full rank.

For the exploitation of the information from all the noise eigenvectors simultaneously, we want to find the zeros of the MUSIC-like function

$$\|\hat{\mathbf{E}}_n^H \mathbf{p}(z)\|^2 = \mathbf{p}^H(z) \hat{\mathbf{E}}_n \hat{\mathbf{E}}_n^H \mathbf{p}(z) \tag{1.48}$$

However, the latter is not a polynomial in z (power of z^* are now present), which complicates the search for zeros. Since the values of z on the unit circle are of interest, we can use $\mathbf{p}^T(z^{-1})$ instead of $\mathbf{p}^H(z)$. After replacing $\mathbf{p}^H(z)$ by $\mathbf{p}^T(z^{-1})$ and multiplying Eq. 1.48 by z^{M-1} we obtain the root-MUSIC polynomial

$$Q_{MU}(z) = z^{M-1}\mathbf{p}^T(z^{-1})\hat{\mathbf{E}}_n\hat{\mathbf{E}}_n^H\mathbf{p}(z) \tag{1.49}$$

$Q_{MU}(z)$ is a polynomial of degree $2(M-1)$ with $2(M-1)$. However, we can show that not all zeros are independent. If z_k is zero of $Q_{MU}(z)$, $1/z_k^*$ is also a zero of $Q_{MU}(z)$. The zeros of $Q_{MU}(z)$ therefore come in pairs.

since z_k and $1/z_k^*$ have the same phase and reciprocal magnitude, one zero is within the unit circle and the other is outside. From the definition of z, only the phase carries the desired information, i.e., both z_k and $1/z_k^*$ carry the same desired information.

The steps of root-MUSIC are:

1. Estimate the correlation matrix using Eq. 1.31. Find its eigendecomposition $\hat{\mathbf{R}}_{\mathbf{xx}} = \hat{\mathbf{E}}\Lambda\hat{\mathbf{E}}^H$
2. Partition $\hat{\mathbf{E}}$ to obtain $\hat{\mathbf{E}}_n$.
3. Form the polynomial $Q_{MU}(z)$ using the Eq. 1.49.
4. Find the roots of the polynomial $Q_{MU}(z)$ in terms of $(M-1)$ pairs.
5. Of the $(M-1)$ roots within the unit circle, choose the L closest to the unit circle $(z_k, k = 1, 2, ..., L)$.
6. Obtain the directions of arrival using

$$\theta_k = -\arcsin\{\frac{\angle z_k}{2\pi\frac{d}{\lambda}}\} \tag{1.50}$$

As root-MUSIC only worries about the phase of the roots, errors in the magnitude do not affect the estimated DOAs. In some cases, especially in low SNR situations, root-MUSIC may provide better performance than spectral MUSIC.

1.4.2.2 Min-Norm algorithm

The Min-Norm algorithm also uses the orthogonality between the steering vector and the noise subspace [22]. But instead of doing this directly, Min-Norm first identifies a single vector in the noise subspace (the prediction vector $\mathbf{b}$ with minimum norm and unit first element). If the noise subspace is partitioned as

$$\mathbf{E}_n = \begin{pmatrix} \mathbf{c}^H \\ --- \\ \mathbf{E}_n^{'} \end{pmatrix} \tag{1.51}$$

were $\mathbf{c}^H$ is the first row and $\mathbf{E}_n^{'}$ the rest rows of $\mathbf{E}_n$, then the prediction vector can be expressed as

$$\mathbf{b} = \mathbf{E}_n \frac{\mathbf{c}}{\|\mathbf{c}\|^2} \triangleq \mathbf{E}_n \overline{\mathbf{c}} \tag{1.52}$$

1. Spectral Min-Norm

To find the directions of arrival, we need to search for the L largest peaks over θ of the following spatial spectrum

$$\mathbf{P}_{MN}(\theta) = \frac{1}{|\mathbf{a}^H(\theta)\hat{\mathbf{b}}|^2} \tag{1.53}$$

Using Eq. 1.52, this spectrum can be alternatively expressed

$$\mathbf{P}_{MN}(\theta) = \frac{1}{\mathbf{a}^H(\theta)\hat{\mathbf{E}}_n\hat{\hat{\mathbf{c}}}\hat{\hat{\mathbf{c}}}^H\hat{\mathbf{E}}_n^H\mathbf{a}(\theta)} \tag{1.54}$$

2. Root-Min-Norm

In the case of ULA, a polynomial Min-Norm algorithm can be defined. Orthogonality is obtained by setting the following polynomial equal to zero.

$$Q_{MN}(z) = \mathbf{p}^T(z^{-1})\mathbf{b} = \sum_{k=1}^{M} b_k z^{-k+1} \tag{1.55}$$

Where $\mathbf{p}(z)$ is defined in Eq. 1.47. Then the directions of arrival are found by rooting the above $M-1$ degree polynomial and picking the L closest roots to the unit circle and using Eq. 1.50.

1.4.2.3 ESPRIT algorithm

The ESPRIT (**E**stimation of **S**ignal **P**arameters using **R**otational **I**nvariance **T**echniques) algorithm uses the structure of the ULA steering vectors in a slightly different way [22]. The observation here is that $\mathbf{A}(\theta)$ has a so-called *shift structure*. We divide a ULA of M elements into two identical subarrays of $(M-m)$ elements shifted by a distance $m \times d$, as shown in Fig. 1.3 for $m = 1$.

Two sub-matrices $\mathbf{A}_1$ and $\mathbf{A}_2$ are formed by deleting the first m and the last m rows from $\mathbf{A}$ respectively,i.e.,

$$\mathbf{A} = \begin{bmatrix} \mathbf{A}_1 \\ \text{last } m \text{ rows} \end{bmatrix} = \begin{bmatrix} \text{first } m \text{ rows} \\ \mathbf{A}_2 \end{bmatrix} \tag{1.56}$$

Since for ULA, the steering matrix takes the special form (Vandermonde matrix)

$$\mathbf{A}(\theta) = \begin{pmatrix} 1 & 1 & \cdots & 1 \\ e^{-j\phi_1} & e^{-j\phi_2} & \cdots & e^{-j\phi_L} \\ \vdots & \vdots & & \vdots \\ e^{-j(M-1)\phi_1} & e^{-j(M-1)\phi_2} & \cdots & e^{-j(M-1)\phi_L} \end{pmatrix}, \phi_k = 2\pi\frac{d}{\lambda}\sin(\theta_k) \tag{1.57}$$

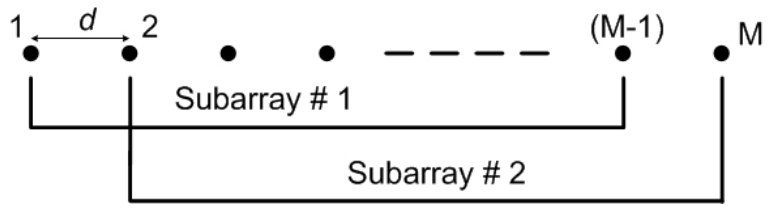

Figure 1.3: The array structure exploited by ESPRIT ($m = 1$)

the matrices $\mathbf{A}_1$ and $\mathbf{A}_2$ are related by the formula

$$\mathbf{A}_2 = \mathbf{A}_1\Phi \tag{1.58}$$

Where Φ is a diagonal matrix having the roots $e^{-jm\phi_k}, k = 1, 2, ..., L$, on the diagonal.

The DOAs estimation problem can be reduced to that of finding Φ. If $\mathbf{E}_{1s}$ and $\mathbf{E}_{2s}$ denote two $(M - m) \times L$ matrices with their columns denoting the L eigenvectors corresponding to the largest eigenvalues of the two subarray correlation matrices $\mathbf{R}_1$ and $\mathbf{R}_2$ respectively. As these two sets of eigenvectors span the same L-dimensional signal space, it follows that these two matrices $\mathbf{E}_{1s}$ and $\mathbf{E}_{2s}$ are related by unique non singular transformation matrix Ψ, that is,

$$\mathbf{E}_{1s}\Psi = \mathbf{E}_{2s} \tag{1.59}$$

Similarly, these two matrices are related to the steering vector matrices $\mathbf{A}_1$ and $\mathbf{A}_2$ by another unique non singular transformation matrix $\mathbf{T}$ as the same signal subspace is spanned by these steering vectors. Thus,

$$\mathbf{E}_{1s} = \mathbf{A}_1\mathbf{T} \tag{1.60}$$

$$\mathbf{E}_{2s} = \mathbf{A}_2\mathbf{T} \tag{1.61}$$

Using Eqs. 1.59, 1.60 and 1.61, and the fact that the matrix $\mathbf{A}_1$ is full rank.

$$\mathbf{T}\Psi\mathbf{T}^{-1} = \Phi \tag{1.62}$$

The matrices Ψ and Φ are related by similarity transformation, and hence have the same eigenvalues. The later is of course given by $e^{-jm\phi_k}, k = 1, 2, ..., L$, and are related to the DOAs by Eq. 1.50.

The ESPRIT algorithm can be now summarised :

1. Compute the two sub-array correlation matrices $\hat{\mathbf{R}}_1$ and $\hat{\mathbf{R}}_2$ and their eigendecompositions.
2. Form $\hat{\mathbf{E}}_{1s}$ and $\hat{\mathbf{E}}_{2s}$ corresponding the L principal eigenvectors of the matrices $\hat{\mathbf{R}}_1$ and $\hat{\mathbf{R}}_2$ respectively.

3. Solve Eq. (1.59) in either a Least-Square sense (LS-ESPRIT) or a Total-Least-Square sense (TLS-ESPRIT).

4. The DOA estimates are obtained by applying the following formula to the eigenvalues of $\hat{\Psi}$, $(\lambda_{\psi k}, k = 1, 2, ..., L)$.

$$\theta_k = -\arcsin\{\frac{\angle\lambda_{\psi k}}{2m\pi\frac{d}{\lambda}}\}, k = 1, 2, ..., L \tag{1.63}$$

We note that, for ULA, $\hat{\mathbf{E}}_{1s}$ and $\hat{\mathbf{E}}_{2s}$ can also be obtained without computing the two subarray correlation matrices $\hat{\mathbf{R}}_1$ and $\hat{\mathbf{R}}_2$ but by computing the array correlation matrix $\hat{\mathbf{R}}_{\mathbf{xx}}$ and its eigendecomposition. The matrix $\hat{\mathbf{E}}_s$ is partitioned conformably with $\mathbf{A}$ into $\hat{\mathbf{E}}_{1s}$ and $\hat{\mathbf{E}}_{2s}$, that is

$$\hat{\mathbf{E}}_s = \begin{bmatrix} \hat{\mathbf{E}}_{s1} \\ \text{last } m \text{ rows} \end{bmatrix} = \begin{bmatrix} \text{first } m \text{ rows} \\ \hat{\mathbf{E}}_{s2} \end{bmatrix} \tag{1.64}$$

1. LS-ESPRIT

The Least-Square solution to Eq. 1.59 is

$$\hat{\Psi} = \hat{\mathbf{E}}_{s1}^{\dagger}\hat{\mathbf{E}}_{s2} \tag{1.65}$$

where $\hat{\mathbf{E}}_{s1}^{\dagger} = (\hat{\mathbf{E}}_{s1}^H\hat{\mathbf{E}}_{s1})^{-1}\hat{\mathbf{E}}_{s1}^H$ is the pseudo-inverse of $\hat{\mathbf{E}}_{s1}$.

2. TLS-ESPRIT

The TLS version of ESPRIT is summarised below.

1. Form the matrices $\hat{\mathbf{E}}_{1s}$ and $\hat{\mathbf{E}}_{2s}$

2. Form a $2L \times 2L$ matrix

$$\mathbf{B} = \begin{bmatrix} \hat{\mathbf{E}}_{s1}^H \\ \hat{\mathbf{E}}_{s2}^H \end{bmatrix} \begin{bmatrix} \hat{\mathbf{E}}_{s1} & \hat{\mathbf{E}}_{s2} \end{bmatrix} \tag{1.66}$$

and perform its eigendecomposition

$$\mathbf{B} = \mathbf{V}\Lambda\mathbf{V}^H \tag{1.67}$$

where Λ is a diagonal matrix containing the eigenvalues of $\mathbf{B}$ on its diagonal, and the columns of $\mathbf{V}$ are the eigenvectors of $\mathbf{B}$.

3. Partition $\mathbf{V}$ into four matrices of dimension $L \times L$ as

$$\mathbf{V} = \begin{pmatrix} \mathbf{V}_{11} & \mathbf{V}_{12} \\ \mathbf{V}_{21} & \mathbf{V}_{22} \end{pmatrix} \tag{1.68}$$

4. Calculate the eigenvalues $\beta_k, k = 1, 2, ..., L$ of the matrix $-\mathbf{V}_{11}\mathbf{V}_{22}^{-1}$

5. Estimate the angles of arrival $\theta_k, k = 1, 2, ..., L$ using

$$\theta_k = -\arcsin(\frac{\angle\beta_k}{2m\pi\frac{d}{\lambda}}) \tag{1.69}$$

We note that the matrix $\mathbf{V}$ can also be found by performing SVD on the matrix $[\hat{\mathbf{E}}_{s1}\hat{\mathbf{E}}_{s2}]$, that is

$$[\hat{\mathbf{E}}_{s1}\hat{\mathbf{E}}_{s2}] = \mathbf{U}_2\Sigma_2\mathbf{V}^H \tag{1.70}$$

1.4.2.4 Comparison of subspace based methods in nonstationary scenario

We compare the statistical performance of the six subspace based estimators: MUSIC, root-MUSIC, Min-Norm, root Min-Norm, LS-ESPRIT and TLS-ESPRIT in the presence of nonstationary sources by using computer simulations.

The location accuracy and resolution capability are used as performance indices. The resolution is the ability to distinguish closely spaced sources .

The general configuration of the simulations is a uniform linear array of ten elements ($d = \lambda/2$) with two chirp signals of unit variance arriving at $\theta_1 = -2.5$ degrees and $\theta_2 = 2.5$ degrees (angles are measured with respect to the normal of the array as indicated in Fig. 1.1) respectively.

The chirp source signals are modeled as:

$$s_1(n) = e^{j(w_{1s}n + \frac{(w_{1e}-w_{1s})}{2N}n^2)}, n = 1, 2, ..., N \tag{1.71}$$

$$s_2(n) = e^{j(w_{2s}n + \frac{(w_{2e}-w_{2s})}{2N}n^2)}, n = 1, 2, ..., N \tag{1.72}$$

The start and end discrete-time frequencies of the two chirps are chosen to be : $(w_{1s}, w_{1e}) = (0, \pi)$ rad and $(w_{2s}, w_{2e}) = (\pi, 0)$ rad.

The noise used in these simulations is zero-mean Gaussian distributed spatially and temporally white. The noise power σ_n^2 is adjusted to give the desired SNR defined as :

$$SNR = 10\log_{10}(\sigma_n^{-2})$$

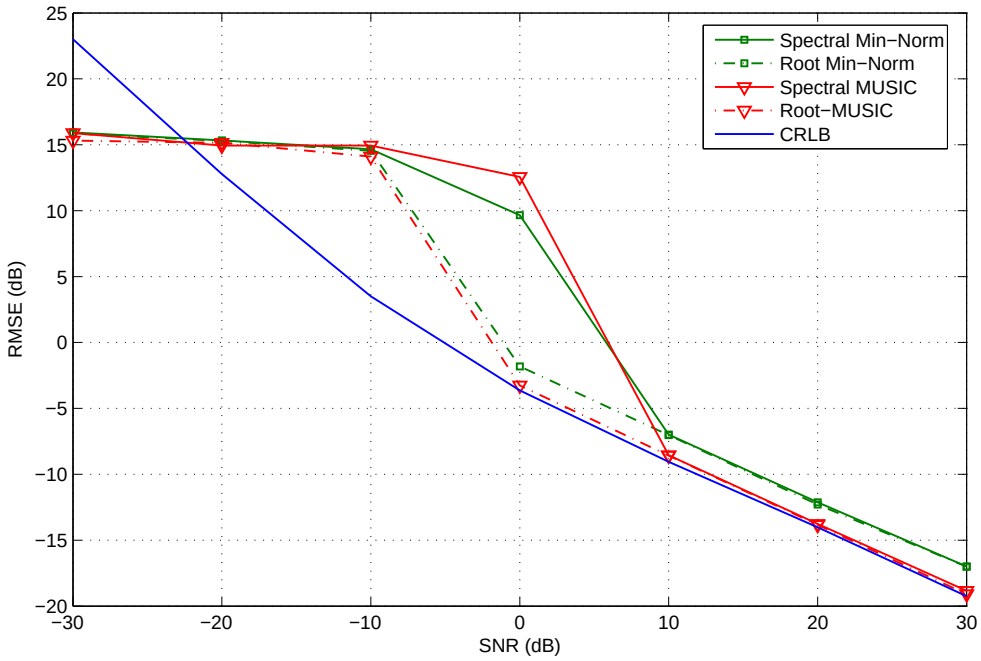

Figure 1.4: MUSIC and Min-Norm algorithms: RMSE versus SNR: N=100

1. Evaluation of the location accuracy

As a measure of location accuracy we use the root mean-squared error defined as:

$$RMSE(\theta_i) = 10\log_{10}\sqrt{\sum_{k=1}^{MC}(\hat{\theta}_i^k - \theta_i)^2} \tag{1.73}$$

where $\hat{\theta}_i^k, i = 1, 2$ are the estimate of $\theta_i, i = 1, 2$ obtained from the realisation number k. MC is the number of Monte Carlo runs (we choose $MC = 200$). In all the figures the CRLB is also plotted for comparison.

In Fig. 1.4, we show the $RMSE(\theta_1)$ versus SNR for MUSIC, Min-Norm and their polynomial versions. Above threshold values, MUSIC and root-MUSIC approach the CRLB. However, the RMSE of Min-Norm and root Min-Norm remains about $2.5dB$ above the CRLB.

In Fig. 1.5, we show $RMSE$ versus the number of snapshots (N) for $SNR = 10dB$. For this SNR root-MUSIC and root Min-Norm are above the threshold. Root-MUSIC approaches the CRLB and root Min-Norm remains $1.9dB$ above it. In both simulations the polynomial versions outperform the spectral ones.

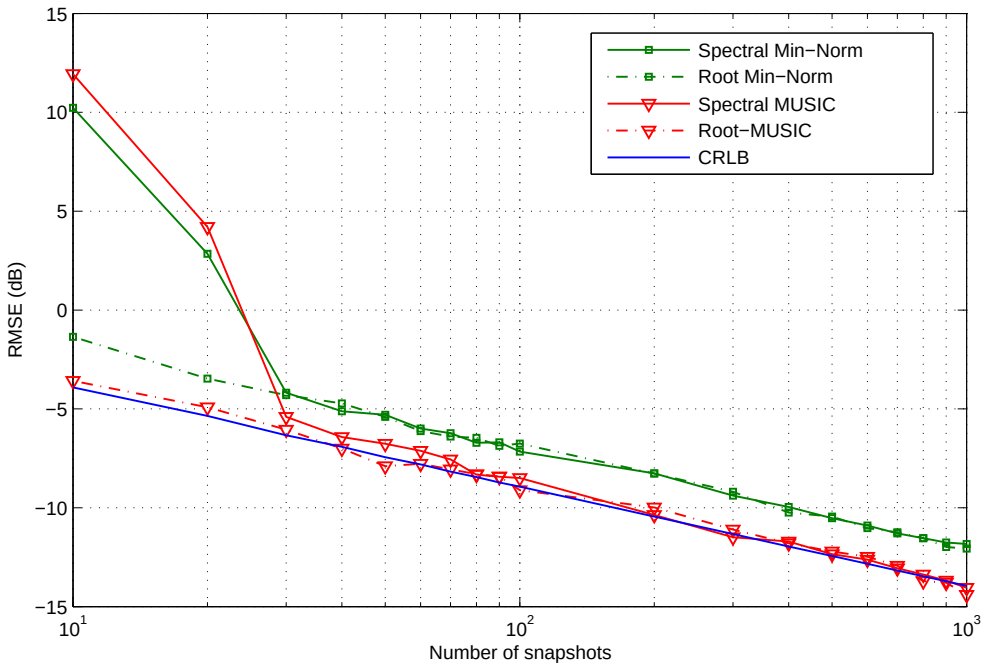

Figure 1.5: MUSIC and Min-Norm algorithms: RMSE versus N: SNR=10dB

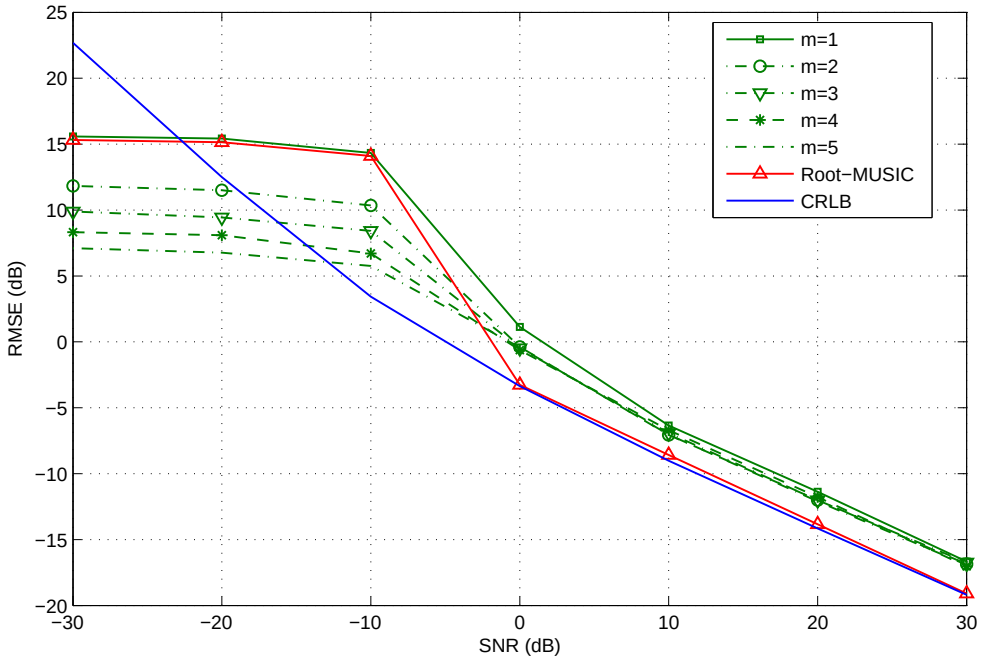

Figure 1.6: TL-ESPRIT algorithm: RMSE versus SNR: N=100

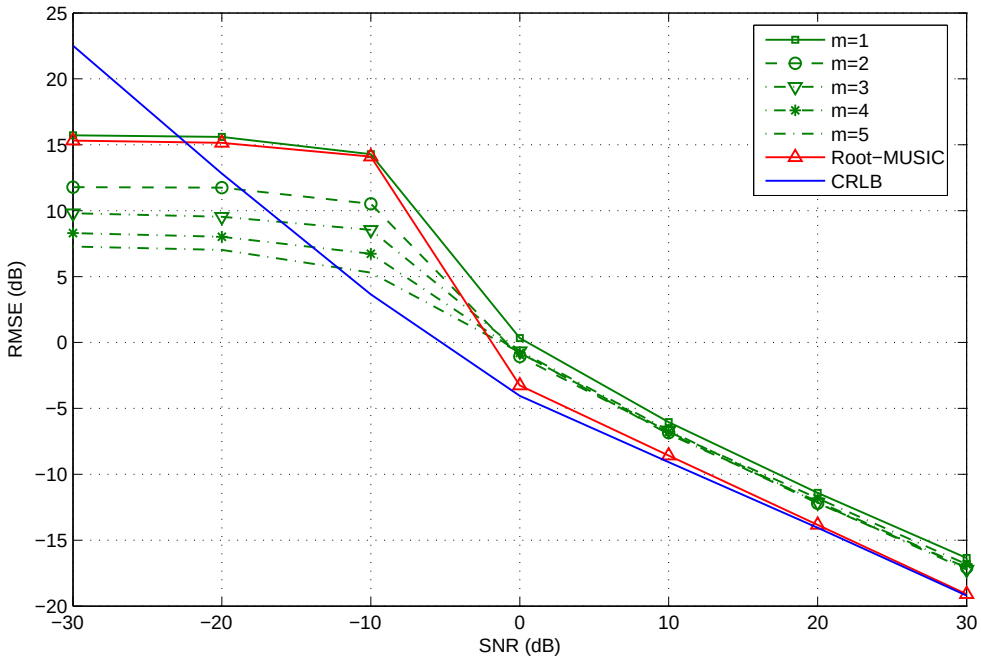

Figure 1.7: TLS-ESPRIT algorithm: RMSE versus SNR: N=100

The $RMSE$ of LS-ESPRIT and TLS-ESPRIT are shown in Figs. 1.6 and 1.7 respectively. For this simulation configuration LS-ESPRIT and TLS-ESPRIT have similar performance. For $m = 1$ the RMSE is about $3dB$ above the CRLB bound.

2. Evaluation of the resolution capability

We use the probability of resolution P_R as a measure of the resolution capability. This measure is the probability that the algorithm produces two distinct solutions $(\hat{\phi}_1, \hat{\phi}_2)$ and:

$$\mid \hat{\phi}_i - \phi_i \mid \leq \min\{\frac{\Delta\phi}{2}, \frac{2\pi}{N}\}, i = 1, 2. \tag{1.74}$$

Where $\hat{\phi}_i = 2\pi\frac{d}{\lambda}sin(\hat{\theta}_i)$ and $\Delta\phi = \mid \phi_1 - \phi_2 \mid$.

In Fig. 1.8, we show the probability of resolution versus SNR for $N = 100$. We see that spectral Min-Norm has better resolution behavior than spectral MUSIC. However, root-MUSIC has better resolution behaviour than root Min-Norm.

In Fig. 1.9 the probability of resolution versus SNR for LS-ESPRIT is plotted. The resolution performance improves as m increases. The TLS-ESPRIT (Fig. 1.10) has slightly better resolution performance than LS-ESPRIT.

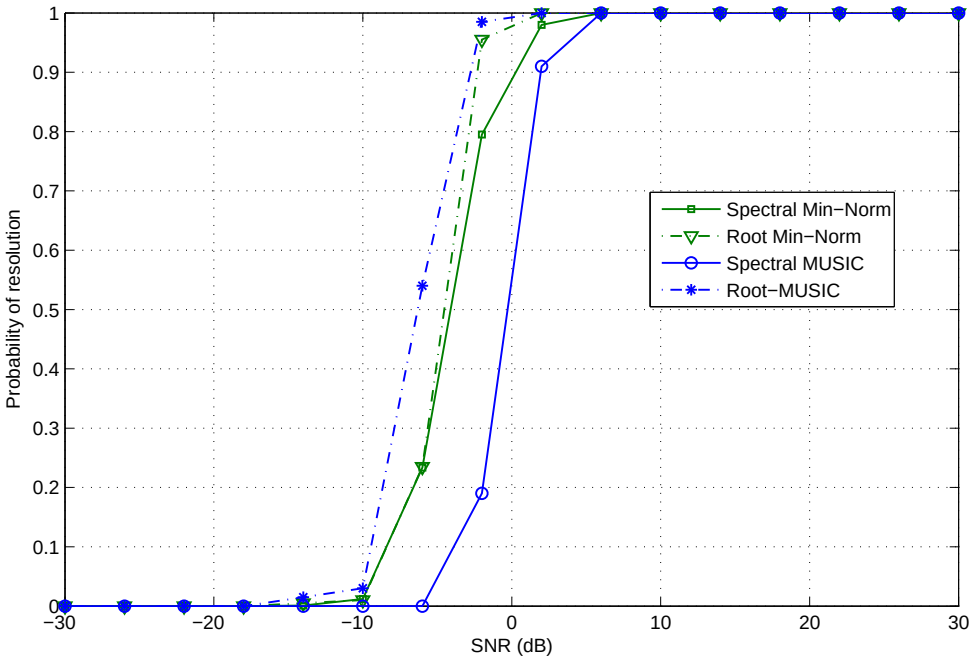

Figure 1.8: Min-Norm and MUSIC algorithms: probability of resolution versus SNR: N=100

1.4.3 Maximum likelihood technique

The subspace based methods are computationally attractive but they do not always yield sufficient accuracy. In particular, for scenarios involving highly correlated (or even coherent) signals, the performance of subspace based methods may be insufficient. Coherent signals impose no difficulties for maximum likelihood (ML) technique.

The price to pay for this increased efficiency and robustness is that the algorithm typically requires multidimensional research to find the estimates.

Two different assumptions about the emitter signals have lead to two ML approaches [21].

1.4.3.1 Deterministic maximum likelihood

The model used is the same as that given in Eq. 1.23. Furthermore, we assume that the source signals $\mathbf{s}(t)$ are deterministic and unknown.

The observation vector $\mathbf{x}(t)$ is assumed Gaussian random process, with mean $\mathbf{A}(\theta)\mathbf{s}(t)$ and covariance matrix $\sigma_n^2\mathbf{I}$. The *likelihood function* is the probability density function (PDF) of all the observations given the unknown parameters.

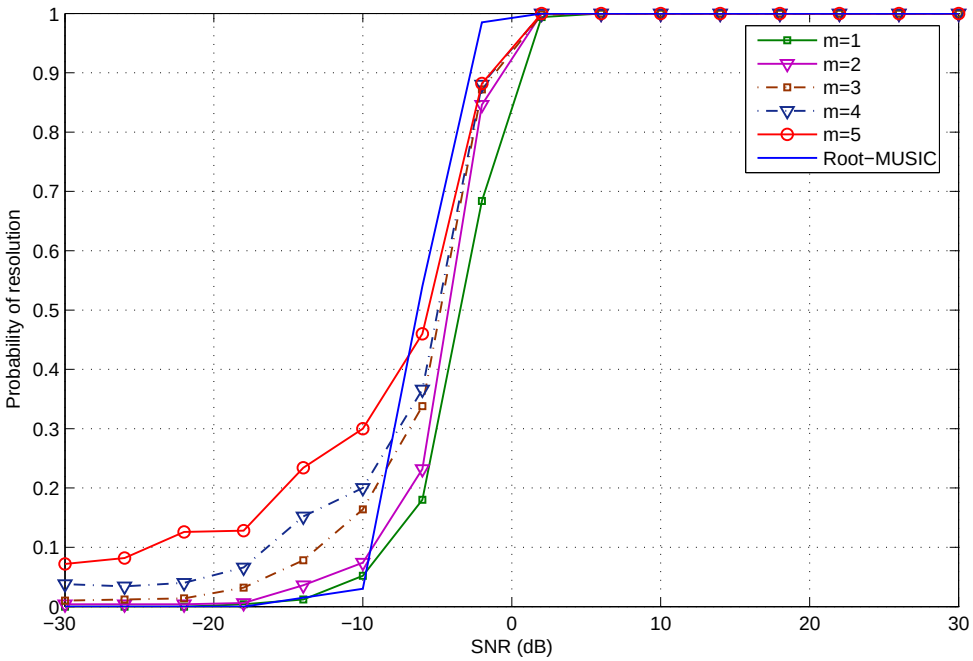

Figure 1.9: LS-ESPRIT algorithm: probability of resolution versus SNR: N=100

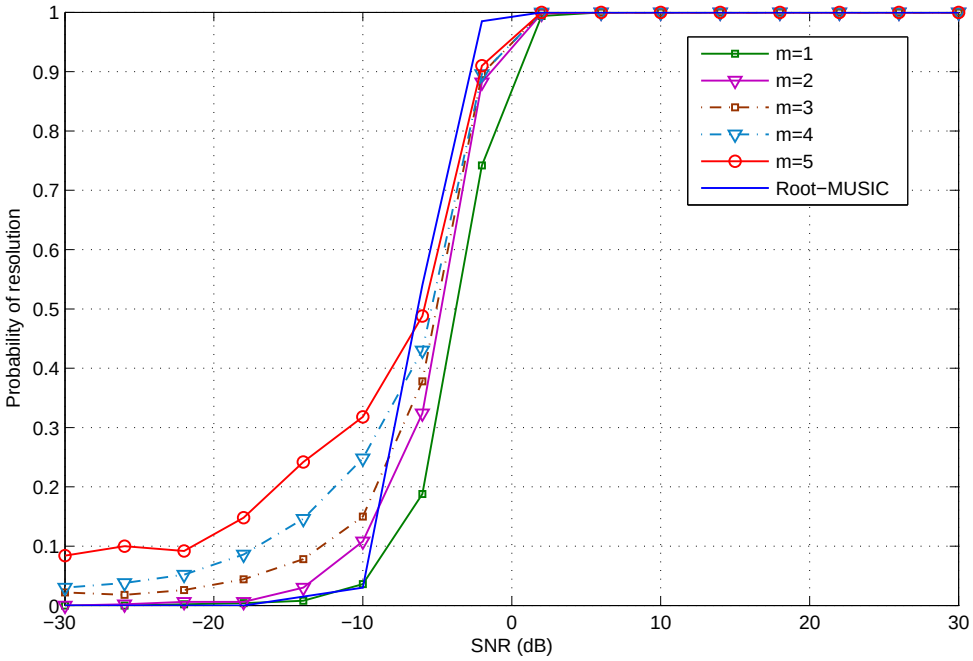

Figure 1.10: TLS-ESPRIT algorithm: probability of resolution versus SNR: N=100

The PDF of one measurement vector $\mathbf{x}(t)$ is

$$\frac{1}{(\pi\sigma_n^2)^M} e^{-\|\mathbf{x}(t)-\mathbf{A}(\theta)\mathbf{s}(t)\|^2/\sigma_n^2} \tag{1.75}$$

Since the measurement are independent, the likelihood function is obtained as

$$\mathcal{L}_{DML}(\theta, \mathbf{s}(t), \sigma_n^2) = \prod_{t=1}^{N} (\pi\sigma_n^2)^{-M} e^{-\|\mathbf{x}(t)-\mathbf{A}(\theta)\mathbf{s}(t)\|^2/\sigma_n^2} \tag{1.76}$$

The unknown parameters in the likelihood function are DOAs θ, the signal waveforms $\mathbf{s}(t)$ and the noise variance σ_n^2. The ML estimates are calculated as the maximising arguments of $Li(\theta, \mathbf{s}(t), \sigma_n^2)$ or as the minimising arguments of the negative log-likelihood function $-\log \mathcal{L}(\theta, \mathbf{s}(t), \sigma_n^2)$

After normalising by N and ignoring the independent $M \log \pi$-term, we get

$$\ell_{DML}(\theta, \mathbf{s}(t), \sigma_n^2) = M \log \sigma_n^2 + \frac{1}{\sigma_n^2 N} \sum_{t=1}^{N} \|\mathbf{x}(t) - \mathbf{A}(\theta)\mathbf{s}(t)\|^2 \tag{1.77}$$

Explicit minima with respect to $\mathbf{s}(t)$ and σ_n^2 are given by

$$\hat{\mathbf{s}}(t) = \mathbf{A}^{\dagger}\mathbf{x}(t) \tag{1.78}$$

$$\hat{\sigma}_n^2 = \frac{1}{MN} \sum_{t=1}^{N} \|\Pi_{\mathbf{A}}^{\perp}\mathbf{s}(t)\|^2 \tag{1.79}$$

$$\hat{\sigma}_n^2 = \frac{1}{M} Tr\{\Pi_{\mathbf{A}}^{\perp}\hat{\mathbf{R}}_{\mathbf{xx}}\} \tag{1.80}$$

where $\mathbf{A}^{\dagger}$ is the Moore-Penrose pseudo-inverse of $\mathbf{A}$ and $\Pi_{\mathbf{A}}^{\perp}$ is the orthogonal projection onto the null space of $\mathbf{A}^H$,i.e.,

$$\mathbf{A}^{\dagger} = (\mathbf{A}^H\mathbf{A})^{-1}\mathbf{A}^H \tag{1.81}$$

$$\Pi_{\mathbf{A}} = \mathbf{A}\mathbf{A}^{\dagger} \tag{1.82}$$

$$\Pi_{\mathbf{A}}^{\perp} = \mathbf{I} - \Pi_{\mathbf{A}} \tag{1.83}$$

Substituting Eqs. 1.80 and 1.78 into Eq. 1.77 shows that the DML signal parameter estimate are obtained by solving the following minimization problem:

$$\hat{\theta}_{DML} = \arg\min_{\theta}\{Tr\{\Pi_{\mathbf{A}}^{\perp}\hat{\mathbf{R}}_{\mathbf{xx}}\}\} = \arg\min_{\theta}\{f_{DML}(\theta)\} \tag{1.84}$$

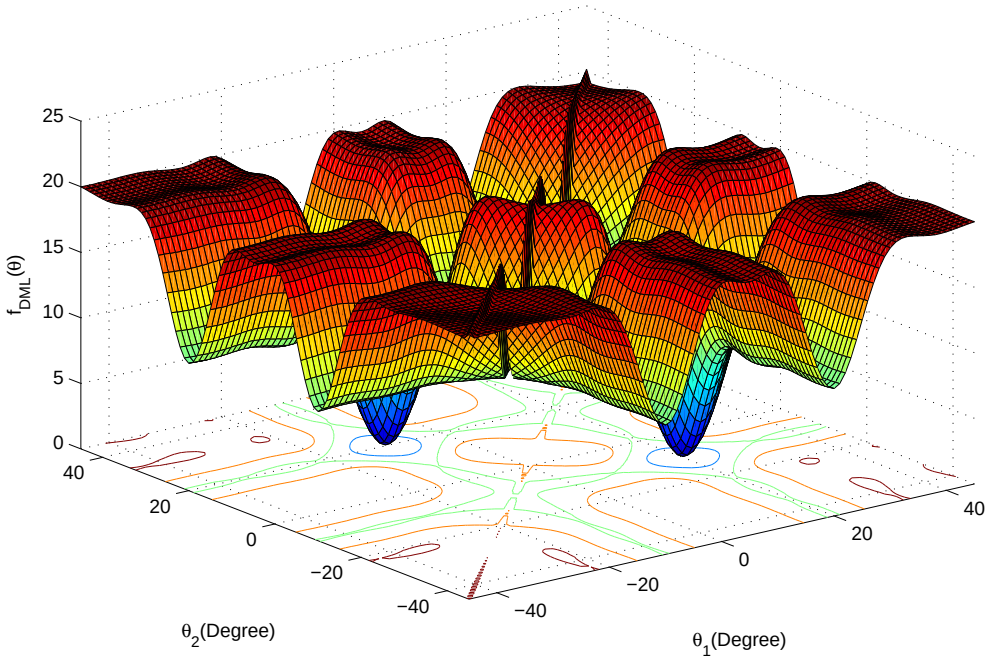

Figure 1.11: Deterministic ML: $f_{DML}(\theta)$: $SNR = 20dB$, N=100

To calculate the DML estimates, the non-linear L-dimensional optimisation problem Eq. 1.84 must be solved numerically. However the convergence of the numerical methods to the global minimum is not guaranteed if a good initial guess is not available. A subspace based methods can be used to obtain an initial estimator, provided that all the sources are resolved. Fig. 1.11 shows the function $f_{DML}(\theta)$ versus θ_1 and θ_2 when the DOAs are equal to $-10°$ and $20°$.

1.4.3.2 Stochastic maximum likelihood

The other ML technique reported in the literature is termed the stochastic maximum likelihood (SML) method. This method is obtained by modeling the signal waveforms as random process. If the signal waveforms are zero-mean Gaussian random process with second order properties

$$E\{\mathbf{s}(t)\mathbf{s}^H(s)\} = \mathbf{R_{ss}}\delta_{t,s} \tag{1.85}$$

$$E\{\mathbf{s}(t)\mathbf{s}^T(s)\} = 0 \tag{1.86}$$

Then the vector $\mathbf{x}(t)$ is white, zero-mean Gaussian random vector with covariance matrix given by Eq. 1.40

The likelihood function now, depends on θ, $\mathbf{R_{ss}}$ and σ_n^2. The stochastic ML estimate of θ is given in

[27] as :

$$\hat{\theta}_{SML} = \arg\min_{\theta}\{\log\det[\mathbf{A}\hat{\mathbf{R}}_{\mathbf{ss}_{SML}}(\theta)\mathbf{A}^H + \hat{\sigma}^2_{n_{SML}}(\theta)\mathbf{I}]\} \tag{1.87}$$

Where

$$\hat{\sigma}^2_{n_{SML}}(\theta) = \frac{1}{M-L}Tr\{\Pi^{\perp}_{\mathbf{A}}\hat{\mathbf{R}}_{\mathbf{xx}}\} \tag{1.88}$$

$$\hat{\mathbf{R}}_{\mathbf{ss}_{SML}}(\theta) = \mathbf{A}^{\dagger}(\hat{\mathbf{R}}_{\mathbf{xx}} - \hat{\sigma}^2_{n_{SML}}(\theta)\mathbf{I})\mathbf{A}^{\dagger H} \tag{1.89}$$

The SML signal parameter estimates have been shown to have a better large sample accuracy than the corresponding DML estimates, with the difference being significant for small numbers of sensors, low SNR and highly correlated signals. For Gaussian signals, the SML estimates attain the stochastic CRLB.

1.4.4 Subspace fitting methods

The Subspace Fitting methods [21] have the same statistical performance as the ML methods. However, the computational cost for these methods is less than for the ML methods.

We recall the structure of the eigendecomposition of the array covariance matrix (Eq. 1.40)

$$\mathbf{R}_{\mathbf{xx}} = \mathbf{A}\mathbf{R}_{\mathbf{ss}}\mathbf{A}^H + \sigma_n^2\mathbf{I} = \mathbf{E}_s\Lambda_s\mathbf{E}_s^H + \sigma_n^2\mathbf{E}_n\mathbf{E}_n^H \tag{1.90}$$

As previously noted, $\mathbf{E}_s$ spans the signal subspace which is the orthogonal complement of the noise subspace spanned by $\mathbf{E}_n$. The identity matrix can be expressed as

$$\mathbf{I} = \mathbf{E}_s\mathbf{E}_s^H + \mathbf{E}_n\mathbf{E}_n^H \tag{1.91}$$

canceling the term $\sigma_n^2\mathbf{E}_n\mathbf{E}_n^H$ in Eq. 1.90 then yields

$$\mathbf{A}\mathbf{R}_s\mathbf{A}^H + \sigma_n^2\mathbf{E}_s\mathbf{E}_s^H = \mathbf{E}_s\Lambda_s\mathbf{E}_s^H \tag{1.92}$$

Post-multiply the right side of Eq. 1.92 by $\mathbf{E}_s$ (note that $\mathbf{E}_s^H\mathbf{E}_s = \mathbf{I}$) and work out the obtained expression we get the following relation

$$\mathbf{E}_s = \mathbf{A}\mathbf{T} \tag{1.93}$$

where $\mathbf{T}$ is full-rank $L \times M$ matrix

$$\mathbf{T} = \mathbf{R}_s\mathbf{A}^H\mathbf{E}_s(\Lambda_s - \sigma_n^2\mathbf{I})^{-1} \tag{1.94}$$

The relation in Eq. 1.93 forms the basis for the *Signal Subspace Fitting* (SSF) approach.

Since θ and $\mathbf{T}$ are unknown, we search for the value that solve Eq. 1.93. The resulting θ will be the true DOAs.

If an estimate $\hat{\mathbf{E}}_s$ is used, we attempt to minimise some distance measure between $\hat{\mathbf{E}}_s$ and $\mathbf{AT}$. For this purpose, we use the Frobenius norm.

Then, the SSF estimate is obtained by solving the following non-linear optimisation problem:

$$\{\hat{\theta}, \hat{T}\} = \arg\min_{\theta,\mathbf{T}} \|\hat{\mathbf{E}}_s - \mathbf{AT}\|_F^2 \tag{1.95}$$

Similar to DML criteria, this is a separable nonlinear least square problem. The solution for the linear parameter $\mathbf{T}$ (for fixed unknown $\mathbf{A}$) is

$$\hat{\mathbf{T}} = \mathbf{A}^{\dagger}\hat{\mathbf{E}}_s \tag{1.96}$$

which, when substituted into Eq. 1.95 leads to the criteria function

$$\hat{\theta} = \arg\min_{\theta}\{Tr\{\Pi_{\mathbf{A}}^{\perp}\hat{\mathbf{E}}_s\hat{\Lambda}_s\hat{\mathbf{E}}_s^H\}\} \tag{1.97}$$

A weighting of the eigenvectors can also be introduced

$$\hat{\theta}_{SSF} = \arg\min_{\theta}\{Tr\{\Pi_{\mathbf{A}}^{\perp}\hat{\mathbf{E}}_s\mathbf{W}\hat{\mathbf{E}}_s^H\}\} \tag{1.98}$$

The optimal choice of $\mathbf{W}$ is given by

$$\mathbf{W}_{opt} = (\Lambda_s - \sigma_n^2\mathbf{I})^2\Lambda_s^{-1} \tag{1.99}$$

Since $\mathbf{W}_{opt}$ depends on unknown quantities, we use instead

$$\hat{\mathbf{W}}_{opt} = (\hat{\Lambda}_s - \hat{\sigma}_n^2\mathbf{I})^2\hat{\Lambda}_s^{-1} \tag{1.100}$$

The estimator defined by Eq. 1.98 with weights given by Eq. 1.100 is termed the *Weighted Subspace Fitting* (WSF) method:

$$\hat{\theta}_{WSF} = \arg\min_{\theta}\{Tr\{\Pi_{\mathbf{A}}^{\perp}\hat{\mathbf{E}}_s\mathbf{W}_{opt}\hat{\mathbf{E}}_s^H\}\} \tag{1.101}$$

An alternative subspace fitting formation is obtained by starting from the MUSIC relation of Eq. 1.43. We minimise the following *Noise Subspace Fitting* (NSF) criterion,

$$\hat{\theta}_{NSF} = \arg\min_{\theta}\{Tr\{\mathbf{A}^H \hat{E}_n \hat{E}_n^H \mathbf{A}\mathbf{V}\}\} \tag{1.102}$$

Where $\mathbf{V}$ is some positive definite weighting matrix.

1.5 Conclusion

We described four types of DOAs estimators, namely the beamforming technique, the subspace based methods, the maximum likelihood methods and the subspace fitting methods.

The performance of the beamforming estimators is limited by the physical size of the array (aperture). They can only be used to indicate the number of sources, their approximate locations and power. The subspace based methods are computationally attractive but they do not yield sufficient performance especially for low SNR or small number of snapshots. The maximum likelihood and subspace fitting techniques provide better performance than the subspace based methods. However, they are not computationally efficient as they need multidimensional search to obtain the DOAs. Although the described methods were originally developed for stationary signals, they can still be applied to nonstationary signals but they do not yield sufficient accuracy and resolution especially for low SNR or small number of snapshots.

All these approaches make no use of any available information about the signal structure. However, many nonstationary signals have a rich structure, such as the time-frequency signature, that can be used to improve the estimator performance.

Chapter 2

Time-frequency concepts

2.1 Introduction

Time **F**requency **S**ignal **A**nalysis and **P**recessing (TFSAP) represents a set of effective methods, techniques and algorithms used for analysis and processing of nonstationary signals. TFSAP is a natural extension of both the time domain and the frequency domain processing, that involves representing signals in a two dimensional space. Such representation is intended to provide a distribution of signal energy versus time and frequency simultaneously. This chapter provides a brief background on the fundamental concepts of TFSAP that will be used in the following chapter. We use the same notions and definitions used in the valuable reference [12].

2.2 Need for time-frequency representation

The two classical representations of a signal $s(t)$, are the time-domain representation, and, frequency-domain representation $S(f) = \mathcal{FT}\{s(t)\}$, where $\mathcal{FT}$ stands for the Fourier transform. Each classical representation of the signal s(t) is non localised with respect to the excluded variable. Consequently, such representations are not suitable for signals with time-varying spectral contents (nonstationary signals). For nonstationary signals, an indication as to how the frequency content of the signal changes with time, is needed. The magnitude spectrum (frequency representation) of a signal gives no indication as to how the frequency content of the signal changes with time. Time-frequency signal processing, being a natural extension of both the time domain and the frequency domain processing, preserves and reveals this information about the signal. TFSAP involves, and is intended to provide a distribution of signal energy versus both time and frequency.

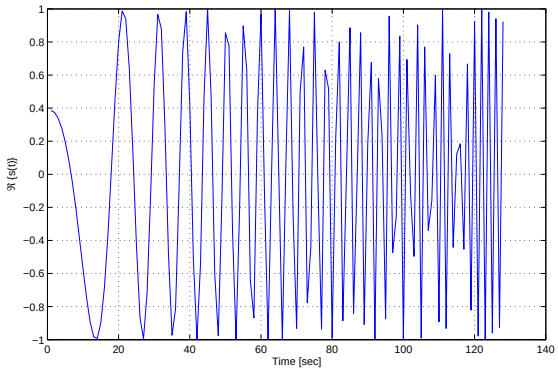

Figure 2.1: Time-domain representation of LFM signal

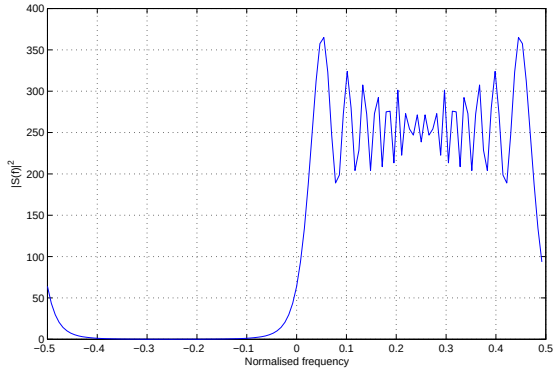

Figure 2.2: Frequency-domain representation of LFM signal

2.2.1 Limitations of classical signal representations

In order to see the inherent limitations of the classical representations of a nonstationary signal, consider a linear frequency modulated (LFM) signal $s(t)$ with length $N = 128$ and sampling frequency $f_s = 1Hz$. Its frequency increases linearly from 0.1 to 0.5 Hz. Fig. 2.1 and Fig. 2.2 show different representations of this signal.

The time representation of the LFM signal gives no indication about the frequency content of the signal, neither does the spectrum $|S(f)|^2$ as to how the spectrum of the signal changes with time. The spectrum phase contains the actual information about the internal organisation of the signal such as the order of appearance in time of the different frequencies present in the signal. The difficulties of interpreting and analyzing a phase spectrum makes the concept of a joint time-frequency representation attractive.

2.2.2 Finding hidden information using joint time-frequency representation

To overcome the inadequacies of classical representations of a nonstationary signal, which was exposed by the above example, we desire a representation in the two dimensional (t, f) space. Such a representation

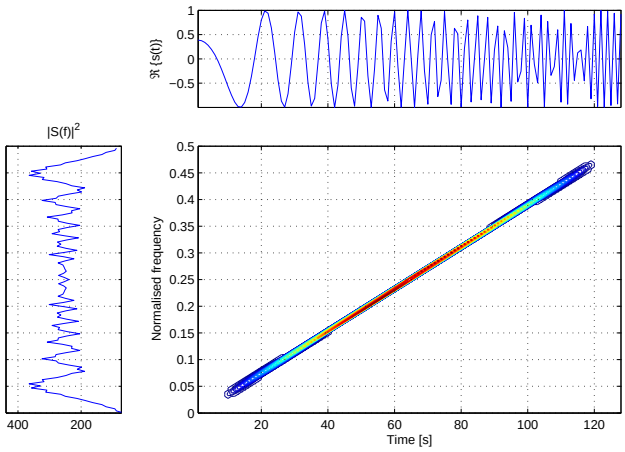

Figure 2.3: Time-frequency representation of LFM signal

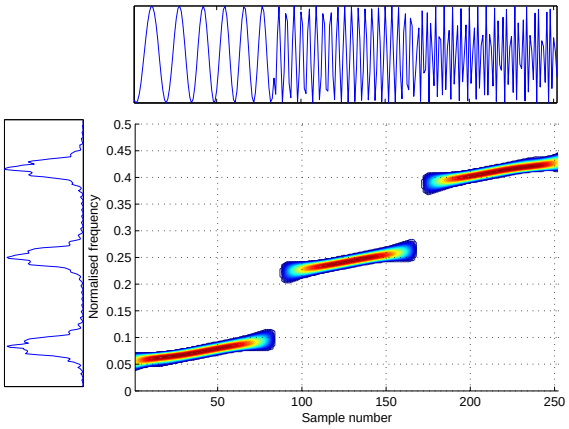

Figure 2.4: Time-frequency representation of three-components signal

is called a Time-Frequency Distribution (TFD). As an illustration, Fig. 2.3 shows one particular time-frequency representation of the LFM signal using Wigner-Ville distribution (WVD). The representation in Fig. 2.3 not only shows the start and end time instants and the frequency range of the LFM signal, but also clearly shows the time variation of the frequency content of the signal. The latter feature, which shows the frequency at a given time or the time at which a given frequency is present, is missing from the conventional signal representations in Fig. 2.1 and Fig. 2.2.

Fig. 2.4 also indicates another significant reason to use the time-frequency representation of signals: it reveals whether the signal is monocomponent or multicomponent, a fact that cannot be revealed by the two conventional representations especially when individual components are also time varying. Using the TFD, the start and end time instants as well as the time variation of frequency content of each component of the signal are clearly identifiable.

2.3 Time-frequency distributions

2.3.1 Instantaneous Frequency and Group Delay

The IF, $f_i(t)$, of a monocomponent signal is a measure of the localisation in time of the individual frequency components of the signal. The IF of a monocomponent analytic signal $z(t) = a(t)e^{j\varphi(t)}$ is given by [12]

$$f_i(t) = \frac{1}{2\pi}\frac{d\varphi(t)}{dt} \tag{2.1}$$

The IF of a monocomponent real signal $s(t) = a(t)\cos\varphi(t)$ is defined as the IF of the analytic signal $z(t)$ corresponding to $s(t)$. When a signal has multiple components, the expression of the IF needs to be applied to its individual components to give a meaningful physical interpretation.

The time delay (TD), $\tau_d(f)$, is the twin of the IF concept in the frequency domain. The TD of a monocomponent analytic signal $z(t)$ is defined as

$$\tau_d(f) = -\frac{1}{2\pi}\frac{d\theta(f)}{df} \tag{2.2}$$

where

$$Z(f) = \mathcal{FT}(z(t)) = A(f)e^{j\theta(f)} \tag{2.3}$$

The TD of a monocomponent real signal is also defined as the TD of the analytic signal corresponding to the real signal. The TD gives the order of appearance of each time-varying frequency component. The mean value of the individual TDs, called group delay, gives the global order of appearance of the frequencies.

2.3.2 Desirable properties of a TFD

The TFD is expected to visualise in the time-frequency domain the time-frequency law of each signal component in order to make the estimation of IF and TD easier. The TFD should also provide additional information about relative component amplitudes, and the central spread of the components around the IF.

The TFD is also expected to satisfy a certain number of properties that are desirable for practical analysis. If $\rho_z(t,f)$ is the TFD of signal $z(t)$, $\rho_z(t,f)$ is expected to satisfy the following properties:

- P1a: The TFD should be real and its integration over the whole time-frequency domain gives the total signal energy E_z:

$$\int_{-\infty}^{+\infty}\int_{-\infty}^{+\infty}\rho_z(t,f)dtdf = E_z \tag{2.4}$$

- P1b: It is desirable that the energy in a certain region R in the TF plane, E_{z_R}, be expressible in a similar way as Eq. 2.4, but with restriction of the integration limits to the boundaries $(\Delta t, \Delta f)$ of the region R:

$$E_{z_R} = \int_{\Delta t} \int_{\Delta t} \rho_z(t, f) dt df \tag{2.5}$$

  which is a portion of signal energy in the band Δf and time interval Δt

- P2: The peak of the TFD and the first moment of the time-frequency representation w.r.t. frequency should be equal to the IF of a monocomponent signal:

$$f_i(t) = \frac{\int_{-\infty}^{+\infty} f \rho_z(t, f) df}{\int_{-\infty}^{+\infty} \rho_z(t, f) df} \tag{2.6}$$

- P3: For multicomponent signals, the peaks of the TFDs should exhibit the various IF laws of individual components without nuisance or ghost terms or interferences.

There are some other properties, which were early considered as strictly needed, but were found later unimportant. For example, the marginal conditions given by Eqs. 2.7 and 2.8 and the positivity.

$$\int_{-\infty}^{+\infty} \rho_z(t, f) dt = |S_z(f)|^2 \tag{2.7}$$

$$\int_{-\infty}^{+\infty} \rho_z(t, f) df = |z(t)|^2 \tag{2.8}$$

2.3.3 Spectrogram

To study the spectral properties of the signal at time t, an intuitive approach is to, first, take a slice of the signal by applying a moving window centered at time t to the signal, and then calculate the magnitude spectrum of the windowed signal. Consider a signal $s(\tau)$ and a real, even window $h(\tau)$, whose $\mathcal{FT}s$ are $S(f)$ and $H(f)$ respectively. To obtain a localized spectrum of $s(\tau)$ at time $\tau = t$, multiply the signal by the window $h(\tau)$ centred at time $\tau = t$.

$$s_h(t, \tau) = s(\tau) h(\tau - t) \tag{2.9}$$

and then take the $\mathcal{FT}$ w.r.t. τ.

$$S_h(t, f) = \mathcal{FT}_{\tau \to f}\{s(\tau) h(\tau - t)\} \tag{2.10}$$

$S_h(t,f)$ is called the Short-Time Fourier Transform (STFT). The squared magnitude of the STFT, denoted by $\rho_{SPEC}(t,f)$ is called the spectrogram $(SPEC)$. It is mathematically expressed as

$$\rho_{SPEC}(t,f) = |S(t,f)|^2 = |\int_{-\infty}^{+\infty} s(\tau)h(\tau - t)e^{-j2\pi f\tau}d\tau|^2 \tag{2.11}$$

where $S(t,f)$ is the STFT. By varying t, one can obtain the spectral density as a function of t.

The SPEC is a simple, popular and robust method in the analysis of nonstationary signals. It is a proper energy distribution in the sense that it is positive. On the other hand, the SPEC has an inherent limitation : the frequency resolution is dependent on the length (and the type) of the analysis window; too short windows cause a decrease in frequency resolution, and too long windows cause a decrease in time resolution, thus an inherent trade-off between time and frequency resolution in the SPEC for a particular window.

2.3.4 Wigner-Ville distribution

For a monocomponent signal, $z(t)$, we expect the WVD to exhibit the IF law of $z(t)$ in the (t,f) plane. Since the WVD is a function of the frequency f and represents a sort of spectrum we may reasonably require the distribution to be the $\mathcal{FT}$ of some function related to the $z(t)$. This function is called ***signal kernel*** or the ***Instantaneous Autocorrelation Function (IAF)*** and it is given the symbol K_z. So the signal kernel, $K_z(t,\tau)$, and the WVD, $W_z(t,f)$, are related by:

$$W_z(t,f) = \mathcal{FT}_{\tau\to f}\{K_z(t,\tau)\} \tag{2.12}$$

Since we would like the WVD of $z(t)$ at any given time to be a unit delta function at the IF, then

$$W_z(t,f) = \delta(f - f_i(t)) \tag{2.13}$$

where $f_i(t) = \frac{\varphi^{'}(t)}{2\pi}$ is the IF of the analytic monocomponent FM signal $z(t) = e^{j\varphi(t)}$.
From Eq. 2.12, we obtain

$$K_z(t,\tau) = \mathcal{FT}^{-1}_{\tau\leftarrow f}\{\delta(f - f_i(t))\} = e^{j2\pi f_i(t)\tau} \tag{2.14}$$

$$= e^{j\varphi^{'}(t)\tau} \tag{2.15}$$

Using the central finite-difference (CFD) approximation, we obtain

$$\varphi^{'}(t) \approx \frac{1}{\tau}[\varphi(t+\tau/2) - \varphi(t-\tau/2)] \tag{2.16}$$

Substituting Eq. 2.16 into Eq. 2.15 and using the expression of $z(t)$ gives the signal kernel expression:

$$K_z(t,\tau) = z(t+\tau/2)z^*(t-\tau/2) \tag{2.17}$$

then

$$W_z(t,f) = \int_{-\infty}^{+\infty} z(t+\tau/2)z^*(t-\tau/2)e^{-j2\pi f\tau}d\tau \tag{2.18}$$

The WVD is the basis TFD because the other TFDs can be written as a filtered WVD using a specific time-lag kernel. In addition, the WVD gives unbiased estimate of the IF of a chirp signal. These are some of the reasons why the WVD is the most widely studied TFD. Furthermore, it has some interesting properties, in addition to those listed in section 2.3.2, such as [12]:

- **Time-shift invariance**: A time shift in the signal causes the same time shift in the VWD:

$$z_r(t) = z(t-t_0) \tag{2.19}$$

  then

$$W_{z_r}(t,f) = W_z(t-t_0,f) \tag{2.20}$$

- **Frequency-shift invariance**: A frequency shift in the signal causes the same frequency shift in the VWD:

$$z_r(t) = z(t)e^{j2\pi f_0 t} \tag{2.21}$$

  then

$$W_{z_r}(t,f) = W_z(t,f-f_0) \tag{2.22}$$

- **Time support**: The time support of $W_z(t,f)$ is limited by the duration of $z(t)$.

- **Frequency support**: The frequency support of $W_z(t,f)$ is limited by the bandwidth of $z(t)$.

- **Invertibility**: if $W_z(t,f)$ is the WVD of the signal $z(t)$, then

$$\int_{-\infty}^{+\infty} W_z(t,f)e^{j2\pi ft}df = z(t)z^*(0) \tag{2.23}$$

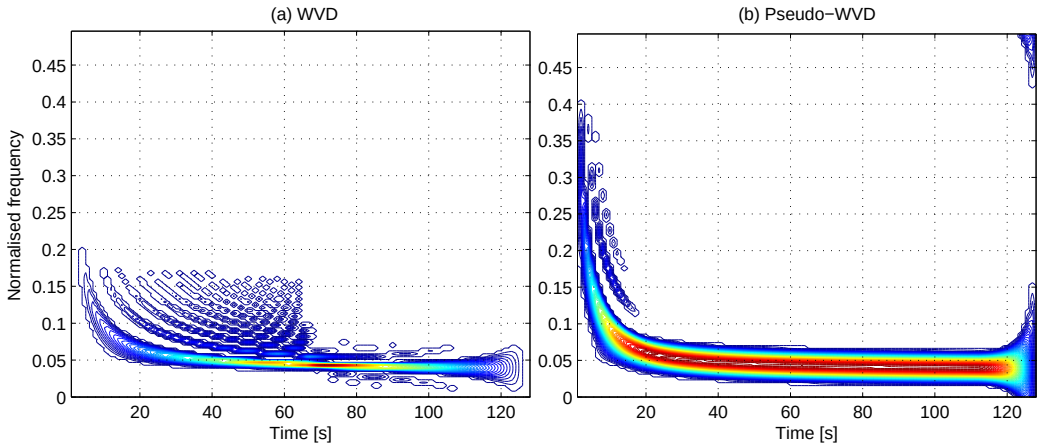

Figure 2.5: The WVD and Pseudo-WVD of a hyperbolic FM signal

2.3.4.1 Limitations of the WVD

The WVD has some drawbacks. It may have large negative values. In addition, since the distribution is bilinear rather than linear, it suffers from spurious effects called **artifacts**. They appear midway between true signal components in the case of multicomponent signals and non-linear mono- and multicomponent FM signals. There are two types of artifacts: inner and outer artifacts.

2.3.4.1.1 Inner artifacts

Inner artifacts are produced when the WVD is applied to mono- or multicomponent non-linear FM signal because the CFD approximation is not exact. The CFD approximation is exact for monocomponent linear FM signal only. This is why the WVD gives an accurate representation of the IF law of linear FM signals.

For example, Fig. 2.5(a) shows the WVD of a monocomponent hyperbolic FM signal. The crest of the WVD seems to be a reasonable approximation to the IF law but there are many spurious ridges which represent the inner artifacts. These artifacts alternate in sign as we move *normal* to the IF law in the (t,f) plane. The inner artifacts can be reduced by windowing the IAF in τ before taking the $\mathcal{FT}$ leading to the pseudo-WVD (Fig. 2.5 (b)). But this causes loss of resolution.

2.3.4.1.2 Outer artifacts

If $z(t)$ is a multicomponent signal, the algebraic expansion of $K_z(t,\tau)$ contains cross-product terms which, when Fourier-transformed, give rise to spurious features in WVD. These are the ***outer artifacts*** or ***cross-terms***. To explain this we consider the signal $z(t)$ defined as

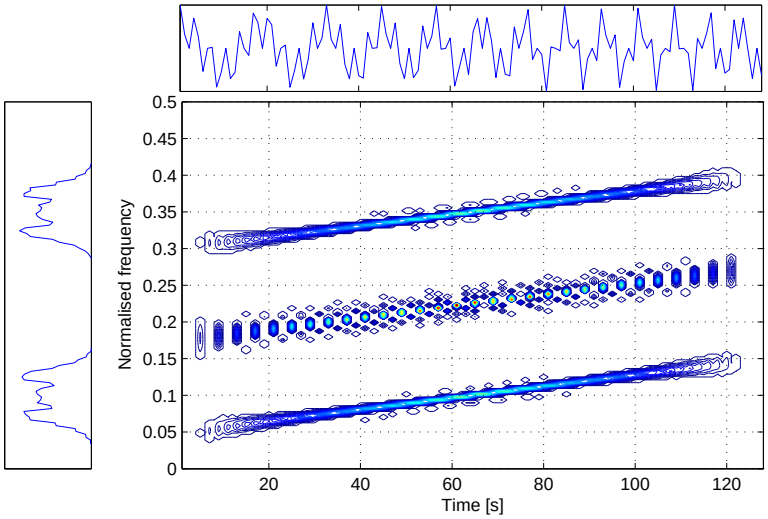

Figure 2.6: The WVD of the sum of two LFM signals

$$z(t) = z_1(t) + z_2(t) \tag{2.24}$$

Expanding the IAF, we obtain

$$K_z(t,\tau) = K_{z_1}(t,\tau) + K_{z_2}(t,\tau) + K_{z_1 z_2}(t,\tau) + K_{z_2 z_1}(t,\tau) \tag{2.25}$$

Where $K_{z_1 z_2}(t,\tau)$ and $K_{z_2 z_1}(t,\tau)$ are the "signal cross-kernels" or instantaneous cross-correlation functions.

Taking the $\mathcal{FT}$ of Eq. 2.25 w.r.t. τ, we find

$$W_z(t,f) = W_{z_1}(t,f) + W_{z_2}(t,f) + 2\Re\{W_{z_1 z_2}(t,f)\} \tag{2.26}$$

Where $W_{z_1}(t,f)$ and $W_{z_2}(t,f)$ are the WVDs of $z_1(t)$ and $z_2(t)$, and $W_{z_1 z_2}(t,f)$ is the cross-Wigner-Ville Distribution (XWVD) of $z_1(t)$ and $z_2(t)$, defined by

$$W_{z_1 z_2}(t,f) = \int_{-\infty}^{+\infty} z_1(t+\tau/2) z_2^*(t-\tau/2) e^{-j2\pi f\tau} d\tau \tag{2.27}$$

Thus the WVD of the sum of two signals is not just the sum of the signal's WVDs, but also their XWVDs. If $z_1(t)$ and $z_2(t)$ are monocomponent signals, $W_{z_1}(t,f)$ and $W_{z_2}(t,f)$ are ***the auto-terms***, while $\Re\{W_{z_1 z_2}(t,f)\}$ is ***the cross-term***.

Fig. 2.6 shows the WVD of the sum of two parallel LFM signals. There seem to be three components rather than two: the "extra" component at the mean frequency of the expected components has a large oscillating amplitude, and occurs in a region of the (t, f) plane where we expect no energy at all. These cross-terms alternate in sign as we move *parallel* to the expected features in the (t, f) plane. The cross-terms make the interpretation of the WVD difficult. In addition, the cross-terms between noise and signal components exaggerate the effect of noise and cause a degradation of the performance as the SNR decreases. For these reasons, there has been a desire to reduce them. Multiplying the VWD by the spectrogram, using a reference signal or selecting the suitable time-lag kernels (Reduced Interference Distributions) are some of the available methods to attenuate these cross-terms [12].

2.3.4.2 Pseudo-WVD

The definition of Eq. 2.18 requires the knowledge of $K_z(t, \tau)$ from $\tau = -\infty$ to $\tau = +\infty$, which can be a problem in practice. That is why we often replace $K_z(t, \tau)$ in Eq. 2.18 by a windowed version of it, leading to the new distribution :

$$PW_z(t, f) \triangleq \int_{-\infty}^{+\infty} h(\tau) z(t + \tau/2) z^*(t - \tau/2) e^{-j2\pi f \tau} d\tau \tag{2.28}$$

where $h(\tau)$ is a regular window. This distribution is called the pseudo Wigner-Ville distribution (PWVD) or the windowed WVD.

The discrete form of the PWVD of a signal $z(t)$, using a rectangular window of length L_h, is given by

$$PW_z(t, f) = \sum_{\tau=-\frac{L_h-1}{2}}^{\frac{L_h-1}{2}} z(t + \tau) z^*(t - \tau) e^{-j4\pi f \tau} \tag{2.29}$$

2.3.5 Quadratic class of TFDs

The quadratic class of TFDs may be considered as the class of *smoothed* Wigner-Ville Distributions. The smoothing operation is described in the (t, f) domain by convolution with time-frequency kernel function $\gamma(t, f)$, and in other domains by multiplication and/or convolution with various transform of $\gamma(t, f)$. The kernel determines the TFD and its properties. We can obtain a TFD with certain desired properties by properly constraining the kernel function.

2.3.5.1 Time, lag, Doppler and frequency domains

For any analytic signal $z(t)$, the IAF was defined in Eq. 2.17 as

$$K_z(t, \tau) = z(t + \tau/2) z^*(t - \tau/2) \tag{2.30}$$

The IAF uses two variables : the time t and the time lag τ. If we take the dual domain of t and τ in the frequency, we obtain the frequency variables ν (Doppler) and f (frequency). This allows us to have four possible domains of representation: $(t,\tau),(t,f),(\nu,f)$ and (ν,τ).

The WVD is obtained by applying the $\mathcal{FT}_{\tau\to f}$ to IAF:

$$W_z(t,f) = \mathcal{FT}_{\tau\to f}\{K_z(t,\tau)\} \tag{2.31}$$

The $\mathcal{FT}_{t\to\nu}$ of the WVD defines the ***spectral autocorrelation function*** (SAF) as

$$\kappa_z(\nu,f) = \mathcal{FT}_{t\to\nu}\{W_z(t,f)\} \tag{2.32}$$

The $\mathcal{FT}_{t\to\nu}$ of the IAF $K_z(t,\tau)$ equals the $\mathcal{FT}^{-1}_{\tau\leftarrow f}$ of the SAF $\kappa_z(\nu,f)$, and defines the symmetrical ***ambiguity function*** (AF) as:

$$A_z(\nu,\tau) = \mathcal{FT}_{t\to\nu}\{K_z(t,\tau)\} = \mathcal{FT}^{-1}_{\tau\leftarrow f}\{\kappa_z(\nu,f)\} \tag{2.33}$$

If we represent $\mathcal{FT}s$ by arrows labeled with the participating variables, Eqs. 2.30 to 2.33 may be combined into a single graphical equation

$$\begin{array}{ccc} W_z(t,f) & \xrightarrow[\nu]{t} & \kappa_z(\nu,f) \\ \tau\uparrow f & & \tau\uparrow f \\ K_z(t,\tau) & \xrightarrow[\nu]{t} & A_z(\nu,\tau) \end{array}$$

This single graphical representation of several equations is very useful in that it links several known methods by simple $\mathcal{FT}$ operations.

we can represent similarly the TFD kernel in these four domains by taking various $\mathcal{FT}$ operations on the ***time-lag kernel*** $G(t,\tau)$:

$$\begin{array}{ccc} \gamma(t,f) & \xrightarrow[\nu]{t} & \mathcal{G}(\nu,f) \\ \tau\uparrow f & & \tau\uparrow f \\ G(t,\tau) & \xrightarrow[\nu]{t} & g(\nu,\tau) \end{array}$$

We refer to $g(\nu,\tau)$ as the ***Doppler-lag kernel***, to $\mathcal{G}(\nu,f)$ as the ***Doppler-frequency kernel***, and to $\gamma(t,f)$ as the ***time-frequency kernel***.

The ***smoothed IAF*** is defined as

$$R_z(t,\tau) = G(t,\tau) \star_t K_z(t,\tau) \tag{2.34}$$

We define the class of ***quadratic TFDs*** (smoothed WVDs) as

$$\rho_z(t,f) = \mathcal{FT}_{\tau\to f}\{R_z(t,\tau)\} \tag{2.35}$$

$$= \int\int_{-\infty}^{+\infty} G(t-u,\tau)z(u+\tau/2)z^*(u-\tau/2)e^{-j2\pi f\tau}dud\tau \tag{2.36}$$

Eq. 2.35 is usually used for the implementation of TFDs because of its simplicity.

The following diagram shows the relationship between the different representations of any smoothed WVD.

$$\begin{array}{ccc} \rho_z(t,f) & \xrightarrow[\nu]{t} & r_z(\nu,f) \\ \tau\uparrow f & & \tau\uparrow f \\ R_z(t,\tau) & \xrightarrow[\nu]{t} & \mathcal{A}(\nu,\tau) \end{array}$$

Where $r_z(\nu,f)$ is the ***generalised SAF*** and $\mathcal{A}(\nu,\tau)$ is ***the generalised ambiguity function*** GAF which are related to the kernel and signal representations as follows

$$\mathcal{A}(\nu,\tau) = g(\nu,\tau)A(\nu,\tau) \tag{2.37}$$

$$r_z(\nu,f) = \mathcal{G}(\nu,f) \star_f \kappa_z(\nu,f) \tag{2.38}$$

$\rho_z(t,f)$ can also be expressed as a double convolution of WVD of $z(t)$, $W_z(t,f)$, and the time-frequency kernel function $\gamma(t,f)$.

$$\rho_z(t,f) = W_z(t,f) \star_t \star_f \gamma(t,f) \tag{2.39}$$

$$= \int_{-\infty}^{+\infty}\int_{-\infty}^{+\infty} W_z(t-t',f-f')\gamma(t',f')dt'df' \tag{2.40}$$

Eq. 2.39 defines the quadratic class of TFDs in terms of the WVD and the time-frequency kernel. For this reason, the WVD is considered as the basic or prototype quadratic TFD, and the other quadratic TFDs are filtered version of it.

The quadratic TFDs can also be defined in terms of the Doppler-lag kernel $g(t,\tau)$ or in terms of the Doppler-frequency kernel $\mathcal{G}(\nu,f)$ and the signal spectrum.

$$\rho_z(t,f) = \int\int\int g(\nu,\tau)z(u+\tau/2)z^*(u-\tau/2)e^{j2\pi(\nu t-\nu u+f\tau)}dud\nu d\tau \tag{2.41}$$

$$\rho_z(t,f) = \int_{-\infty}^{+\infty}\int_{-\infty}^{+\infty} \mathcal{G}(\nu, f-f')Z(f'+\nu/2)Z^*(f'-\nu/2)e^{j2\pi\nu t}df'd\nu \tag{2.42}$$

The interest of the formulation given by Eq. 2.42 is that the TFDs of narrow-band signals expressed by their spectra may be more efficiently computed in this form.

2.3.5.2 Reduced interference distribution

Since the cross-terms in the (t,f) domain tend to be highly oscillatory, the corresponding terms in the dual (ν,τ) domain tend to be far from the origin (high-pass). On the other hand, the auto-terms in the (t,f) domain tend to be smooth, so the corresponding terms in the dual (ν,τ) domain are concentrated about the origin (low-pass). Therefore, the cross-terms in the ambiguity domain can be filtered out by selecting a kernel filter $g(\nu,\tau)$ that attenuates information far from the origin of the Doppler-lag domain. The TFDs properties are equivalent to constraints on the kernel filter, and most of these constraints are conveniently expressed in the ambiguity domain. For these reasons, the design of the filter kernel is performed in the ambiguity domain. The resulting kernel is then expressed in the time-lag domain for the TFD implementation (Eq. 2.35).

The corresponding TFDs to the filter kernels which reduce cross-terms are known as *Reduced Interference Distributions* (RID). Examples of time-frequency RID include the Choi-Williams distribution (CWD), the Born-Jordan distribution (BJD), the B-distribution (BD) and its modified version (MBD)and the cone-shaped Zhao-Atlas-Marks distribution (ZAMD).

Table 2.1 lists some common quadratic TFDs and their corresponding kernels given in the Doppler-lag and time-lag domains.

2.3.5.2.1 Choi-Williams distribution

The kernel of the Choi-Williams distribution (Gaussian distribution) is a two-dimensional Gaussian function centred around the origin of the ambiguity plane. This kernel is defined as

$$g(\nu,\tau) = e^{\frac{-\nu^2\tau^2}{\sigma}} \tag{2.43}$$

The spread of the kernel is controlled by the parameter σ (controlling the amount of cross-terms reduction and auto-terms resolution). When σ is large the Choi-Williams distribution is close to the Wigner-Ville distribution. Decreasing σ attenuates the cross-terms, but spreads $\gamma(t,f)$, which reduces the time-frequency resolution of the distribution. Fig. 2.7 shows that the cross-terms of two LFM signals disappear when the Wigner-Ville distribution of Fig. 2.6 is smoothed by a Choi-Williams kernel having a sufficiently small σ ($\sigma = 0.2$). The energy of the two LFM signals is spread over wider time-frequency bands but cross-terms are attenuated.

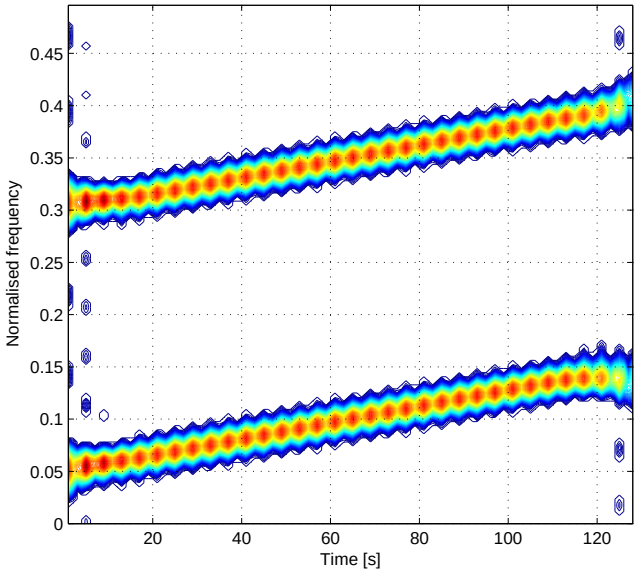

Figure 2.7: The CWD of the sum of two LFM signals

Distribution	**Doppler-lag Kernel**: $g(\nu,\tau)$	**Time-lag kernel**: $G(t,\tau)$
Wigner-Ville	1	$\delta(t)$
PWV	$h(\tau)$	$\delta(t)h(\tau)$
Spectrogram	$\int_{-\infty}^{+\infty} h(u+\frac{\tau}{2})h^*(u-\frac{\tau}{2})e^{-j2\pi\nu u}du$	$h(t+\tau/2)h^*(t-\tau/2)$
Choi-Williams	$e^{-\nu^2\tau^2/\sigma}$	$\frac{\sqrt{\pi\sigma}}{\lvert\tau\rvert}e^{-\pi^2\sigma t^2/\tau^2}$
Born-Jordan	$sinc(2\alpha\nu\tau)$	$\frac{1}{\lvert 2\alpha\tau\rvert}rect\frac{t}{2\alpha\tau}$
ZAM	$h(\tau)\frac{a}{2\lvert\tau\rvert}sinc\frac{2\nu\tau}{a}$	$h(\tau)rect\frac{t}{2\tau/a}$
B	$\frac{\lvert\tau\rvert^\beta\lvert\Gamma(\beta+j\pi\nu)\rvert^2}{2^{1-2\beta}\Gamma(2\beta)}$	$\lvert\tau\rvert^\beta\cosh^{-2\beta}t$
MB	$\frac{\lvert\Gamma(\beta+j\pi\nu)\rvert^2}{\Gamma^2(\beta)}$	$\frac{\cosh^{-2\beta}t}{\int_{-\infty}^{+\infty}\cosh^{-2\beta}\zeta d\zeta}$
Rihaczek	$e^{-j\pi\nu\tau}$	$\delta(t-\tau/2)$
Page	$e^{-j\pi\nu\lvert\tau\rvert}$	$\delta(t-\lvert\tau/2\rvert)$
Levin	$\cos(\pi\nu\tau)$	$\frac{1}{2}[\delta(t+\tau/2)+\delta(t-\tau/2)]$

Table 2.1 : Some common TFDs and their filter kernels

2.4 Conclusion

In this chapter we introduced the concept of TFD. We showed that the Wigner-Ville distribution is optimal for energy concentration about the IF for a monocomponent linear FM signal. However, if the IF of the monocomponent FM signal is not linear or the signal is multicomponent, the WVD suffers from inner and outer artifacts respectively. The use of smoothing kernels allow the attenuation of artifacts but they reduce the time-frequency resolution of the distribution.

Chapter 3

Time-frequency DOAs estimation

3.1 Introduction

In this chapter, we describe the time-frequency DOAs estimation methods obtained from the combination of DOAs estimation methods based on second-order statistics applied to the temporal representation of the signal (chapter one) and the time-frequency distributions (chapter two). Some examples are given to illustrate the usefulness of the time-frequency methods. The use of joint-block diagonalisation , time-frequency averaging, the issue of noise, auto- and cross-terms detection in the time-frequency domain are also covered in this chapter.

3.2 Time-frequency array signal processing

Conventional array processing algorithms assume stationary signals and mainly employ the covariance matrix of the data array. When the frequency content of the measured signals is time varying (nonstationary signals), this class of approaches can still be applied. However, the achievable performances are reduced with respect to those that would be achieved in a stationary environment.

Instead of considering the nonstationarity as a shortcoming and trying to design algorithm robust with respect to nonstationarity, it would be better to take advantage of the nonstationarity by considering it as a source of information. The latter can then be exploited in the design of efficient algorithms in such nonstationary environment.

The exploitation of the nonstationarity can be done by using the Spatial Time-Frequency Distributions (STFDs), which are a generalisation of the TFDs to a vector of multisensor signals. Under linear model, the STFDs and the commonly known covariance matrix exhibit the same eigenstructure.

Algorithms based on the TFDs properly use the time-frequency information to significantly improve performance. This improvement comes essentially from the fact that the effects of spreading the noise

power while localizing the source energy in the time-frequency domain increase the signal-to-noise ratio (SNR).

STFD based algorithms exploit the time-frequency representation of the signals together with the spatial diversity provided by the multiantenna.

The concept of STFD was introduced for the first time in 1996 [8]. It was used successfully in solving the problem of blind separation of nonstationary signals [10]. This concept was then applied to solve the problem of DOA estimation [9].

3.2.1 Spatial time-frequency distributions

The quadratic class of STFD matrix of a signal vector $\mathbf{x}(t)$ is obtained from Eq. 2.41 as

$$\mathbf{D_{xx}}(t,f) = \int_{-\infty}^{+\infty}\int_{-\infty}^{+\infty}\int_{-\infty}^{+\infty} g(\nu,\tau)\mathbf{x}(u+\tau/2)\mathbf{x}^H(u-\tau/2)e^{j2\pi(\nu t-\nu u-f\tau)}d\nu du d\tau \tag{3.1}$$

Where $g(\nu,\tau)$ is the Doppler-lag kernel function (see chapter 2).

The cross-term STFD matrix between two vector signals $\mathbf{x}_1$ and $\mathbf{x}_2$ is defined as

$$\mathbf{D_{x_1x_2}}(t,f) = \int_{-\infty}^{+\infty}\int_{-\infty}^{+\infty}\int_{-\infty}^{+\infty} g(\nu,\tau)\mathbf{x}_1(u+\tau/2){\mathbf{x}_2}^H(u-\tau/2)e^{j2\pi(\nu t-\nu u-f\tau)}d\nu du d\tau \tag{3.2}$$

The discrete form of the spatial pseudo Wigner-Ville distribution (SPWVD) matrix, using a rectangular window of length L_h, is obtained by replacing the signal $z(t)$ in Eq. 2.29 by the signal vector $\mathbf{x}(t)$

$$\mathbf{D_{xx}}(t,f) = \sum_{\tau=-\frac{L_h-1}{2}}^{\frac{L_h-1}{2}} \mathbf{x}(t+\tau)\mathbf{x}^H(t-\tau)e^{-j4\pi f\tau} \tag{3.3}$$

3.3 Time-frequency subspace based methods

In narrowband array processing, where L signals arrive at a M-element array (see Fig. 1.1). The linear data model given by Eq. 1.23 as

$$\mathbf{x}(t) = \mathbf{y}(t) + \mathbf{n}(t) = \mathbf{A}\mathbf{s}(t) + \mathbf{n}(t) \tag{3.4}$$

is commonly assumed.

Substituting Eq. 3.4 into Eq. 3.2, we obtain

$$\mathbf{D_{xx}}(t,f) = \mathbf{D_{yy}}(t,f) + \mathbf{D_{yn}}(t,f) + \mathbf{D_{ny}}(t,f) + \mathbf{D_{nn}}(t,f) \tag{3.5}$$

Under the uncorrelated signal and noise assumption and the zero-mean noise property, the expectation

of the cross-term STFD matrices between the signal and the noise vectors is zero, i.e. $E\{\mathbf{D_{yn}}(t,f)\} = E\{\mathbf{D_{ny}}(t,f)\} = 0$, and it follows

$$\tilde{\mathbf{D}}_{\mathbf{xx}}(t,f) = \mathbf{A}\tilde{\mathbf{D}}_{\mathbf{ss}}(t,f)\mathbf{A}^H + \sigma^2\mathbf{I}_M \tag{3.6}$$

where

$$\tilde{\mathbf{D}}_{\mathbf{xx}}(t,f) = E\{\mathbf{D_{xx}}(t,f)\} \tag{3.7}$$

$$\tilde{\mathbf{D}}_{\mathbf{ss}}(t,f) = E\{\mathbf{D_{ss}}(t,f)\} \tag{3.8}$$

$$\sigma_n^2\mathbf{I}_M = E\{\mathbf{D_{nn}}(t,f)\} \tag{3.9}$$

Eq. 3.6 is similar to that which has been commonly used in array processing based on second-order statistics, relating the signal correlation matrix to the data spatial correlation matrix (see Eq. 1.40). This implies that the key problems in various applications of array processing, specifically those dealing with nonstationary signals, can be approached using quadratic time-frequency transformations. If $\tilde{\mathbf{D}}_{\mathbf{ss}}(t,f)$ is full-rank matrix, the two subspaces spanned by the principal eigenvectors of $\tilde{\mathbf{D}}_{\mathbf{xx}}(t,f)$ and the columns of $\mathbf{A}$ become identical. In this case, direction finding techniques based on eigenstructure, described in Section 1.4.2, can be applied.

Eq. 3.6 holds true for every (t,f) point. In order to reduce the effect of noise and ensure the full column rank property of STFD matrix, we consider multiple (t,f) points. This allows more information of the source signal time-frequency signatures to be included into their respective subspace formulation. This is similar to incorporating several snapshots in conventional array processing to perform DOAs estimation and source separation. Joint block-diagonalisation (JBD) [9] and time-frequency averaging (TFA) [31] are the two main approaches that have been used for this purpose.

In practical situations, the sample STFD matrices (Eq. 3.1) are used instead of the exact (statistically expected) matrices (Eq. 3.6).

When only L_0 source signals are selected out of the total of L signal based on their time-frequency signatures, Eq. 3.6 takes the form

$$\tilde{\mathbf{D}}_{\mathbf{xx}}(t,f) = \mathbf{A}^0\tilde{\mathbf{D}}^{\mathbf{0}}_{\mathbf{ss}}(t,f){\mathbf{A}^0}^H + \sigma_n^2\mathbf{I}_M \tag{3.10}$$

Where $\mathbf{A}^0$ and $\mathbf{D^0}_{\mathbf{ss}}(t,f)$, respectively, denote the mixing matrix and the source signal STFD matrix defined using the selected L_0 signals.

This suggests that the well known condition $M > L$ on DOA estimation can be relaxed to $M > L_0$.

i.e. we can perform DOAs estimation with the number of sensors smaller than the number of signals (under-determined system).

3.3.1 Joint block-diagonalisation

If we perform the singular value decomposition (SVD) on the steering matrix $\mathbf{A}(\theta)$, we obtain

$$\mathbf{A}(\theta) = [\mathbf{E}_s \quad \mathbf{E}_n][\mathbf{\Sigma} \quad \mathbf{0}]^T \mathbf{V}^H \tag{3.11}$$

Incorporating the above equation in Eq. 3.6 and assuming the noise-free model, it is easily shown that

$$\mathbf{D_{xx}}(t,f) = [\mathbf{E}_s \quad \mathbf{E}_n]\mathbf{B}(t,f)[\mathbf{E}_s \quad \mathbf{E}_n]^H \tag{3.12}$$

Where $\mathbf{B}(t,f)$ is a block-diagonal matrix given by

$$\mathbf{B}(t,f) = diag[\mathbf{\Sigma V}^H \mathbf{D_{ss}}(t,f)\mathbf{V\Sigma} \quad \mathbf{0}] \tag{3.13}$$

If we consider a set of K matrices, $\mathbf{D_{xx}}(t_k,f_k) \in \mathbb{C}^{M\times M}$, $k = 1,...,K$, we have the following decomposition: for $k = 1,...,K$

$$\mathbf{D_{xx}}(t_k,f_k) = [\mathbf{E}_s \quad \mathbf{E}_n] \begin{bmatrix} \mathbf{A}_k & \mathbf{0} \\ \mathbf{0} & \mathbf{0} \end{bmatrix} \begin{bmatrix} \mathbf{E}_s^H \\ \mathbf{E}_n^H \end{bmatrix} = \mathbf{E}_s \mathbf{A}_k \mathbf{E}_s^H \tag{3.14}$$

Where $\mathbf{E} = [\mathbf{E}_s \quad \mathbf{E}_n]$ is unitary and $\mathbf{A}_k = \mathbf{\Sigma V}^H \mathbf{D_{ss}}(t_k,f_k)\mathbf{V\Sigma}$ are $L \times L$ matrices.

The matrices $\mathbf{D_{xx}}(t_k,f_k)$ are said to be jointly block diagonalisable under the unitary transform $\mathbf{E}$, i.e. $\mathbf{E}^H\mathbf{D_{xx}}(t_k,f_k)\mathbf{E}$ are block diagonal matrices for $k = 1,...,K$.

The problem of JBD consists of estimating the matrices $\mathbf{E}$ (or $\mathbf{E}_s$) and $\mathbf{A}_k, k = 1,..,K$ given the matrices $\mathbf{D_{xx}}(t_k,f_k)$, $k = 1,..,K$.

In practice, the matrices $\mathbf{D_{xx}}(t_k,f_k), k = 1,..,K$ are only approximately block diagonalisable because of noise and finite sample size effects.

A least-square fitting approach for computing the JBD, proposed in [5], consists of finding the $M \times L$ unitary matrix $\mathbf{E}_s$ and the $L \times L$ matrices $\mathbf{A}_k, k = 1,..,K$ that minimise the Frobenius norm of the difference between the STFD matrices $\mathbf{D_{xx}}(t_k,f_k), k = 1,..,K$ and $\mathbf{E}_s\mathbf{A}_i\mathbf{E}_s^H, k = 1,..,K$.

$$\min_{\mathbf{E}_s,\{\mathbf{A}_k\}} \sum_{k=1}^{K} \|\mathbf{D_{xx}}(t_k,f_k) - \mathbf{E}_s\mathbf{A}_k\mathbf{E}_s^H\|^2 \tag{3.15}$$

It has been shown that the LS criterion of Eq. 3.15 is equivalent to the maximisation of the following criterion

$$\max_{\mathbf{E}_s} \sum_{k=1}^{K} \|\mathbf{E}_s^H \mathbf{D}_{\mathbf{xx}}(t_k, f_k)\mathbf{E}_s\|^2 \tag{3.16}$$

3.3.1.1 JBD algorithms

To maximise the JBD criterion of Eq. 3.16, the unitary matrix $\mathbf{E}$ is computed as a product of elementary Givens rotations in [5]. The advantage of the Jacobi methods is their efficient implementation thanks to their inherent parallelism. In addition, the Jacobi methods have a favorable rounding error properties. i.e. small relative perturbation in the matrices entries cause small perturbations on the entries of their eigenstructures.

3.3.1.1.1 Givens rotations

In Jacobi-like algorithms, a unitary matrix $\mathbf{U}$ is decomposed into a product of Given rotations.

$$\mathbf{U} = \prod_{\texttt{\# of sweeps}} \prod_{1 \le p < q \le M} \mathbf{\Theta}_{(qp)} \tag{3.17}$$

Where the elementary Givens rotations are defined as unitary matrices where all diagonal elements are 1 except for the two elements equal to c in rows (columns) p and q. Also, all the off-diagonal elements of $\mathbf{\Theta}_{(qp)}$ are 0 except for the two elements s and $-s^*$ at (p, q) and (q, p) respectively. The scalars c and s are given by

$$\begin{cases} c = \cos(\gamma) \\ s = \sin(\gamma)\exp(i\alpha) \end{cases} \tag{3.18}$$

A procedure to choose the rotation angles γ and α at particular iteration such as the cost function Eq. 3.16 is increased to its maximum is described in the following.

In the sequel, we use $\mathbf{D}_k$ to denote $\mathbf{D}_{\mathbf{xx}}(t_k, f_k)$. For any matrix $\mathbf{D}_k \in \mathbb{C}^{M \times M}$, we define the following orthogonal transformation

$$\mathbf{D}_k^{'} = \mathbf{\Theta}_{(qp)}^H \mathbf{D}_k \mathbf{\Theta}_{(qp)} \tag{3.19}$$

These orthogonal transformations change only the pth and qth rows and the pth and qth columns of $\mathbf{D}_k$. For $q > p > L$ and for $p < q < L$, the Frobenius norm of the top left $L \times L$ submatrix of $\mathbf{D}_k^{'}$ (the value of the JBD criterion Eq. 3.16) is unchanged. So, only the indices (p, q) in the range $1 \le p \le L < q \le M$ are considered. The changed elements of $\mathbf{D}_k^{'}$ in its top left $L \times L$ submatrix are given by:

$$\mathbf{D}_k^{'}(p,j) = c\mathbf{D}_k(p,j) - s\mathbf{D}_k(q,j), |j| \leq L, j \neq p$$
$$\mathbf{D}_k^{'}(j,p) = c\mathbf{D}_k(j,p) - s^*\mathbf{D}_k(j,q), |j| \leq L, j \neq p$$
$$\mathbf{D}_k^{'}(p,p) = \mathbf{D}_k(p,p)c^2 + \mathbf{D}_k(q,q)|s|^2 + \mathbf{D}_k(p,q)s^*c + \mathbf{D}_k(q,p)sc \tag{3.20}$$

3.3.1.1.2 Exact JBD algorithm

The method proposed in [5] consists of maximising iteratively the JBD criterion Eq. 3.16 using Givens rotations. The algorithm starts from $\mathbf{E} = \mathbf{I}$. When the iterative procedure ends, we obtain $\mathbf{E}$ as

$$\mathbf{E} = \prod_{\texttt{\# of iterations}} \prod_{1 \leq p < q \leq M} \mathbf{\Theta}_{(qp)} \tag{3.21}$$

Where the matrices $\mathbf{\Theta}_{(qp)}$ are computed such as 3.16 is maximum. Thus, at each iteration the angles (γ, α) are determined by maximising the following cost function:

$$(\gamma, \alpha) = \arg\max \mathcal{C}(\gamma, \alpha) \tag{3.22}$$

where

$$\mathcal{C}(\gamma, \alpha) = \sum_{k=1}^{K} \sum_{i,j}^{L} |\mathbf{D}_k^{'}(i,j)|^2 \tag{3.23}$$

Therefore, the exact JBD algorithm can be summarised as follows

$\mathbf{E} = \mathbf{I}$

`For n=1,...,# of iterations`

`For` $1 \leq p \leq L < q \leq M$

$\mathbf{\Theta}_{(qp)} = \arg\max_{\gamma,\alpha} \mathcal{C}(\gamma, \alpha)$

$\mathbf{E} = \mathbf{E}\mathbf{\Theta}_{(qp)}$ `and` $\mathbf{D}_k = \mathbf{\Theta}_{(qp)}^H \mathbf{D}_k \mathbf{\Theta}_{(qp)}, k = 1, ..., K$

The maximisation of $\mathcal{C}(\theta, \alpha)$ is equivalent to the maximisation of the quadratic form

$$\max_{\|\mathbf{v}\|=1} = (\mathbf{v}^T\mathbf{G}\mathbf{v} + \mathbf{g}^T\mathbf{v}) \tag{3.24}$$

Where $\mathbf{v} = [\cos(2\gamma), \sin(2\gamma)\cos(\alpha), \sin(2\gamma)\sin(\alpha)]^T$, $\mathbf{G}$ is a 3×3 matrix and $\mathbf{g}$ is a 3×1 vector. The expressions of $\mathbf{g}$ and $\mathbf{G}$ are given in the appendix. The maximisation of Eq. 3.24 leads to

$$\mathbf{v} = -\frac{1}{2}(\mathbf{G} + \lambda\mathbf{I})^{-1}\mathbf{g} \tag{3.25}$$

Where λ is a scalar chosen such as

$$\|\mathbf{v}\|^2 = 1 \Longleftrightarrow \frac{1}{4}\sum_{i=1}^{3}\frac{|\mathbf{u}_i^T\mathbf{g}|^2}{(\lambda_i+\lambda)^2} = 1 \tag{3.26}$$

Where $\mathbf{u}_i$ and $\lambda_i, i = 1,2,3$ are the eigenvectors and eigenvalues of $\mathbf{G}$.

From Eq. 3.26 we can see that finding λ involves the rooting of a $6th$ order polynomial. Amongst all the roots of the polynomial, we select the one which makes the vector $\mathbf{v}$ maximises the value of $\mathcal{C}(\gamma,\alpha)$, i.e. the vector $\mathbf{v}$ that maximises Eq. 3.24.

It has been observed in [5] that when the matrices are almost jointly diagonalisable, Eq. 3.25 is numerically unstable. In this case an alternative method is to use the following expression

$$\mathbf{v} = -\frac{1}{2}(\mathbf{G} - \lambda_i\mathbf{I})^{\dagger}\mathbf{g} + c_i\mathbf{u}_i, i = 1,2,3 \tag{3.27}$$

The real scalar c_i is chosen such that Eq. 3.24 is verified. It is given by

$$c_i = sign(\mathbf{u}_i^T\mathbf{g})(1 - \|(\mathbf{G} - \lambda_i\mathbf{I})^{\dagger}\mathbf{g}\|^2/4)^{\frac{1}{2}}$$

3.3.1.1.3 Approximate JBD algorithm

In the approximate JBD algorithm, $|\mathbf{D}_k^{'}(p,p)|^2$ is approximated by $|\mathbf{D}_k^{'}(p,p)|^2 \approx |[\mathbf{D}_k\mathbf{\Theta}_{(qp)}](p,p)|^2 + |[\mathbf{\Theta}_{(qp)}^H\mathbf{D}_k](p,p)|^2$. Using this approximation, the JBD criterion takes the following simpler form

$$\mathcal{C}(\gamma,\alpha) \approx \tilde{\mathbf{g}}^T\mathbf{v} \tag{3.28}$$

The maximisation of Eq. 3.28 leads to the following expressions

$$\alpha = \arctan(\frac{\Im(a)}{\Re(a)}) \tag{3.29}$$

$$\gamma = \frac{1}{2}\arctan(-2\frac{\Re(e^{-i\alpha}a)}{b}) \tag{3.30}$$

$$a = \sum_{k=1}^{K}\sum_{j=1}^{L}\mathbf{D}_k(p,j)\mathbf{D}_k^*(q,j) + \mathbf{D}_k(j,p)\mathbf{D}_k^*(j,q) \tag{3.31}$$

$$b = \sum_{k=1}^{K}\sum_{j=1}^{L}|\mathbf{D}_k(p,j)|^2 + |\mathbf{D}_k(j,p)|^2 - (|\mathbf{D}_k(q,j)|^2 + |\mathbf{D}_k(j,q)|^2) \tag{3.32}$$

The expression of $\tilde{\mathbf{g}}$ as well as the detailed calculation are given in the appendix.

3.3.2 Time-frequency MUSIC

We give the algorithm involved in the implementation of TF-MUSIC to show how the time-frequency subspace based algorithms can be implemented using the STFD matrices and the subspace based algorithms described in Section 1.4.2 (different versions of MUSIC, ESPRIT and Min-Norm).

The time-frequency spectral and root-MUSIC algorithms are summarised in the following steps:

- STEP 1: Form the K matrices $\mathbf{D_{xx}}(t_k, f_k)$ for the selected (t_k, f_k) points, $k = 1, 2, ..., K$
- STEP 2: The eigenvectors of $E\{\mathbf{D_{xx}}(t_k, f_k)\}$ corresponding to the $M - L$ smallest eigenvalues, which form the noise subspace $\mathbf{E}_n = [\mathbf{e}_{L+1}, \mathbf{e}_{L+2}, ..., \mathbf{e}_M]$, are obtained by JBD of the STFDs, or TFA through the eigendecomposition of averaged matrix

$$\hat{\mathbf{D}}_{\mathbf{xx}} = \frac{1}{K} \sum_{k=1}^{K} \mathbf{D_{xx}}(t_k, f_k) \tag{3.33}$$

- STEP 3: Estimate the DOAs from the peaks of the TF spectrum defined by Eq. 1.44 to obtain the time-frequency spectral MUSIC (**TF spectral MUSIC**) estimator, or by solving the polynomial defined by Eq. 1.49 to obtain the time-frequency root MUSIC (**TF-root-MUSIC**).

Fig. 3.1 shows the estimated spatial spectra at $SNR = -20dB$ based on the conventional spectral MUSIC and TF spectral MUSIC. The array antenna has eight sensors separated by half a wavelength. The number of sample is N=1024. Two chirp signals emitted from two sources positioned at $(\theta_1, \theta_2) = (-10^o, 10^o)$. The start and end frequencies of the two chirps are : $(w_{1s}, w_{1e}) = (0, \pi)$ rad and $(w_{2s}, w_{2e}) = (\pi, 0)$ rad. PWVD with a Hamming window of length $L_h = 129$ is considered. TFA of $N - L_h + 1 = 896$ (t,f) points of each source signature is used. The time-frequency MUSIC clearly resolves the spectral peaks whereas the conventional MUSIC does not.

3.3.3 Time-frequency Min-Norm

The steps involved in the implementation of time-frequency spectral and root-Min-Norm are:

- STEP 1: Same as for TF-MUSIC
- STEP 2: Same as for TF-MUSIC
- STEP 3: Partition the noise subspace $\hat{\mathbf{E}}_n$ using Eq. 1.51 and express the prediction vector $\mathbf{b}$ using Eq. 1.52
- STEP 4: Find the L largest peaks over θ of the spatial spectrum defined by Eq. 1.53 to obtain the time-frequency spectral Min-Norm (**TF spectral Min-Norm**) estimator, or by solving the

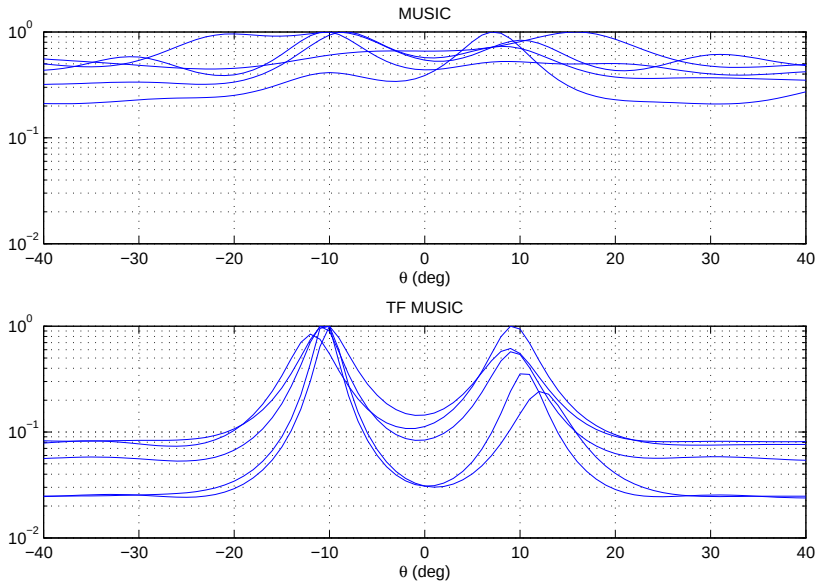

Figure 3.1: The estimated spatial spectra of conventional MUSIC and TF MUSIC

polynomial defined by Eq. 1.55 to obtain the time-frequency root Min-Norm estimator (**TF-root-Min-Norm**).

Fig 3.2 shows the estimated spatial spectra based on the conventional spectral Min-Norm and TF spectral Min-Norm. The values of parameters are the same as those used to plot Fig. 3.1. It is clear that the TF spectral Min-Norm peaks are clearly resolved.

3.3.4 Time-frequency ESPRIT

We can also formulate the time-frequency LS-ESPRIT and TLS-ESPRIT algorithms as follows:

- STEP 1: Same as for TF-MUSIC
- STEP 2: Same as for TF-MUSIC
- STEP 3: Form $\hat{\mathbf{E}}_{1s}$ and $\hat{\mathbf{E}}_{2s}$ using Eq. 1.64
- STEP 4: Solve Eq. 1.59 in either a Least-Square sense to obtain the time-frequency LS-ESPRIT (**TF-LS-ESPRIT**) estimator, or a Total-Least-Square sense to obtain the time-frequency TLS-ESPRIT (**TF-TLS-ESPRIT**) estimator
- STEP 5: The DOAs estimates are obtained by applying the formula 1.63 to the eigenvalues of $\hat{\Psi}\,, (\lambda_{\psi k}, k = 1, 2, ..., L)\,.$

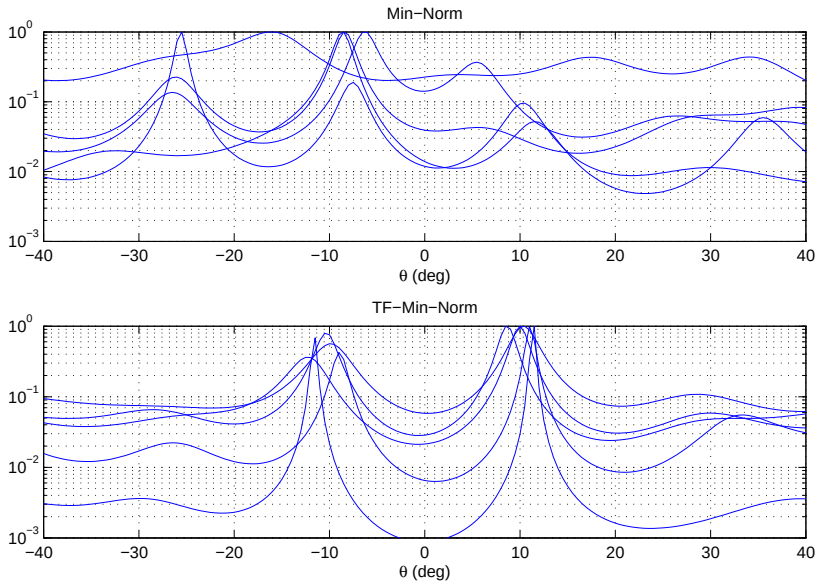

Figure 3.2: The estimated spatial spectra of conventional Min-Norm and TF-Min-Norm

3.4 Time-frequency maximum likelihood

Compared to the time-frequency subspace based methods, time-frequency maximum likelihood method can be applied to coherent environments, without the need to perform any type of preprocessing , such us spatial smoothing.

The conventional ML estimator is obtained by solving the minimisation problem defined by Eq. 1.84 whereas the time-frequency ML is obtained by solving the minimisation problem defined by Eq. 3.34.

$$\hat{\theta}^{tf} = \arg\min_{\theta}\{Tr\{\Pi_{\mathbf{A}}^{\perp}\hat{\mathbf{D}}_{\mathbf{xx}}\}\} \tag{3.34}$$

Eq. 3.34, defined from the STFD matrix, is similar to Eq. 1.84 and is obtained by replacing $\hat{\mathbf{R}}_{\mathbf{xx}}$ by $\hat{\mathbf{D}}_{\mathbf{xx}}$ [32].

We can now summarise the time-frequency maximum likelihood (**TF-ML**) algorithm in the following steps:

- STEP 1: Form the K matrices $\mathbf{D}_{\mathbf{xx}}(t_k, f_k)$ for the selected (t_k, f_k) points, $k = 1, 2, ..., K$
- STEP 2: Calculate $\hat{\mathbf{D}}_{\mathbf{xx}}$ using Eq. 3.33
- STEP 3: Solve Eq. 3.34 to obtain the DOAs.

To demonstrate the advantage of TF-ML over the conventional ML, we consider a uniform linear array of eight sensors separated by half a wavelength. The number of sample is $N = 1024$. Two chirp

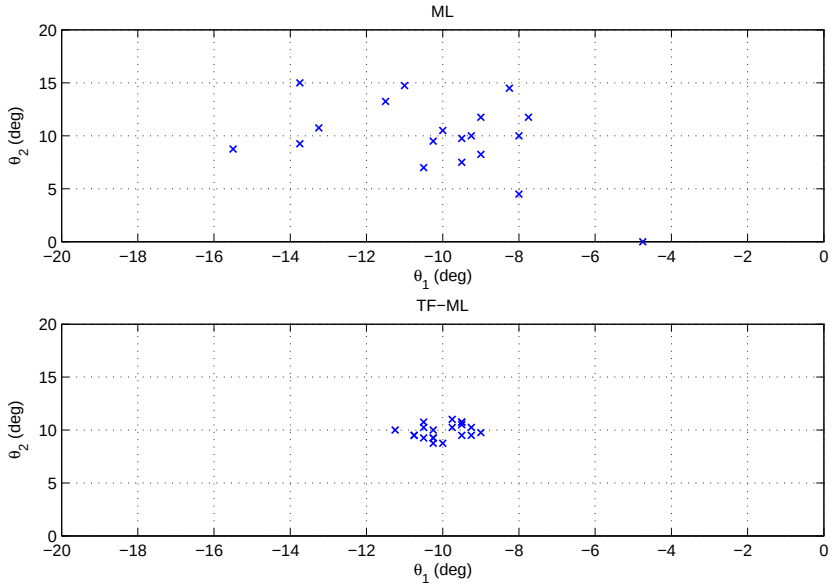

Figure 3.3: (θ_1, θ_2) which maximise the TF-ML and conventional ML functions

signals emitted from two sources positioned at $(\theta_1, \theta_2) = (-10^o, 10^o)$. The start and end frequencies of the two chirps are $:(w_{1s}, w_{1e}) = (0.2\pi, \pi)$ rad and $(w_{2s}, w_{2e}) = (0, 0.8\pi)$ rad. The SNR of each source signal is $-20dB$. PWVD with a Hamming window of length $L_h = 129$ is considered. PWVD with a window length $L_h = 129$ is considered. TFA of $N - L_h + 1 = 896$ (t, f) points of each source signature is used.

Fig. 3.3 shows (θ_1, θ_2) that yield the maximum values of the likelihood function of TF-ML and the conventional ML methods for 20 independent trials. It is evident that TF-ML provides much more improved DOA estimation over the conventional ML.

In the next example, we compare the TF-ML and the TF-MUSIC for coherent sources. The two coherent chirp signals have the same start and end frequencies $(w_{1s}, w_{1e}) = (w_{2s}, w_{2e}) = (0, \pi)$ rad, with $\pi/2$ phase difference. The signals arrive at $(\theta_1, \theta_2) = (-2^o, 2^o)$. The SNR of both signals is $5dB$ and the number of snapshots $N = 1024$. Again, we used $L_h = 129$ for both TF-ML and TF-MUSIC. Fig. 3.4 shows (θ_1, θ_2) which maximise the TF-ML function, and the estimated spectra of TF-MUSIC for five independent trials. It is clear that the TF-ML can separate the two signals whereas the TF-MUSIC cannot.

Like the conventional maximum likelihood method, time-frequency maximum likelihood has also a heavy computational load since the non-linear L-dimensional optimisation problem (Eq. 3.34) must be solved numerically.

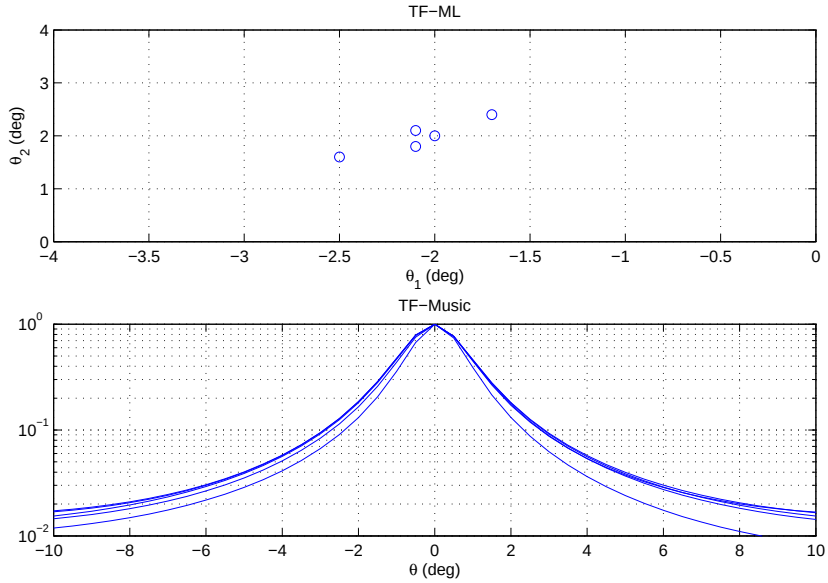

Figure 3.4: TF-ML function and TF-MUSIC spectra of two coherent chirp signals

3.5 Time-frequency subspace fitting

The traditional correlation matrix $\hat{\mathbf{R}}_{\mathbf{xx}}$ can be replaced by the STFD averaged matrix $\hat{\mathbf{D}}_{\mathbf{xx}}$ [19], and after eigendecomposition of $\hat{\mathbf{D}}_{\mathbf{xx}}$, the DOAs of signals can be estimated with subspace fitting as the traditional method does (see section 1.4.4).

Now we can formulate the algorithm of time-frequency subspace fitting methods as:

- STEP 1: Form K matrices $\mathbf{D}_{\mathbf{xx}}(t_k, f_k)$ for the selected (t_k, f_k) points, $k = 1, 2, ..., K$
- STEP 2: Calculate $\hat{\mathbf{D}}_{\mathbf{xx}}$ using Eq. 3.33
- STEP 3: Eigendecompose $\hat{\mathbf{D}}_{\mathbf{xx}}$ to obtain $\hat{\mathbf{E}}_s$ which spans the signal subspace, or $\hat{\mathbf{E}}_n$ which spans the noise subspace. The JBD can also be used to obtain $\hat{\mathbf{E}}_s$ and $\hat{\mathbf{E}}_n$
- STEP 4: Solve Eq. 1.97 to obtain the time-frequency signal subspace fitting (**TF-SSF**) estimator, Eq. 1.101 to obtain the time-frequency weighted subspace fitting (**TF-WSF**) estimator, or Eq. 1.102 to obtain the time-frequency noise subspace fitting (**TF-NSF**) estimator.

Fig. 3.5 shows (θ_1, θ_2) that yield the minimum values of the TF-WSF and the conventional WSF functions for 20 independent trials, where the values of the parameters are the same as those used to plot Fig. 3.3. Again, It is clear that TF-WSF provides much more improved DOAs estimation over the

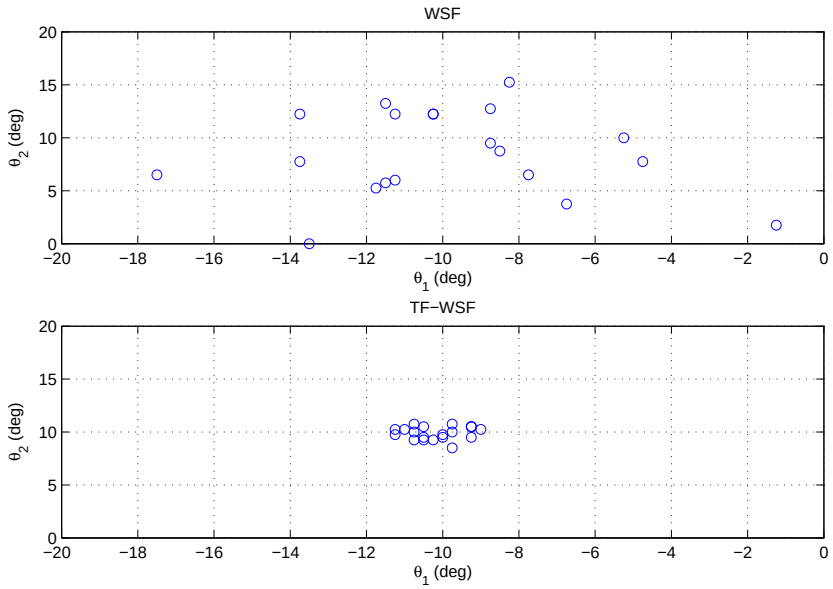

Figure 3.5: (θ_1, θ_2) which minimise the TF-WSF and conventional WSF functions

conventional WSF.

As the conventional method, the time-frequency subspace fitting methods still have a heavy computational load.

3.6 Selection of auto- and cross-terms in the time-frequency domain

Up to now, we have assumed that the signatures of signals are known. However in blind scenario, no *a priori* knowledge of the source time-frequency localisation can be assumed and must therefore be estimated. In this section, we describe the existing methods to detect the auto- and cross-terms in the time-frequency domain.

A simple method to select the auto-terms in the time-frequency domain is to consider the (t, f) with the maximum energy in the time-frequency plane[8]. However, this method has shown its limitations in the practical situations. A projection-based selection procedure of auto- and cross-terms, which exploits the off-diagonal structure of the cross STFDs, has been proposed in [4]. An alternative solution which consists of exploiting the existence of only one source at some auto-term points has been proposed in [1]. In order to discriminate between noise and either auto- or cross-terms, the variance of a test static was used in [13] where the variance of the test static is estimated using a bootstrap resampling technique. Spatial averaging has been shown to reduce the effect of cross-terms without smearing the auto-terms which allows easier detection of the auto-term points in the time-frequency plane [33]. It has been shown in [17] that when

the imaginary part of the STFD of real valued signals is not equal to zero, the considered (t, f) point is cross-term point. The latter selection criterion of auto- and cross-terms was then extended to the case of noisy signals by introducing two thresholds based on Bayesian and Neyman-Person approaches [16].

3.6.1 Projection-based selection procedure

In [4], a projection-based selection procedure was proposed to distinguish between auto- and cross-terms. This method uses a unitary linear model obtained by pre- and post-multiplying the STFD by the whitening matrix $\mathbf{W}$. This leads to the whitened STFD $\mathbf{D_{zz}}(t, f)$, defined as

$$\mathbf{D_{zz}}(t, f) = \mathbf{W}\mathbf{D_{xx}}(t, f)\mathbf{W}^H \tag{3.35}$$

where $\mathbf{W}$ is a $L \times M$ whitening matrix such as

$$(\mathbf{WA})(\mathbf{WA})^H = \mathbf{U}\mathbf{U}^H = \mathbf{I}_L \tag{3.36}$$

The whitening matrix can be calculated by different methods. For example, it can be calculated as an inverse square root of the observation covariance matrix [10] or obtained from the STFD as shown in [30].

From Eqs. 3.6, 3.35 and 3.36, we obtain in the noise-free case the following linear unitary model

$$\mathbf{D_{zz}}(t, f) = \mathbf{U}\mathbf{D_{ss}}(t, f)\mathbf{U}^H \tag{3.37}$$

Auto-source STFD: we define the auto-source STFD by

$$\mathbf{D^a_{ss}}(t, f) = \mathbf{D_{ss}}(t, f) \quad \text{for auto-term TF points } (t_a, f_a) \tag{3.38}$$

Cross-source STFD: we define the cross-source STFD by

$$\mathbf{D^c_{ss}}(t, f) = \mathbf{D_{ss}}(t, f) \quad \text{for cross-term TF points } (t_c, f_c) \tag{3.39}$$

The cross-source STFD matrix $\mathbf{D^c_{ss}}(t, f)$ is quasi anti-diagonal for each TF point that corresponds to cross-term because the diagonal elements are the auto-terms. Based on this observation a selection approach that exploits the anti-diagonal structure of cross-source STFD matrices was defined. More precisely, we have

$$\begin{aligned} Trace(\mathbf{D^c_{zz}}(t, f)) &= Trace(\mathbf{U}\mathbf{D^c_{ss}}(t, f)\mathbf{U}^H) \\ &= Trace(\mathbf{D^c_{ss}}(t, f)) \approx 0 \end{aligned} \tag{3.40}$$

From Eq. 3.40, the following testing procedure can be defined

$$\text{if } \frac{Trace(\mathbf{D_{zz}}(t,f))}{norm(\mathbf{D_{zz}}(t,f))} < \epsilon \rightarrow \text{decide that } (t,f) \text{ is a cross-term} \tag{3.41}$$

$$\text{if } \frac{Trace(\mathbf{D_{zz}}(t,f))}{norm(\mathbf{D_{zz}}(t,f))} > \epsilon \rightarrow \text{decide that } (t,f) \text{ is an auto-term} \tag{3.42}$$

where ϵ is a small positive real scalar (typically $\epsilon = 0.9$).

Selection algorithm: a DOA estimation method based on this selection procedure can be summarised in the following steps:

- STEP 1: Estimate the auto-correlation matrix $\hat{\mathbf{R}}_{\mathbf{xx}}$ from N data sample. Denote by $\lambda_1, \lambda_2, ..., \lambda_L$ the L largest eigenvalues and by $\mathbf{e}_1, \mathbf{e}_1, ..., \mathbf{e}_L$ the corresponding eigenvectors of $\hat{\mathbf{R}}_{\mathbf{xx}}$.
- STEP 2: An estimate $\hat{\sigma}_n^2$ of the noise variance is the average of the $M - L$ smallest eigenvalues of $\hat{\mathbf{R}}_{\mathbf{xx}}$. The whitening matrix is formed as

$$\hat{\mathbf{W}} = [(\lambda_1 - \hat{\sigma}_n^2)^{\frac{-1}{2}}\mathbf{e}_1, (\lambda_2 - \hat{\sigma}_n^2)^{\frac{-1}{2}}\mathbf{e}_2, ..., (\lambda_L - \hat{\sigma}_n^2)^{\frac{-1}{2}}\mathbf{e}_L]^H$$

- STEP 3: Compute the whitened STFD matrix $\mathbf{D_{zz}}(t,f)$ using Eq. 3.35.
- STEP 4: Select a set of TF points (corresponding to the high amplitude points of the signal TF transform) and then distinguish between auto- and cross-terms points using the selection criterion defined by Eqs. 3.41 and 3.42
- STEP 5: Use TFA or JBD to incorporate the selected auto- or cross-terms in the chosen time-frequency DOAs estimation method.

In contrast to the method proposed in [8], this approach distinguishes between auto- and cross-terms. However, this method does not differentiate between the auto-terms belonging to different sources. Furthermore, it does not clearly address the problem of discriminating between noise and the true power concentration.

3.6.2 DOAs estimation using vector clustering

This method was initially proposed to deal with the problem of underdetermined blind separation of nonstationary sources [1]. Herein, we adapt this method to the DOAs estimation problem.

In this approach, the sources are assumed to be orthogonal in the TF domain in the sense that their TF supports are disjoint. However, simulation results in [1] and [23] have shown that the orthogonality condition can be relaxed as almost orthogonal.

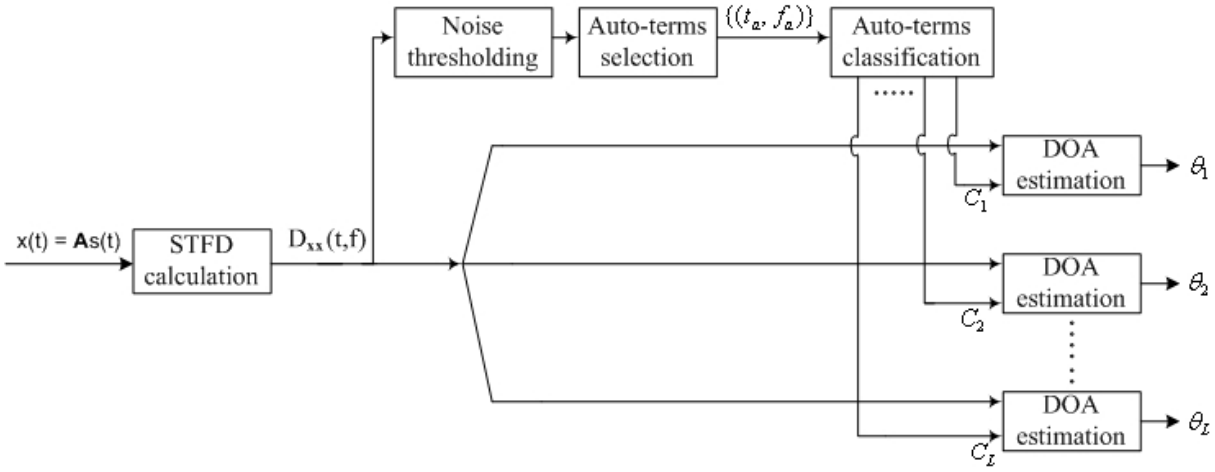

Figure 3.6: Block diagram of the proposed algorithm

Under the orthogonality assumption, two auto-term points (t_1, f_1) and (t_2, f_2) corresponding to the same source $s_i(t)$ are in the noise-free case such that:

$$\mathbf{D_{xx}}(t_1, f_1) = D_{s_i s_i}(t_1, f_1)\mathbf{a}_i\mathbf{a}_i^H \tag{3.43}$$

$$\mathbf{D_{xx}}(t_2, f_2) = D_{s_i s_i}(t_2, f_2)\mathbf{a}_i\mathbf{a}_i^H \tag{3.44}$$

Eq. 3.43 and 3.44 indicate that $\mathbf{D_{xx}}(t_1, f_1)$ and $\mathbf{D_{xx}}(t_2, f_2)$ have the same principal eigenvector $\mathbf{a}_i$. The main idea of the this algorithm is to group together the auto-term points associated with the same principal eigenvector. The DOAs are then obtained using the auto-term points of the selected signal. The block diagram of the proposed algorithm is shown in Fig. 3.6. This algorithm can be summarised in four steps as follows:

- STEP 1: ***STFD computation and noise thresholding***: the STFD matrices $\mathbf{D_{xx}}(t, f)$ are computed and then a noise thresholding ϵ_1 is applied to the signal TFD to keep only the (t_s, f_s) with suffient energy in order to reduce the computational complexity.

$$\text{keep} \quad (t_s, f_s) \quad \text{if} \quad \|\mathbf{D_{xx}}(t_s, f_s)\| > \epsilon_1. \tag{3.45}$$

  where ϵ_1 is a small positive scalar typically $\epsilon_1 = 0.05$ of the TF point with maximum energy.

- STEP 2: ***Auto-terms selection***: in this step, the auto-term points are separated from the cross-term points using an appropriate testing criteria. In the case of TF orthogonality, each auto-term STFD matrix is of rank one or has one large eigenvalue compared to its other eigenvalues. Based upon this observation, rank selection criteria such as MDL (minimum description length) or AIC

(Aikaike information criterion) can be used to select auto-term points as those corresponding to the STFD matrices of rank equal to one. The following simple criterion was used in [1]

$$\text{if} \quad \left| \frac{\lambda_{max}\{\mathbf{D_{xx}}(t,f)\}}{norm\{\mathbf{D_{xx}}(t,f)\}} - 1 \right| > \epsilon_2 \rightarrow \quad \text{decide that } (t,f) \text{ point is a cross-term point} \tag{3.46}$$

where ϵ_2 is a small positive scalar (typically $\epsilon_2 = 10^{-4}$), and $\lambda_{max}\{\mathbf{D_{xx}}(t,f)\}$ represents the largest eigenvalue of $\mathbf{D_{xx}}(t,f)$.

- STEP 3: ***Vector clustering***: the clustering is based upon the fact that two STFD matrices corresponding to the same source signal have the same principal eigenvector. The clustering is implemented by the following operations:

  (a) Compute for each auto-term point (t_a, f_a) the main eigenvector, $\mathbf{a}(t_a, f_a)$, of the auto-term STFD matrix $\mathbf{D_{xx}}(t_a, f_a)$

  (b) Since the vectors $\mathbf{a}(t_a, f_a)$ are estimated up to a random phase $e^{j\phi}$, $\phi \in [0, 2\pi)$, we force their first entries to one.

  (c) The obtained vectors are then clustered to different classes $\{C_i\}$. The number of sources is equal to the number of classes. Two vectors $\mathbf{a}(t_i, f_i)$ and $\mathbf{a}(t_j, f_j)$ belong to the same class if:

  $$d(\mathbf{a}(t_i, f_i), \mathbf{a}(t_j, f_j)) < \epsilon_3 \tag{3.47}$$

  where ϵ_3 is a properly chosen positive scalar and d is a distance measure. For example, we use the angle between the two vectors as a distance measure.

  $$d(\mathbf{a}_i, \mathbf{a}_j) = \arccos(\tilde{\mathbf{a}}_i^T \tilde{\mathbf{a}}_j) \tag{3.48}$$

  where $\tilde{\mathbf{a}} = [\Re(\mathbf{a})^T, \Im(\mathbf{a})^T]^T / \|\mathbf{a}\|$.

- STEP 4: ***DOAs estimation***: Consider the auto-term points belonging to each class, $(t_a, f_a) \in \{C_i\}$, in any time-frequency DOAs estimation algorithm to estimate the DOA of each signal separately.

This method allows the improvement of the DOAs estimation by grouping the time-frequency points belonging to each source separately. This TF grouping becomes essential if the number of sources is greater than the number of sensors used. Like the previous method, this one does not propose an efficient procedure to distinguish between noise the true power concentration.

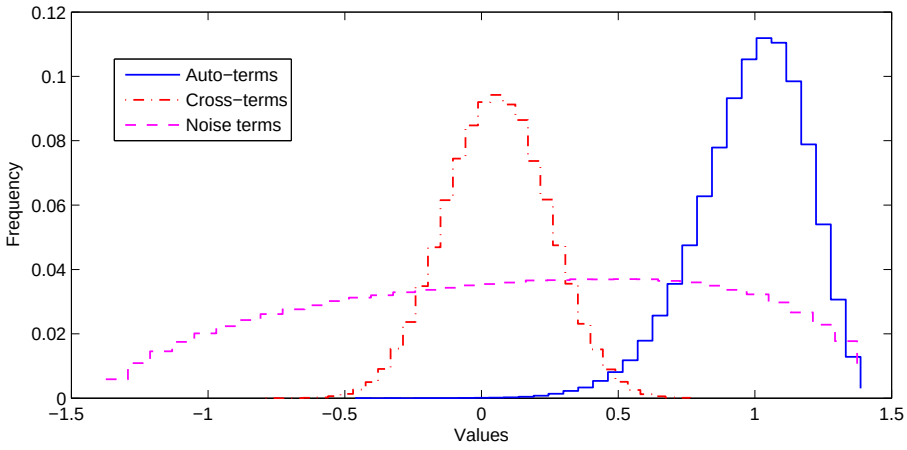

Figure 3.7: Distribution of the Test Statistic

3.6.3 Bootstrap based selection method

A procedure for the classification of noise, auto- and cross-terms was proposed in [13]. This procedure uses an estimate of the variance of the test statistic given in Eqs. 3.41 and 3.42 and defined as

$$T(t,f) = \frac{Trace(\mathbf{D_{zz}}(t,f))}{norm(\mathbf{D_{zz}}(t,f))} \tag{3.49}$$

Where $\mathbf{D_{zz}}(t,f)$ is the whitened STFD.

The test statistic given by 3.49 should be close to one at an auto-term and approximately zero at a cross-term location. In the TF regions where only noise is present, T can still have high values due to significant noise power which may cause false detection of auto- or cross-terms.

In order to obtain an estimate of the distribution of the test statistic at noise, auto- and cross-terms locations, we conduct a Monte-Carlo simulation of 1,000 independent runs at an SNR of $-5dB$ for an ULA of 5 elements receiving two chirp signals at $(-10, 10)$ degrees respectively. Pseudo Wigner-Ville distribution and $N = 256$ snapshots were considered in the simulation. The result shown in Fig. 3.7 clearly reveals that the distribution of the test statistic is centered around zero for noise and cross-terms and at one for auto-terms locations. Furthermore, the density at noise location significantly overlaps that of auto- and cross-term densities.

Fig. 3.7 suggests the use of the variance of the test statistic to discriminate between noise terms and either auto- or cross-terms.

Since only one value of the test statistic is available at any given (t,f) point, the variance can not be estimated directly but it may be estimated using a re-sampling scheme such as the bootstrap as suggested in [13].

After the estimation of the variance of the test statistic, σ_T^2, the procedure illustrated in Fig. 3.8 may

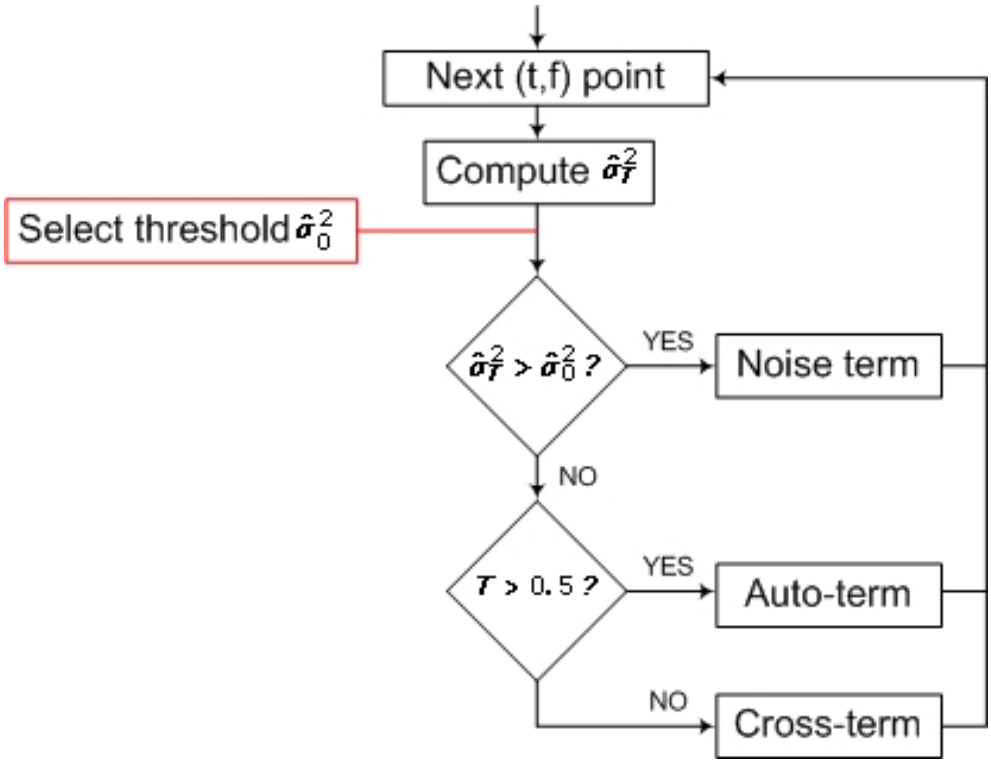

Figure 3.8: Procedure for automatic classification of TF points

be employed to classify automatically the TF points into the three classes.

3.6.3.1 Bootstrap

The bootstrap is a powerful technique for assessing the accuracy of a parameter estimator in situation where the conventional techniques such as large sample methods are not valid. In many signal-processing problems large sample methods cannot be applied either because of time constraints since these methods need large size of sample or because the process is nonstationary and only small portions of data can be considered as stationary.

The bootstrap has been successively used to solve many signal processing that would be too complicated for traditional statistical analysis [34].

With the bootstrap, the observation are randomly reassigned, and the estimate recomputed. The reassignment of the observation and recomputations of estimates are done thousands of time and they are considered as repeated independent experiments. For example, if we want to estimate the variance of a parameter estimator, $\hat{\vartheta}$, from one experiment the following bootstrap procedure can be used:

- STEP 1: ***Experiment***: Conduct the experiment and collect the random data into the sample $x = \{x_1, x_2, ..., x_n\}$.

- STEP 2: ***Resampling***: Using a pseudo-random generator, draw a random sample (*bootstrap resample*) x^*, of size n, with replacement, from x.

- STEP 3: ***Calculating of the bootstrap estimate***: Evaluate the *bootstrap estimate* $\hat{\vartheta}^*$ from x^* calculated in the same manner as $\hat{\vartheta}$ but with the resample x^* replacing x.

- STEP 4: ***Repetition***: Repeat steps 1 and 2 many times to obtain a total of B bootstrap estimates,

$$\hat{\vartheta}_1^*, \hat{\vartheta}_2^*, ..., \hat{\vartheta}_B^*$$

- STEP 4: ***Variance estimation of*** $\hat{\vartheta}$: Estimate the variance, $\hat{\sigma}_{\hat{\vartheta}}^2$ of $\hat{\vartheta}$ by the sample variance of the B bootstrap estimates,

$$\hat{\sigma}_{\hat{\vartheta}}^2 = \frac{1}{B-1} \sum_{b=1}^{B} \left(\hat{\vartheta}_b^* - \frac{1}{B} \sum_{b=1}^{B} \hat{\vartheta}_b^* \right)^2$$

For the problem of estimating the variance of the test T, the bootstrap resampling is used. This involves resampling from independent residuals of the auto-correlation function. The following procedure is used to estimate the variance of the test statistic:

- STEP 1: Compute $D_{z_i z_j}(t, f)$ for $i, j = 1, ..., L$

- STEP 2: Smooth $D_{z_i z_j}(t, f)$ using a 1-D or 2-D filter to obtain $\bar{D}_{z_i z_j}(t, f)$

- STEP 3: Find smoothed local auto-correlation

$$\bar{R}_{z_i z_j}(t, \tau) = \mathcal{FT}^{-1}_{\tau \leftarrow f} \{ \bar{D}_{z_i z_j}(t, f) \}$$

- STEP 4: Bootstrap from residuals

$$E_{z_i z_j}(t, \tau) = R_{z_i z_j}(t, \tau) - \bar{R}_{z_i z_j}(t, \tau)$$

to obtain the bootstrap samples $E^{*b}_{z_i z_j}(t, \tau)$, $b = 1, 2, .., B$.

- STEP 5: Calculate

$$D^{*b}_{z_i z_j}(t, f) = \mathcal{FT}_{\tau \rightarrow f} \{ E^{*b}_{z_i z_j}(t, \tau) + \bar{R}_{z_i z_j}(t, \tau) \}$$

and then form $\mathbf{D}^{*b}_{\mathbf{zz}}(t, f)$, $b = 1, 2, .., B$.

- STEP 6: Calculate the bootstrap estimates $T^{*b}(t, f), b = 1, 2, .., B.$ and then the variance

$$\hat{\sigma}^2_{T^*} = \frac{1}{B-1}\sum_{b=1}^{B}\left(T^{*b} - \frac{1}{B}\sum_{b=1}^{B}T^{*b}\right)^2$$

In the bootstrap resampling, we assume that the random variables are statistically independent and identically distributed. This condition is not usually valid for the data itself. So we try to find "residuals" which satisfy this condition. However, residuals satisfying this condition are not easy to obtain directly from the TFD. By transforming to the correlation domain, residuals were not correlated and therefore better suited for resampling.

An important issue in implementing the automatic point classification procedure illustrated in Fig. 3.8 is the selection of threshold for the variance of the test statistic. Because of the lack of analytical expression of the distribution of the test statistic, we will use a Monte-Carlo estimate of the distribution of the variance of test statistic to set a threshold for classifying noise terms.

3.7 Conclusion

The examples provided reveal that the TF methods outperform the conventional ones. However, a quantified analysis is needed to measure their performance and find out where the application of TF methods is worthwhile.

To reduce the effect of noise and ensure the full column rank property of STFD matrix, multiple TF points have to be considered. We have shown that there are two ways to incorporate multiple TF points in the determination of the noise and signal subspaces, namely time-frequency averaging and joint-block diagonalisation and we gave the algorithms used by each one. The effectiveness of these two methods should also be assessed and compared. Another important aspect which has to be considered is the effects of incorporation of auto- and cross-terms upon the performance of the TFA or JBD procedures.

Finally, we addressed the issue of detecting noise terms, auto- and cross-terms in the TF domain. We also covered the aspect of TF grouping to improve the performance and to deal with the underdetermined problems. We listed the mostly used methods for this purpose and then we described some of them that will be assessed and compared in the next chapter.

Chapter 4

Performance evaluation

4.1 Introduction

We compare the performance of the conventional subspace methods and TF methods in the presence of nonstationary signals. The effects of incorporating auto- and cross-terms in the TFA and JBD processes are assessed and compared. The performances of some auto- and cross-terms selection methods are evaluated. Finally, the performance of TF DOAs of source with unknown signatures is compared to the optimal case of known signatures.

4.2 Conventional and time-frequency DOAs estimation

In this section we compare the performance of the conventional and time-frequency DOAs estimation methods in terms of location accuracy and resolution capability assuming that the signals signatures are known. We evaluate the effects of noise and the number of sensors upon the performance for different TFD kernels.

For all the simulations we use two chirp signals of unit variance having the same spectral shape and occupy the same time interval but with different time-frequency signatures. The chirp signals are modeled by Eqs. 1.71 and 1.72. The start and end frequencies of the two chirps are $(w_{1s}, w_{1e}) = (0, \pi)$ rad and $(w_{2s}, w_{2e}) = (\pi, 0)$ rad respectively. The signals arrive at $\theta_1 = -1$ degrees and $\theta_2 = 1$ degrees respectively.

The noise used is zero-mean Gaussian distributed spatially and temporally white. The noise power σ_n^2 is adjusted to give the desired SNR defined as :

$$SNR = 10 \log_{10}(\sigma_n^{-2})$$

A uniform linear array of M elements separated by half a wavelength and an observation interval of $N = 256$ snapshots are considered.

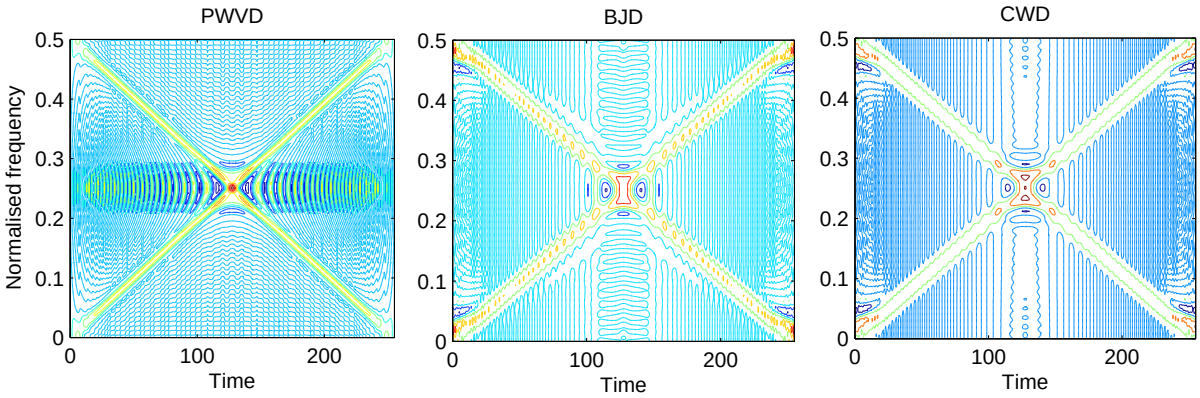

Figure 4.1: The TFDs of chirp signals in the first array sensor

Three types of time-frequency distributions are used:

1. Pseudo Wigner-Ville Distribution (PWVD) with a Hamming window of length $L_h = 65$.
2. Born-Jordan Distribution (BJD) with $\alpha = 1$
3. Choi-Williams Distribution (CWD) with $\sigma = 0.2$

Fig. 4.1 shows the three TFDs of the free-noise chirp signals received by the first array sensor.

We use 192 (t, f) points of each source signature in the averaging of STFD matrices to obtain $\hat{\mathbf{D}}_{\mathbf{xx}}$ (Eq. 3.33).

In all the simulations a total of $MC = 300$ independent Monte Carlo simulation runs are used.

4.2.1 Comparison of the location accuracy

As a measure of location accuracy we use the root mean-squared error $(RMSE)$ defined by Eq. 1.73. The $RMSE$ is evaluated versus the SNR and the number of array sensors to study their effects.

4.2.1.1 Effect of noise

A ten-element ULA is used. The SNR is varied from -12 to 14 dB. Figs. 4.2 to 4.6 show that the time-frequency versions of root-MUSIC, root-Min-Norm and ESPRIT have better location accuracy than the conventional ones especially in the case of low SNR. The PWVD offers better location accuracy than the BJD and CWD.

4.2.1.2 Effect of the number of sensors

We set the SNR=5dB and we vary the number of sensors from 3 to 16. Figs. 4.7 to 4.9 indicate that there is an improvement in the location accuracy offered by the time-frequency methods and it is more pronounced when the number of sensors is small. The PWVD outperforms the two other distributions.

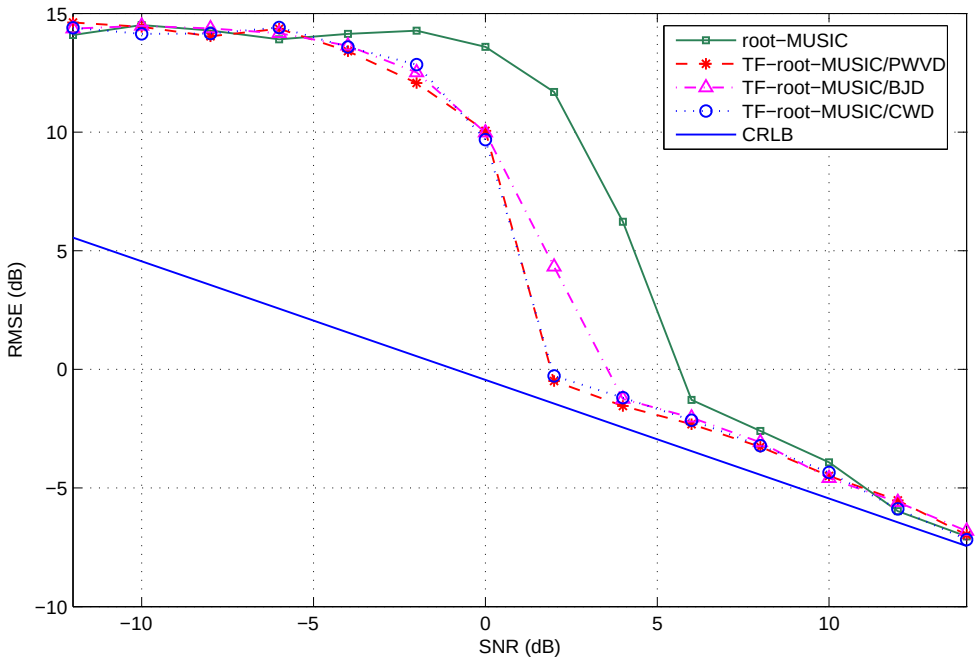

Figure 4.2: Root-MUSIC and TF-root-MUSIC: RMSE versus SNR

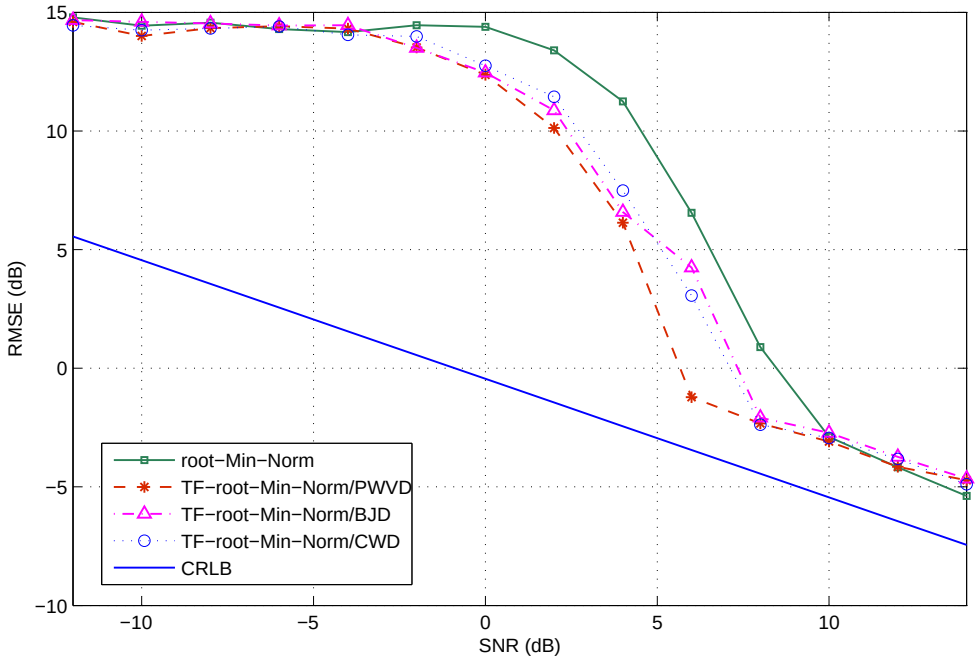

Figure 4.3: Root-Min-Norm and TF-root-Min-Norm: RMSE versus SNR

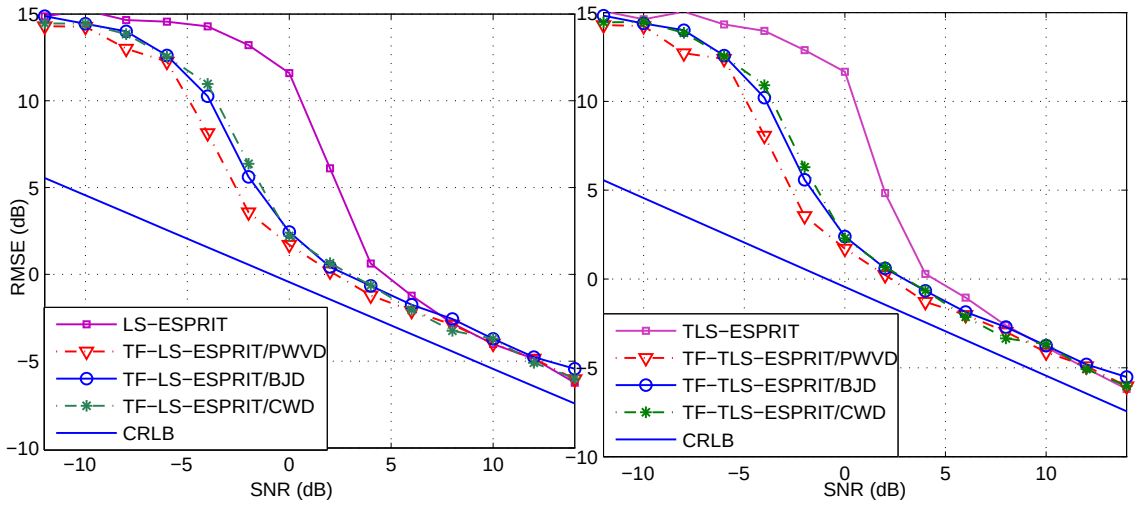

Figure 4.4: ESPRIT and TF-ESPRIT (m=1): RMSE versus SNR

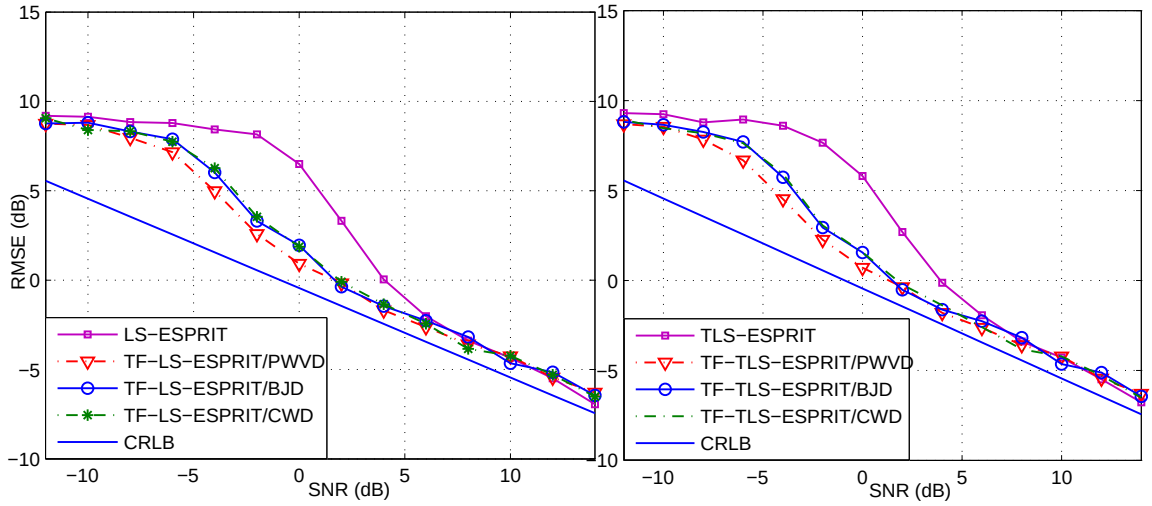

Figure 4.5: ESPRIT and TF-ESPRIT (m=3): RMSE versus SNR

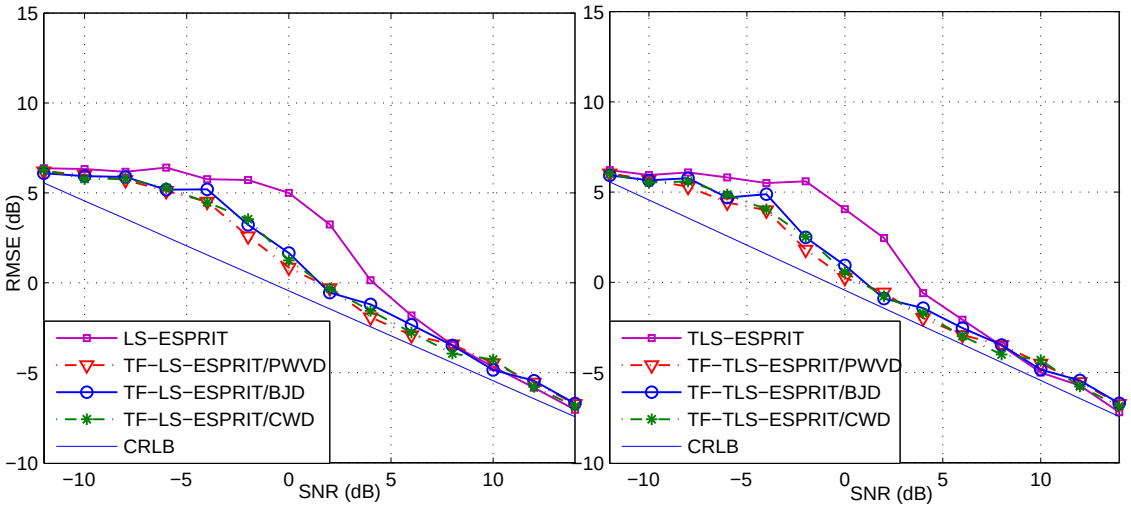

Figure 4.6: ESPRIT and TF-ESPRIT (m=5): RMSE versus SNR

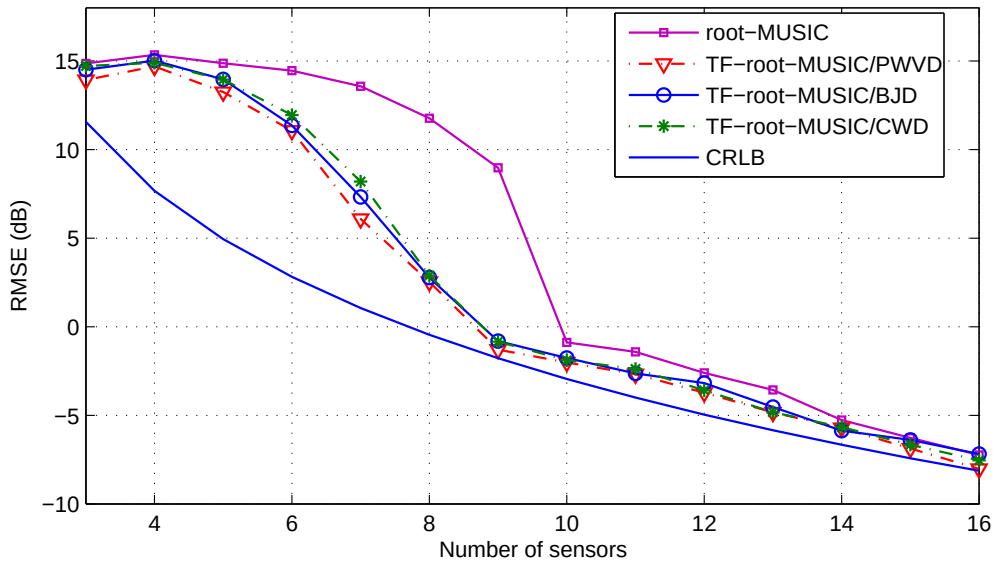

Figure 4.7: Root-MUSIC and TF-root-MUSIC: RMSE versus number of sensors

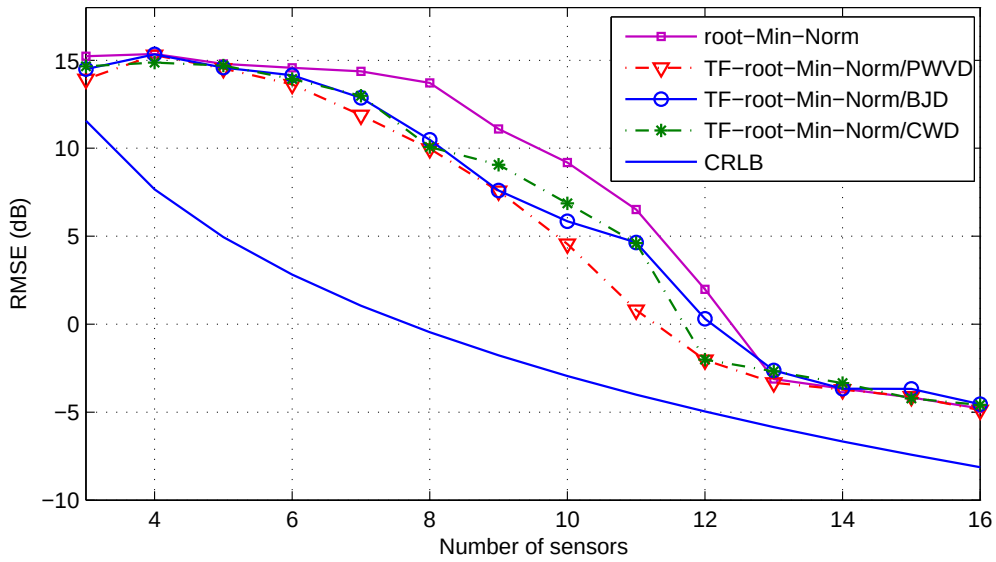

Figure 4.8: Root-Min-Norm and TF-root-Min-Norm: RMSE versus number of sensors

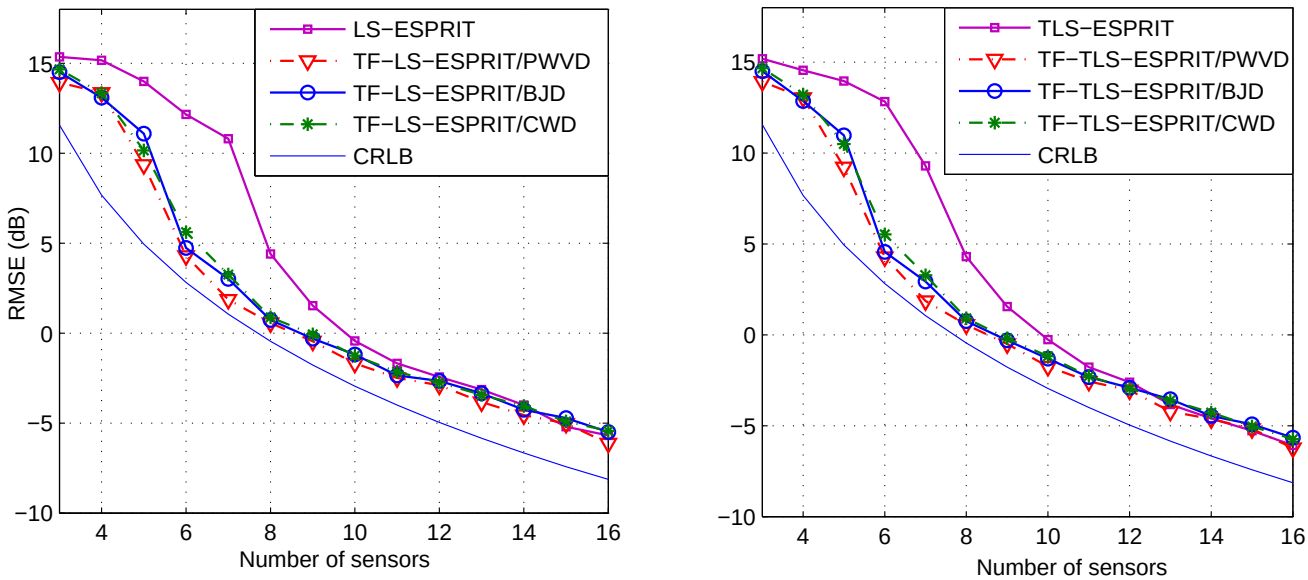

Figure 4.9: ESPRIT and TF-ESPRIT (m=1): RMSE versus number of sensors

4.2.2 Comparison of the resolution capability

The resolution is the ability to distinguish closely spaced sources. We adopt the probability of resolution as a measure of the resolution capability. The probability of resolution is obtained from Eq. 1.74. We compare the resolution capability of the conventional and time-frequency methods.

4.2.2.1 Effect of noise

A ten-element ULA is used. The SNR is varied from -12 to 14 dB. Figs. 4.10 to 4.14 reveal that the time-frequency methods have better resolution than the conventional ones. The use of PWVD offers improved resolution than when BJD or CWD are used.

4.2.2.2 Effect of the number of sensors

We set the SNR=5dB and we vary the number of sensors from 3 to 16. Figs. 4.15 to 4.17 show that the time-frequency methods have better resolution than the conventional ones especially when the number of sensors is small.

4.2.3 Comparison of the execution time

A ten-element ULA is used. The SNR is set equal to $2dB$. Fig. 4.18 illustrates the average execution time of the TF and conventional root-MUSIC for $M = 10$ and $SNR = 2dB$. We notice that the TF methods have longer execution time especially when the BJ or CW kernels are used. This figure suggests that a trade-off between the execution time and estimators performance should be considered when the TF methods are used.

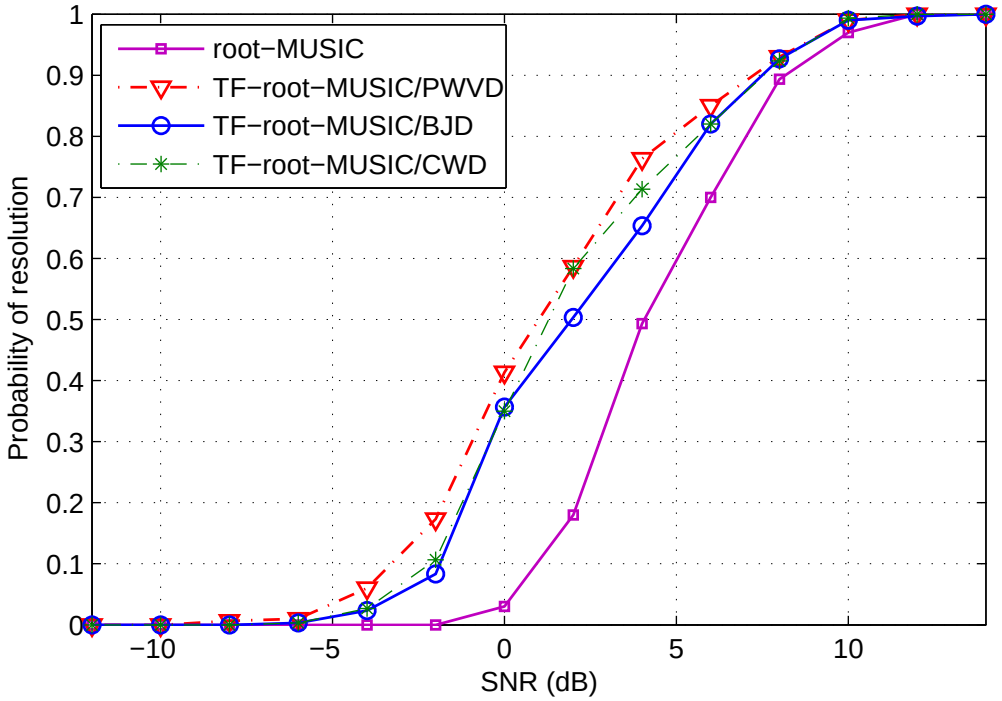

Figure 4.10: Root-MUSIC and TF-root-MUSIC: probability of resolution versus SNR

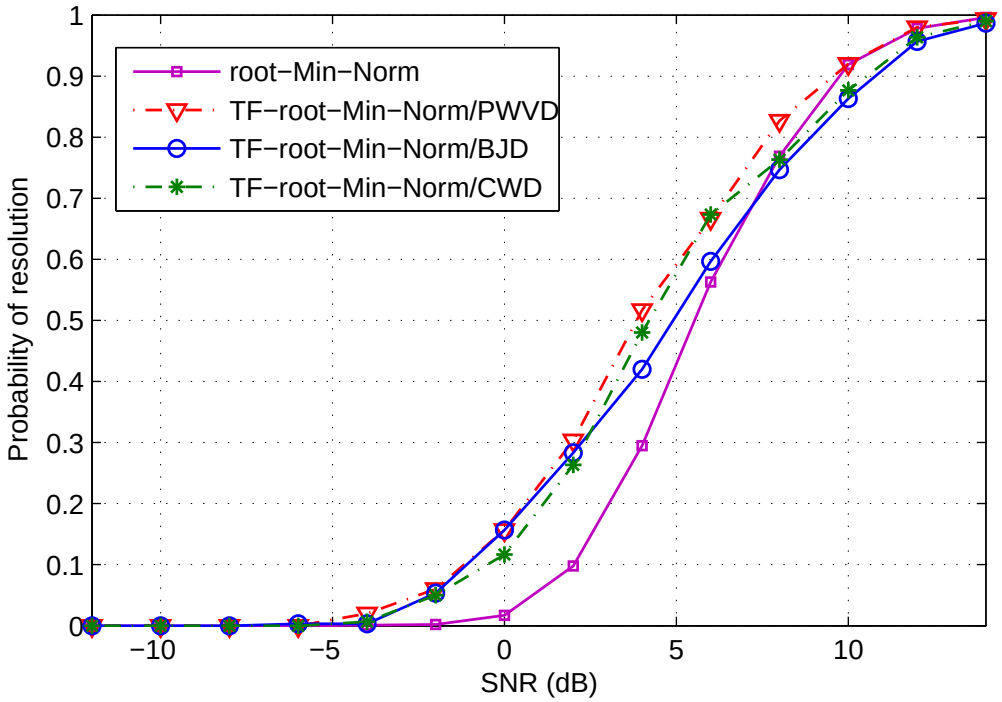

Figure 4.11: Root-Min-Norm and TF-root-Min-Norm: probability of resolution versus SNR

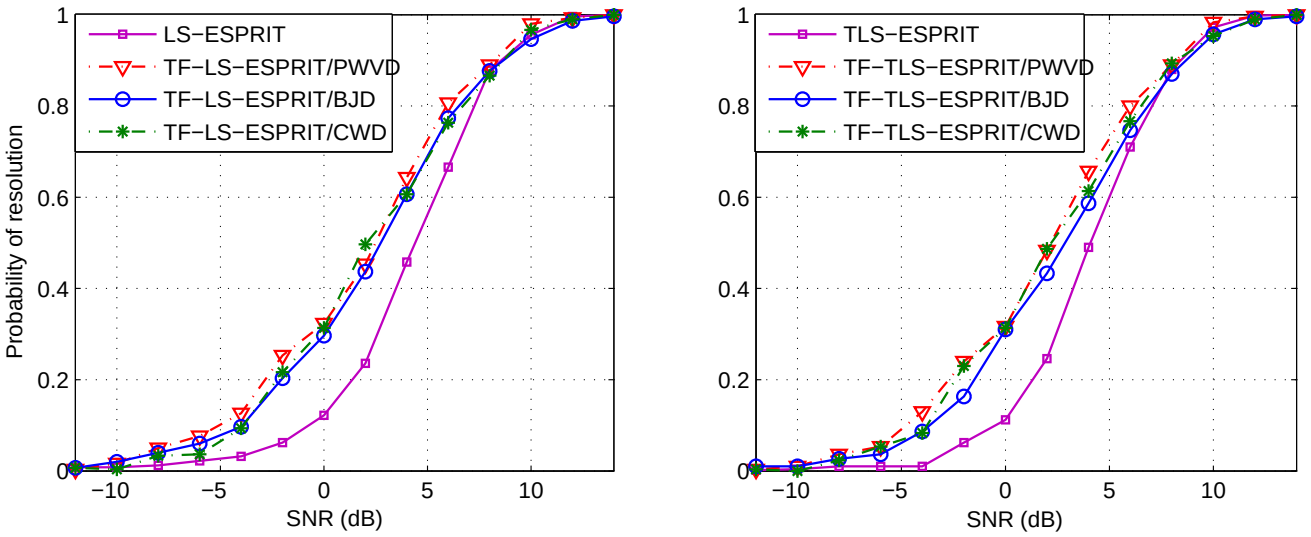

Figure 4.12: ESPRIT and TF-ESPRIT (m=1): probability of resolution versus SNR

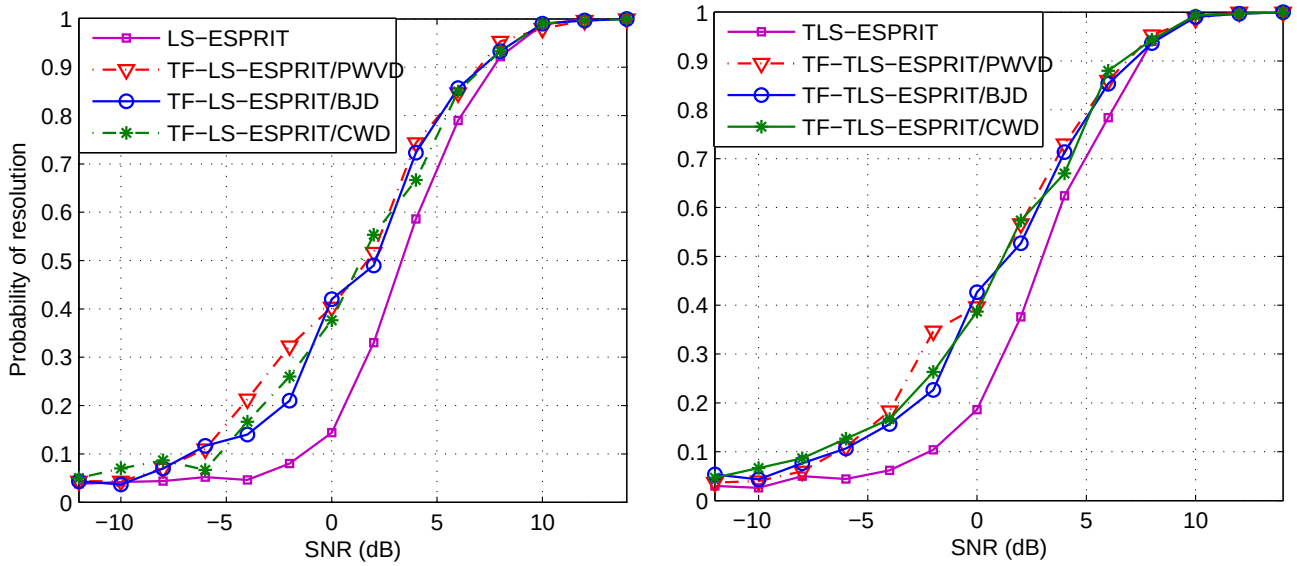

Figure 4.13: ESPRIT and TF-ESPRIT (m=3): probability of resolution versus SNR

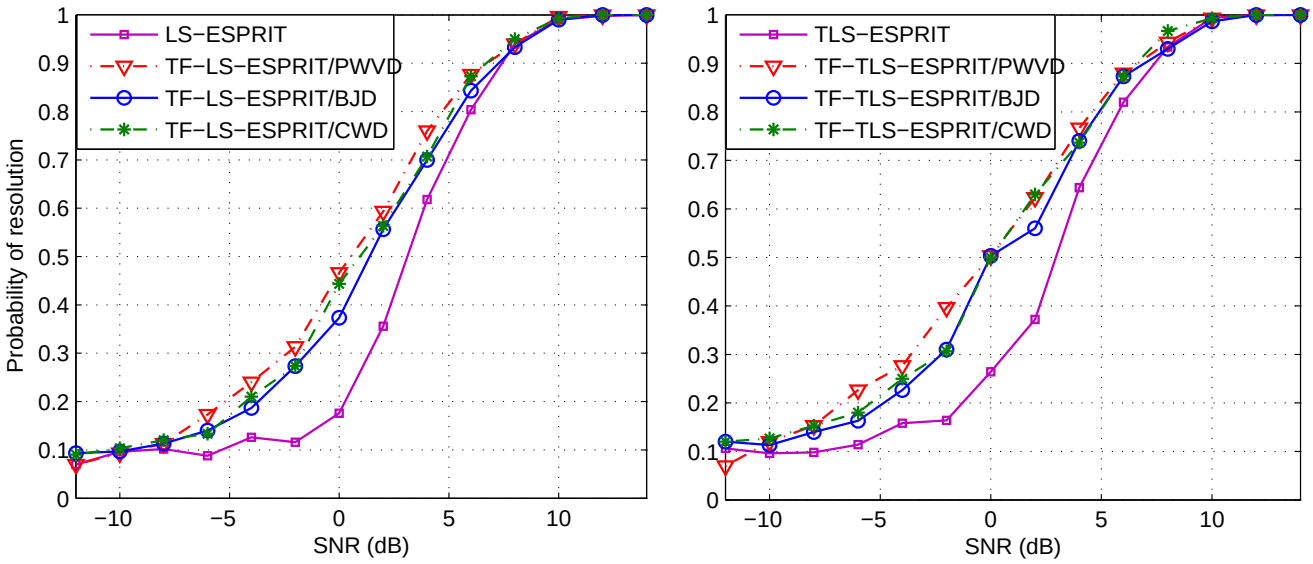

Figure 4.14: ESPRIT and TF-ESPRIT (m=5): probability of resolution versus SNR

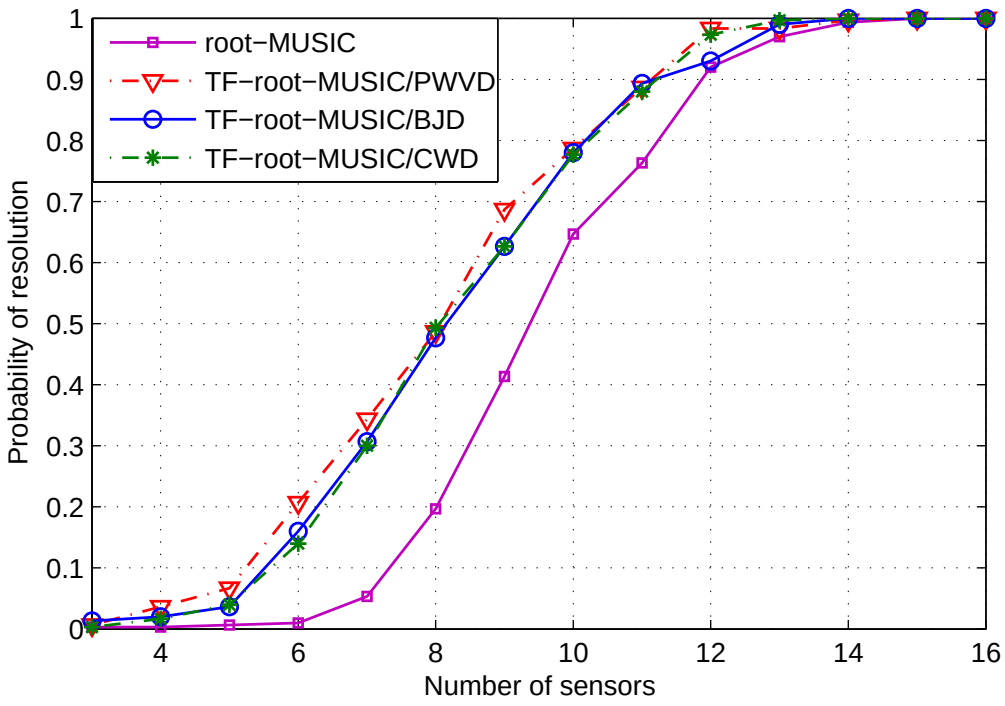

Figure 4.15: Root-MUSIC and TF-root-MUSIC: probability of resolution versus number of sensors

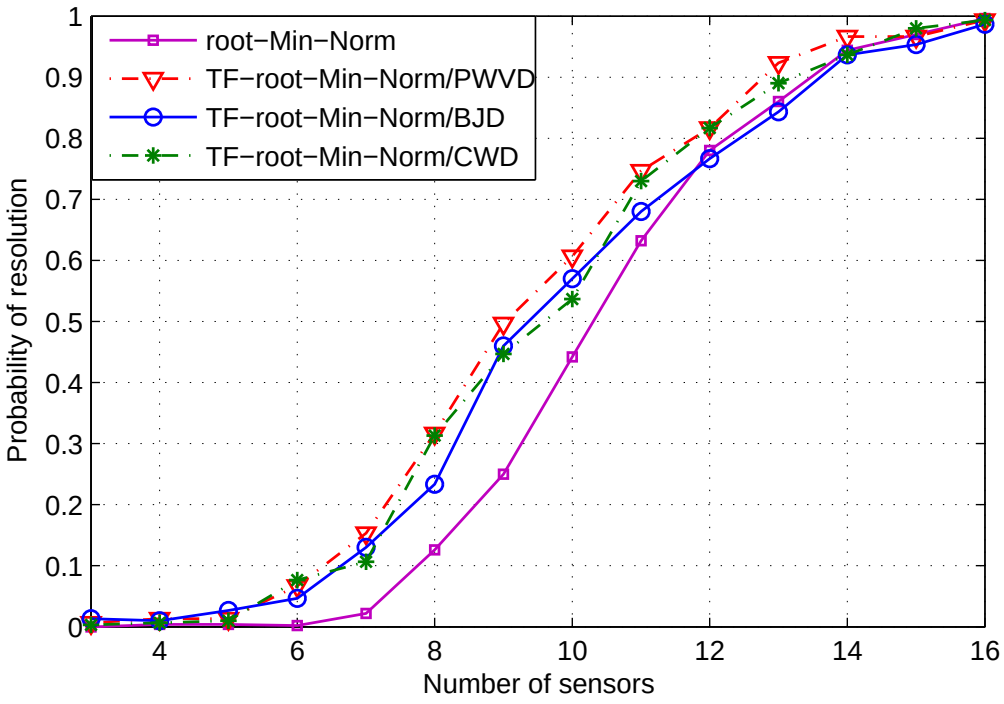

Figure 4.16: Root-Min-Norm and TF-root-Min-Norm: probability of resolution versus number of sensors

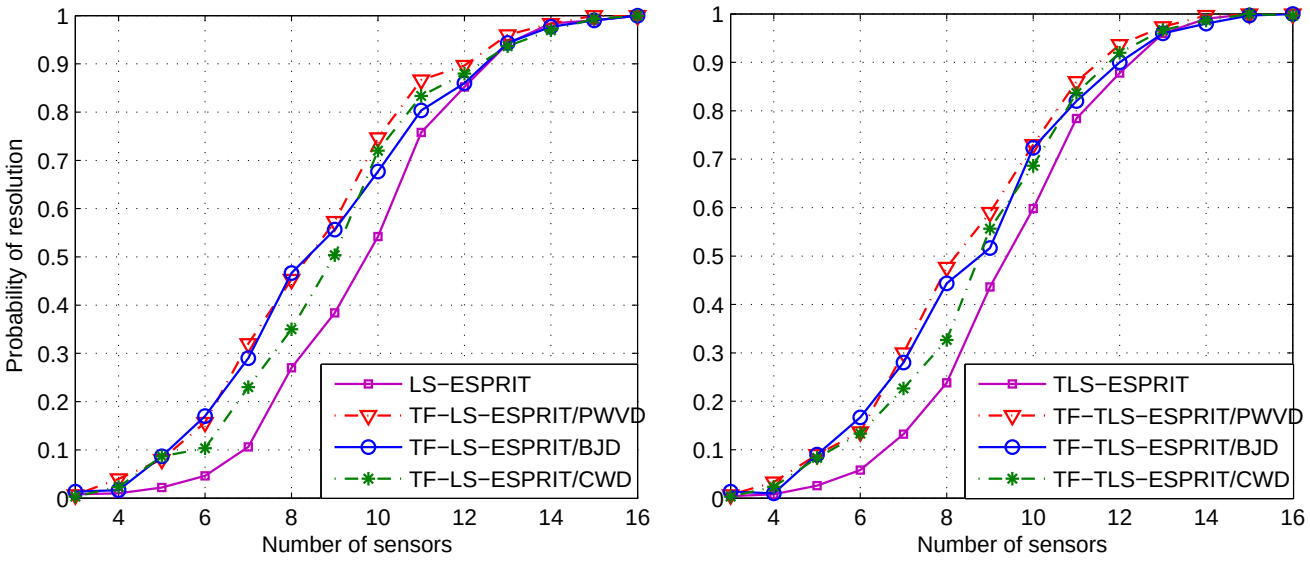

Figure 4.17: ESPRIT and TF-ESPRIT (m=1): probability of resolution versus number of sensors

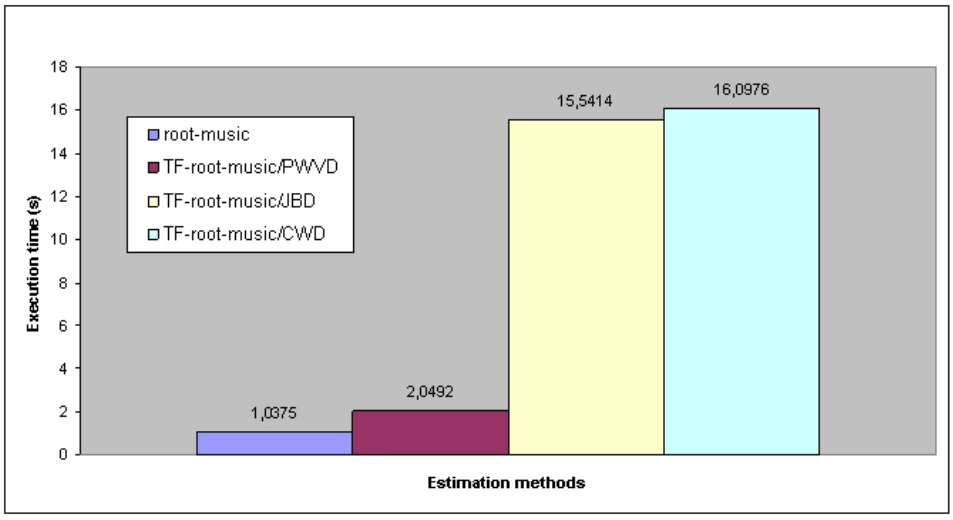

Figure 4.18: Execution time: conventional and TF methods

4.3 Auto-terms versus cross-terms incorporation

The purpose of this section is to study the effect of incorporating cross-terms and auto-terms when TFA or JBD are used as an incorporation method.

Two chirp signals are received. The start and end frequencies of the two chirps are $(w_{1s}, w_{1e}) = (\pi, 0.2\pi)$ rad and $(w_{2s}, w_{2e}) = (0.8\pi, 0)$ rad respectively. The signals arrive at $\theta_1 = -10$ degrees and $\theta_2 = 10$ degrees respectively. The noise used is zero-mean Gaussian distributed spatially and temporally white. A ULA of six elements separated by half a wavelength, an observation interval of N = 256 snapshots and PWVD with a Hamming window of length $L_h = 65$ are considered. Fig. 4.19 shows the PWVD of the mixed signals at the first sensor.

We consider the auto-terms and cross-terms in the following two regions:

1. Auto-term regions (t, f_1) with $f_1(t) = 0.5 - 0.4t/N$ and (t, f_2) with $f_2(t) = 0.4 - 0.4t/N$
2. Cross-term region (t, f_c) with $f_c(t) = [f_1(t) + f_2(t)]/2 = 0.45 - 0.4t/N$

Figs. 4.20, 4.21 and 4.22 give the RMSE of the first DOA when 192 (t, f) points belonging, respectively, to the auto-term regions, cross-term region and both are incorporated in the TFA and JBD processes. TF-TLS-ESPRIT with a separation of half a wavelength $(m = 1)$ between the two subarrays is considered. The number of iteration used by the approximate JBD algorithm is 20.

These figures clearly show that the JBD offers better performance than the TFA in all the three cases and its performance is roughly independent from the regions selected (auto-terms regions, cross-term region or both). On the other hand, the TFA leads to very degraded performance when the (t, f) points selected belong to the cross-term region. This is true because the cross-terms change over time t, taking both positive and negative values, adding them at different (t, f) points in the TFA process yield small smoothed values. However, the execution time of the JBD is longer than that of the TFA as revealed by Fig. 4.24.

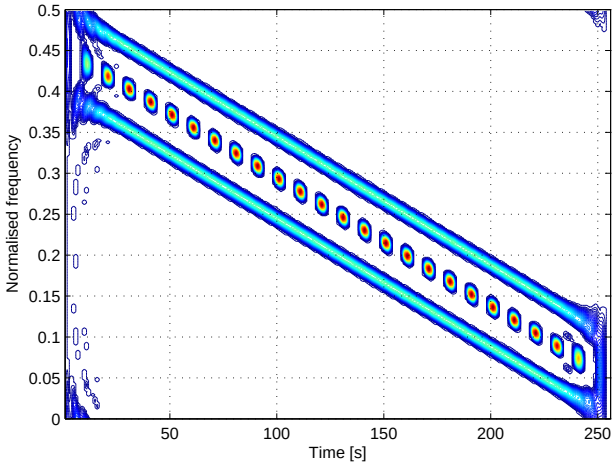

Figure 4.19: PWVD of two chirp signals

The RMSE can be lower than the deterministic CRLB because the displayed bound assumes unknown deterministic stationary signals and does not take into consideration the chirp signal structure which was used in performing the DOAs estimation.

To further improve the performance of the algorithm, we can select from the auto-term regions the (t, f) points that belong to particular signals. For example, Fig. 4.23 shows the RMSE when one and two signal signatures are incorporated in the TFA process. We notice that better performance is offered when only one signal signature is selected from the auto-term regions.

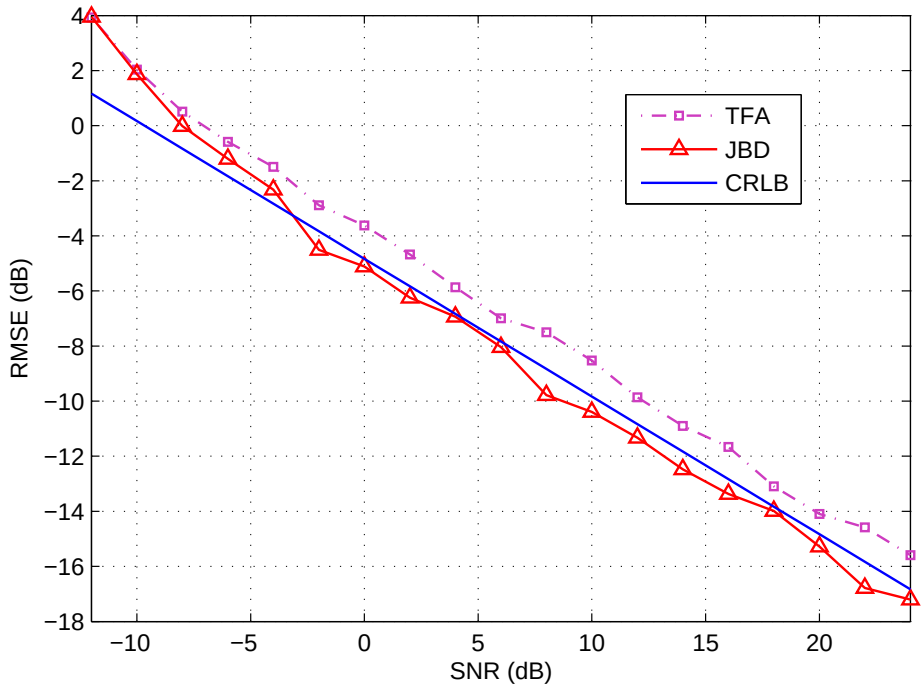

Figure 4.20: Auto-term regions: RMSE versus SNR for TF-TLS-ESPRIT (m=1)

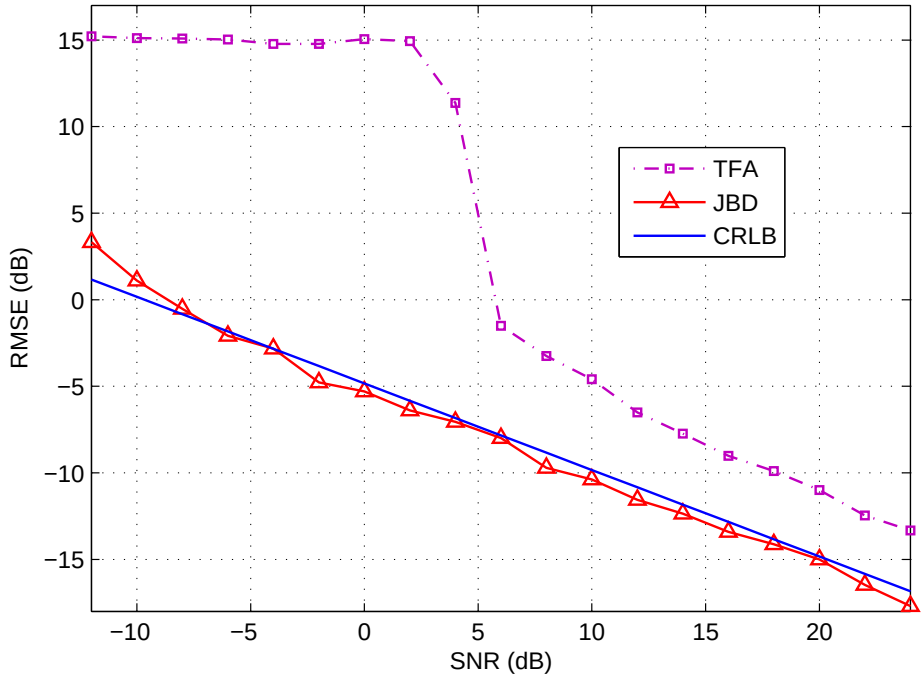

Figure 4.21: Cross-term region: RMSE versus SNR for TF-TLS-ESPRIT (m=1)

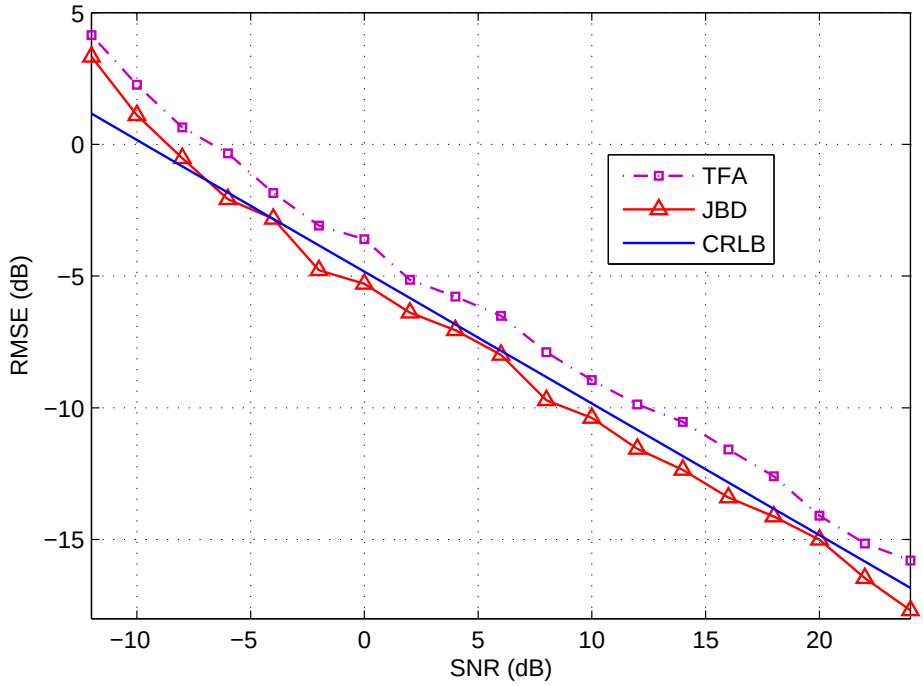

Figure 4.22: Auto-term and cross-term regions: RMSE versus SNR for TF-TLS-ESPRIT (m=1)

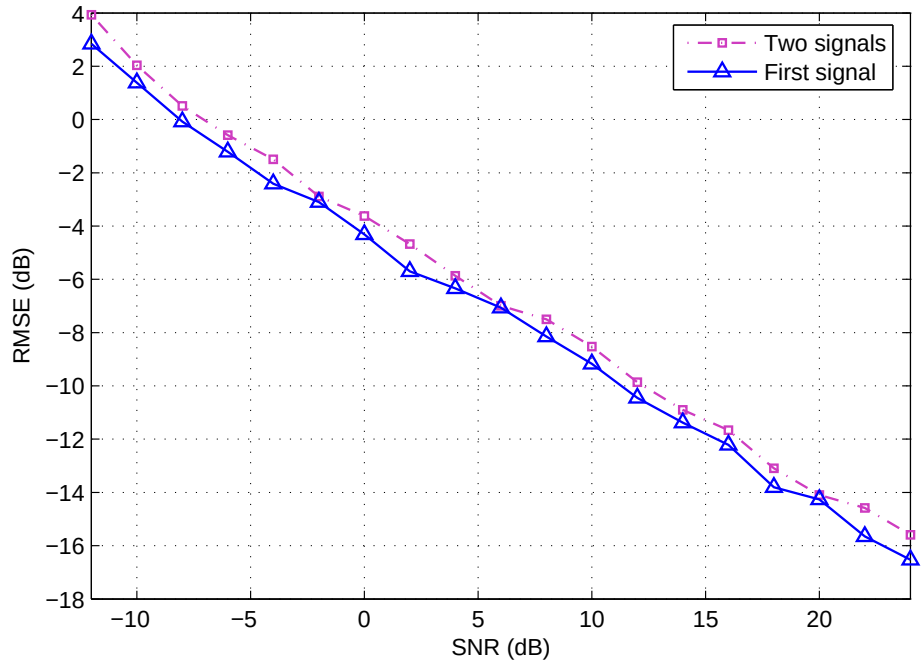

Figure 4.23: Selection of particular signals: RMSE versus SNR for TF-TLS-ESPRIT (m=1)

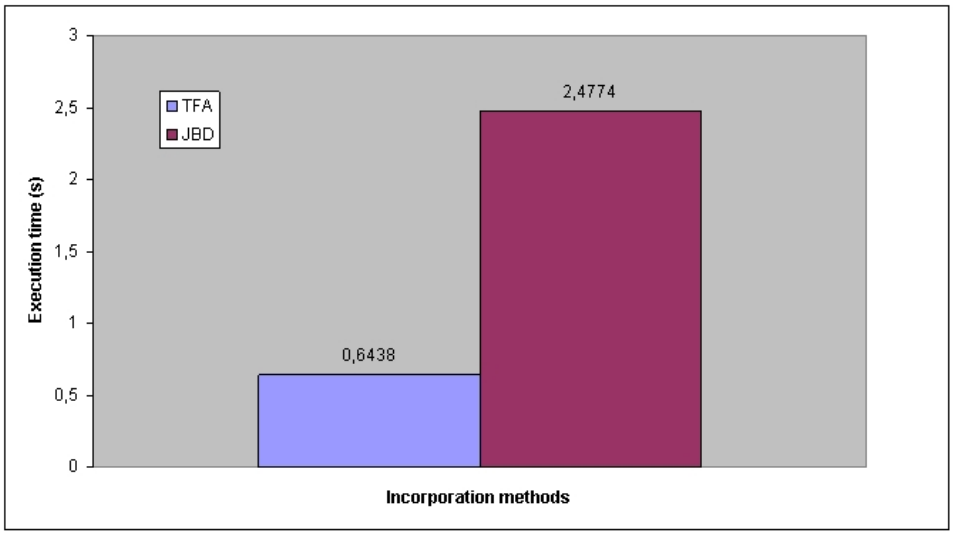

Figure 4.24: Execution time: TFA and JBD methods

4.4 Selection of auto- and cross-terms

In this section we present some simulation results demonstrating the performance of the described methods for the selection of auto-terms and cross-terms points. In this section, PBM, BBM and VCBM denote the Projection Based Method, Bootstrap Based Method and Vector Clustering Based Method, respectively.

For the purpose of performance evaluation and comparison between the aforementioned methods, we use the Receiver Operating Characteristic (ROC) as performance index. The ROC gives the probability of correct selection for a particular probability of false selection.

The set of TF locations obtained by point selection of auto- and cross-terms are respectively denoted $\hat{\mathbf{S}}_A$ and $\hat{\mathbf{S}}_C$. Accordingly, empirical probabilities of detection and false alarm are defined as follows:

$$P_D = \#\left\{\mathbf{S}_A \cap \hat{\mathbf{S}}_A\right\} / \#\left\{\mathbf{S}_A\right\} \qquad \text{For auto-term points}$$
$$P_D = \#\left\{\mathbf{S}_C \cap \hat{\mathbf{S}}_C\right\} / \#\left\{\mathbf{S}_C\right\} \qquad \text{For cross-term points}$$

$$P_{FA} = \#\left\{\mathbf{S}_A - \hat{\mathbf{S}}_A\right\} / \#\left\{\mathbf{S}_T - \mathbf{S}_A\right\} \qquad \text{For auto-term points}$$
$$P_{FA} = \#\left\{\mathbf{S}_C - \hat{\mathbf{S}}_C\right\} / \#\left\{\mathbf{S}_T - \mathbf{S}_C\right\} \qquad \text{For cross-term points}$$

where $\mathbf{S}_A$, $\mathbf{S}_C$ and $\mathbf{S}_T$ are the sets of auto-term points, cross-term points and total TF points respectively. $\#\{.\}$ denotes the number of elements in the considered set.

The threshold of each selection method was varied in order to generate the receiver operating characteristic. We consider a scenario with two source signals impinging on the array at -10 and 10 degrees. The source signals $s_1(t)$ and $s_2(t)$ are chirp signals with start and end frequencies $(\pi, 0.2\pi)$ and $(0.8\pi, 0)$

radians respectively. The noise used is zero-mean Gaussian distributed spatially and temporally white with variance σ_n^2. Since the signals are chirps, we employ the PWVD with a Hamming window of length $L_h = 33$. The number of Monte Carlo runs considered is $MC = 100$ and the number of snapshots is $N = 256$.

The BBM uses a total of $B = 20$ bootstrap estimates to compute σ_T^2 and one dimensional rectangular filter of length 5 to smooth the TFDs along each time-slice.

The ROCs of the three methods for auto- and cross-terms are shown in Figs. 4.25 and 4.26 for $SNR = 0$, -5 and $-10dB$ and $M = 5$ sensors. As shown in these two figures, the BBM outperforms the other methods, especially for low SNR, in the selection of both auto- and cross-terms. When the SNR increases the performances of the three methods for the selection of auto-terms tend to be similar. Since the BBM involves high computational cost, the PBM and VCBM are worth using in scenarios of high SNR. Fig. 4.29 provides the average execution time of these three methods for $M = 5$ and $SNR = -5dB$.

The effect of the number of sensors on the performance of the three methods is illustrated in Figs. 4.27 and 4.28 for both auto- and cross-terms for $SNR = -5dB$. For all values of M and for both auto- and cross-terms selection, the BBM is better than the others. As the number of sensors used increases, the three methods tend to have similar performances.

Although the VCBM has the worst performance in the simulated scenarios, it can select the auto-terms of each source separately. This allows us to improve the performance of DOA estimation method as demonstrated in section 4.3. An illustrative example is provided in Figs. 4.30 and 4.31, showing the selection of auto-term points of two chirp signals. Fig. 4.30 shows the mixture of two chirp signals received by the first sensor. The VCBM is able to separate the auto-terms belonging to each source as shown in Fig. 4.31.

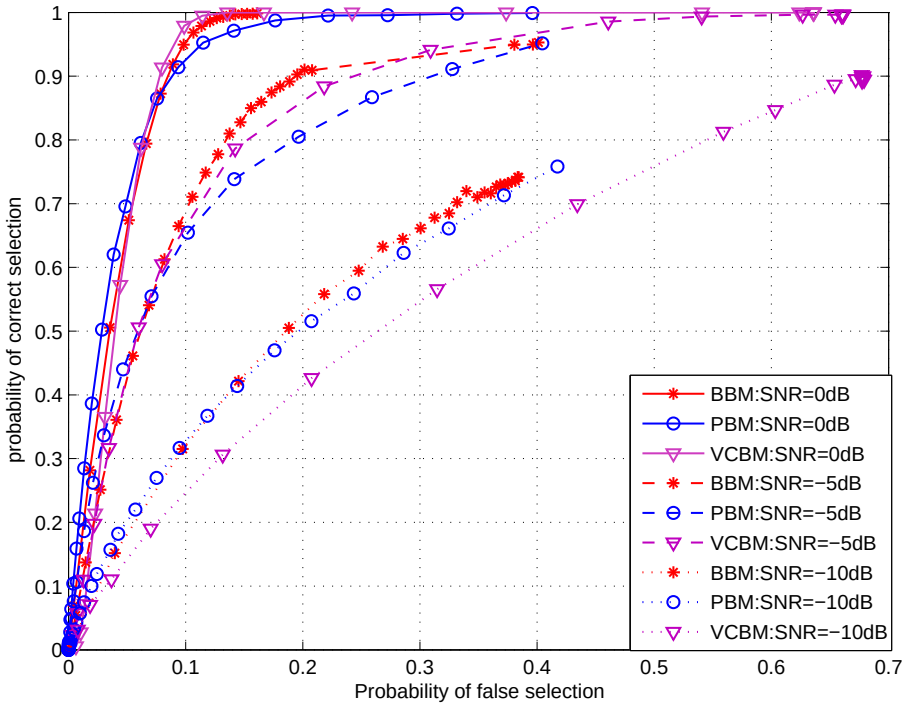

Figure 4.25: Receiver Operating Characteristic of auto-terms: SNR=0, -5 and -10dB

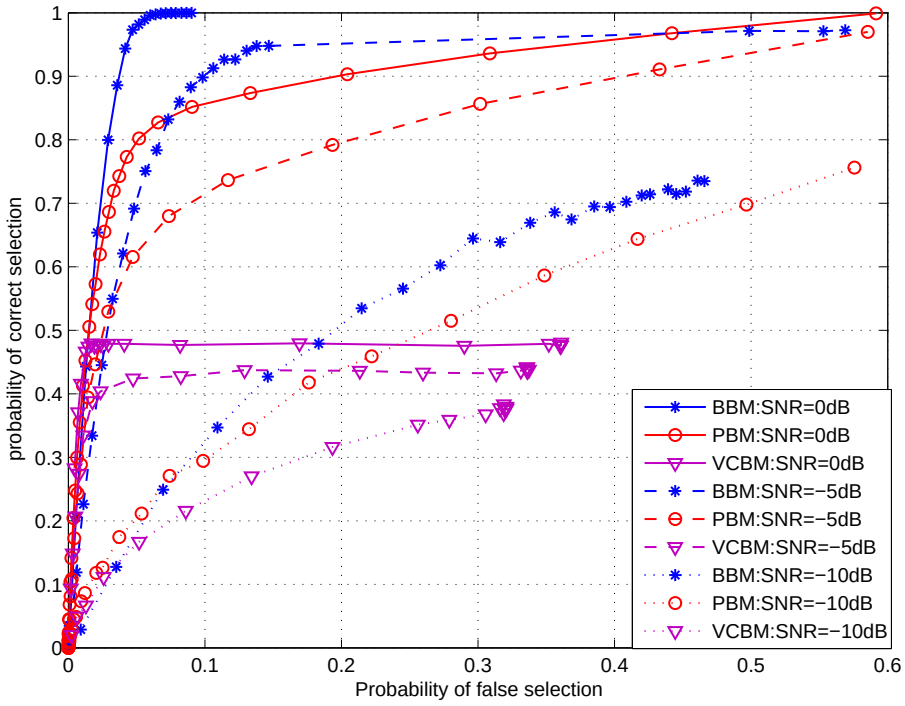

Figure 4.26: Receiver Operating Characteristic of cross-terms: SNR=0, -5 and -10dB.

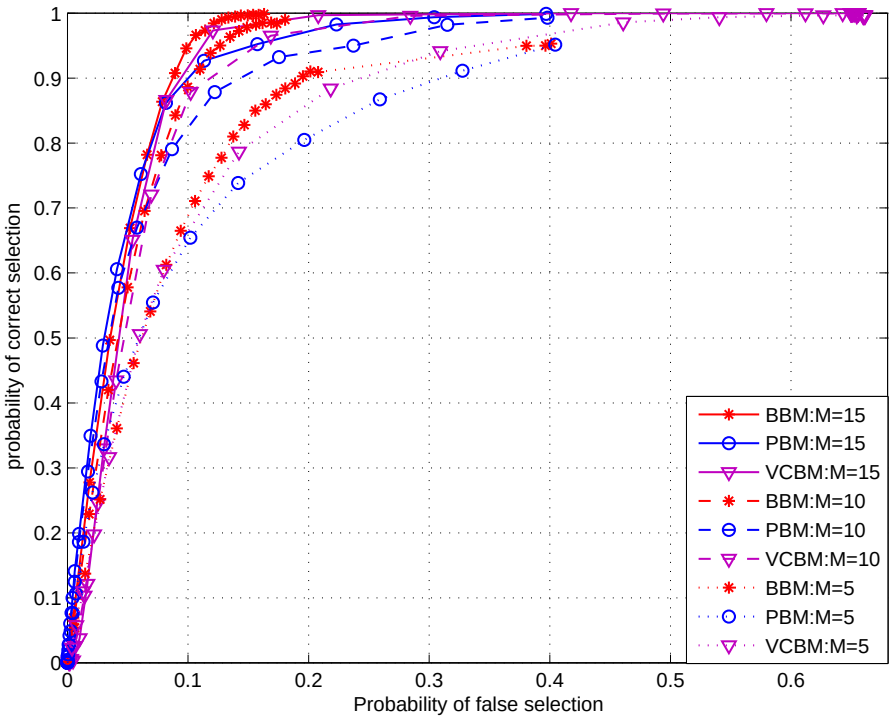

Figure 4.27: Receiver Operating Characteristic of auto-terms: M=15, 10 and 5 sensors

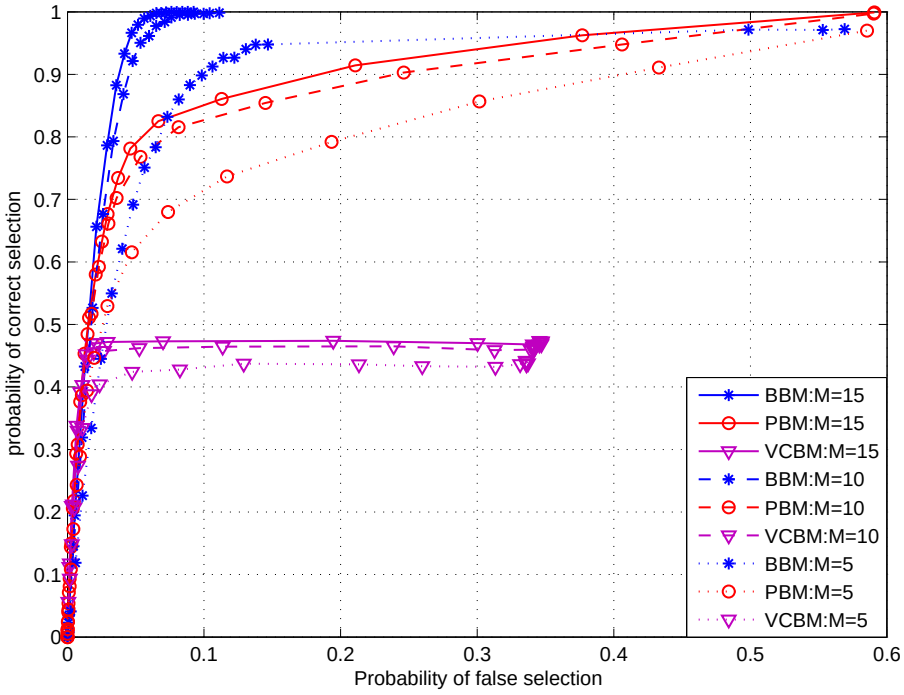

Figure 4.28: Receiver Operating Characteristic of cross-terms: M=15, 10 and 5 sensors.

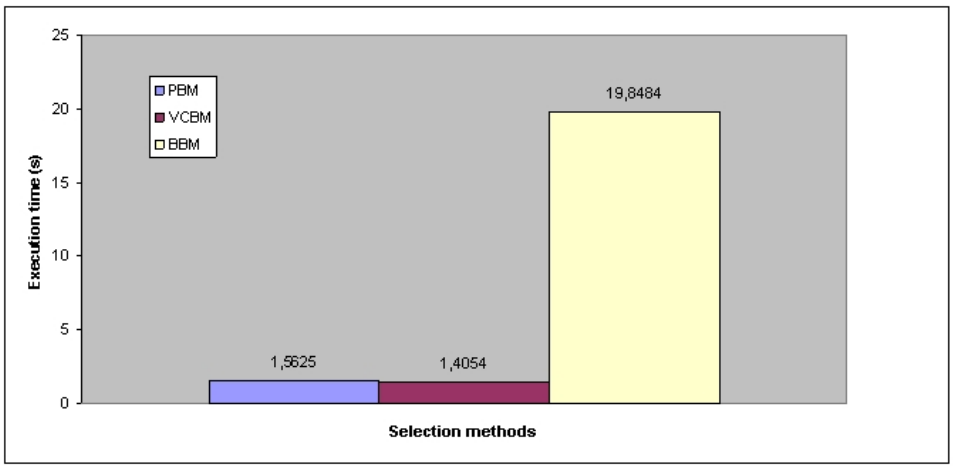

Figure 4.29: Execution time: selection methods

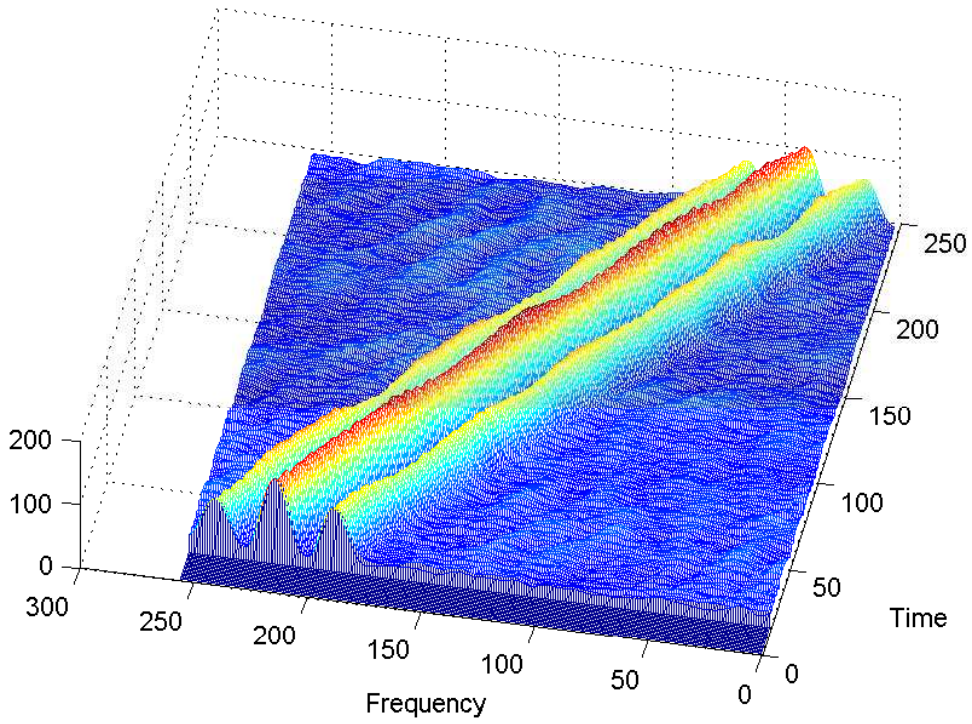

Figure 4.30: PWVD of two chirp signals: SNR=5dB

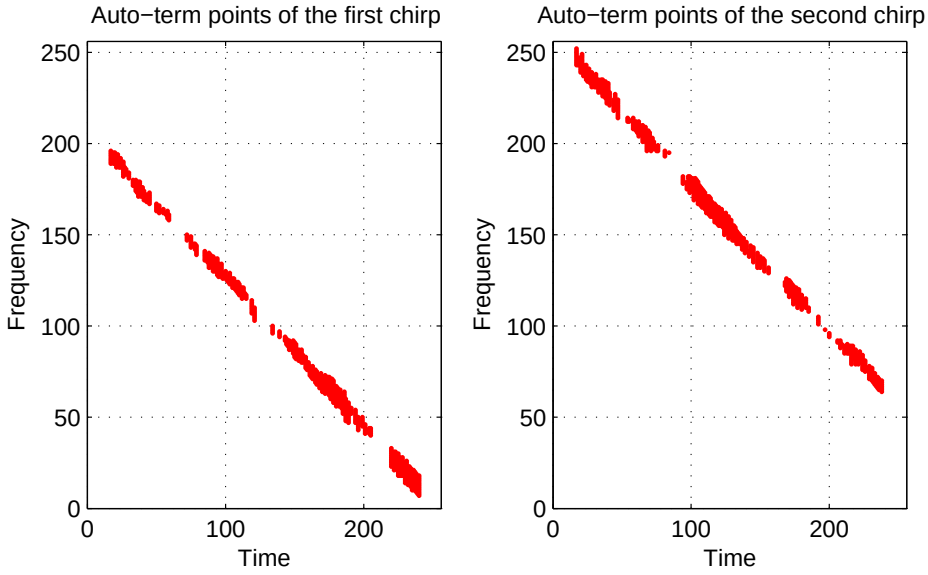

Figure 4.31: Auto-term points of the first and second chirp separated

4.5 TF DOAs estimation of sources with unknown signatures

The aim of this section is to demonstrate that we can estimate the DOAs of non-stationary sources with completely unknown TF signatures. To achieve this, we apply two successive estimations. We start by estimating the signatures of the sources using the algorithms given in section 3.6 and then we estimate the DOAs of these sources using any TF DOAs estimation algorithm described in sections 3.3 to 3.5.

Two chirp signals are received. The start and end frequencies of the two chirps are $(w_{1s}, w_{1e}) = (\pi, 0.2\pi)$ rad and $(w_{2s}, w_{2e}) = (0.8\pi, 0)$ rad respectively. The signals arrive at $\theta_1 = -10$ degrees and $\theta_2 = 10$ degrees respectively. A ULA of six elements separated by half a wavelength, an observation interval of N = 256 snapshots and PWVD with a Hamming window of length $L_h = 65$ are considered. As an auto-terms incorporation method, the TFA is used. Fig. 4.32 gives the RMSE of the first DOA when the selected (t, f) points belong to the auto-term regions for TF-TLS-ESPRIT algorithm. As the SNR increases the estimation accuracy tends to be similar to that of the optimal case (known signatures). From $SNR = 5dB$, the achieved accuracy is very close to the optimal case for the three simulated methods.

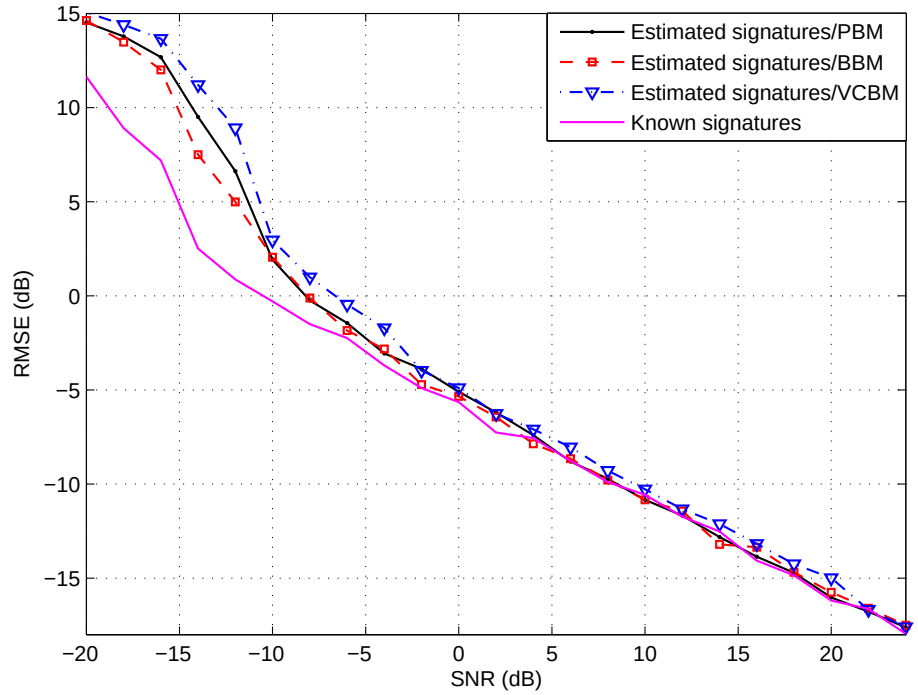

Figure 4.32: Estimated and known TF signatures: RMSE versus SNR for TF-TLS-ESPRIT (m=1)

4.6 Conclusion

The optimality of the PWVD for the representation of the chirp signals in the time-frequency domain was demonstrated through computer simulations. In comparison to the BJD and CWD, the application of the PWVD allows the achievement of the best location accuracy and resolution capability of the simulated TF subspace algorithms.

One of the interesting findings of this chapter is the fact that for some parameter range (e.g. the number of sensors and SNR), the application of the TF methods for DOAs estimation is worthwhile. Out of this parameter range, the TF DOAs estimation methods tend to have progressively the same performance, in terms of location accuracy and resolution capability, as the conventional methods. e.g. the use of TF-root-MUSIC with PWVD at $SNR = 2$ brought an improvement in the location accuracy as high as $12dB$ and the gap between the RMSE and CRLB is less than $1dB$, whereas when the SNR is out of the range of -4 to $+5dB$, the conventional root-MUSIC and TF-root-MUSIC tend to have the same performance. Since the TF DOAs estimation methods involve high computational cost, the conventional methods should be considered when the performances of both approaches are similar.

This chapter also reveals that the JBD method outperforms the TFA one when using multiple TF

points in both auto- or cross-term regions. The gap between these two method is the biggest (could be as much as $20dB$) when the considered points belong to the cross-term region. Furthermore, the selection of auto-terms belonging to one signal allows the improvement of the location accuracy by roughly $1dB$ in the simulated scenario. In the case of auto-term points, the JBD and TFA tend to have similar performance for low SNR. In such scenarios, the TFA is preferred to JBD as the latter has high computational cost.

The problem of auto- and cross-terms selection was also tackled in this chapter. We proved through simulation, the superiority of the BBM in terms of ROC over the VCBM and PBM for both auto- and cross-terms selection especially for low SNR and small number of sensors. When the SNR or the number of sensors increases, the gap between these methods decreases. Since the PBM has the lowest computational cost, it should be considered when the three methods have similar ROC. We also showed how the VCBM could be used to separate auto-term points belonging to different signals in order to improve the estimation accuracy and to cope with the problem of under-determined systems. In the last part, we demonstrated that thanks to the methods used for the detection of auto-terms we can estimate the DOAs of nonstationary sources with unknown TF signatures. For the simulated scenario, the accuracy of this estimation is very close to the optimal case for $SNR > 5dB$.

Chapter 5

CTF-DOAs Tool presentation

5.1 Introduction

This chapter presents a simulation tool for conventional and time-frequency directions of arrival estimation. The tool can be used to rapidly study and compare the conventional and time-frequency DOAs estimation methods in given scenario. This tool can also be used for computer-aided learning of DOAs estimation.

5.2 Graphical user interface

The conventional algorithms such as Bartlett, Capon, Linear Prediction, MUSIC, Root-MUSIC, Min-Norm, Root Min-Norm and ESPRIT as well the corresponding time-frequency algorithms have been implemented using MATLAB version 7.0. A GUI has also been built to ease the simulation. The layout of the starting GUI is depicted in Fig. 5.1. There are three modules: auto- and cross-terms detection, spectral methods and evaluation.

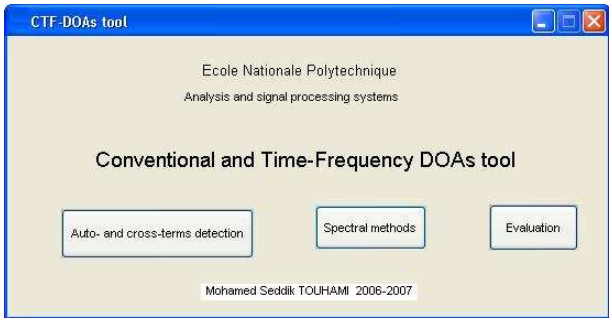

Figure 5.1: The layout of the starting GUI

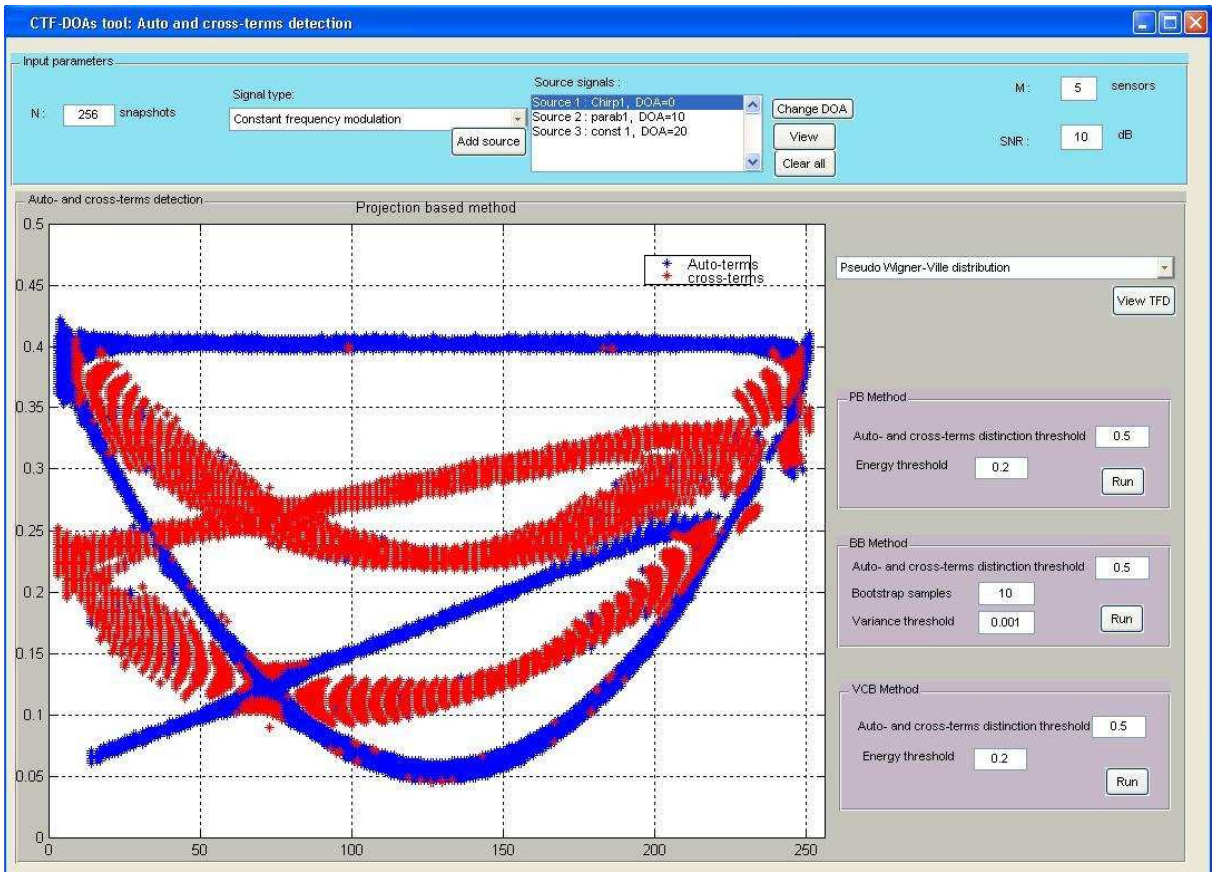

Figure 5.2: The layout of auto- and cross-terms detection module

5.2.1 Auto- and cross-terms detection module

The user can input the number and type of signals: stationary and nonstationary signals. Signals having IF laws of constant, parabolic, hyperbolic, sinusoidal or linear forms can be considered. The DOAs, the number of snapshots, the number of sensors, the SNR and the type of the time-frequency distribution can be changed to study their effects on the detection of auto- and cross-terms. For the detection of auto- and cross-terms, three methods are implemented, namely the PBM, BBM and VCBM whose parameters can also be varied. As an example, Fig. 5.2 shows the detected auto- and cross-terms of three signals having constant, parabolic and linear IF laws when the PBM is used.

5.2.2 Spectral methods module

In addition to the configuration of the impinging signals, the number of snapshots, the number of sensors and the SNR, the user can simultaneously visualise the spatial spectra of the conventional and TF methods. As conventional methods, the Capon, Bartlett, linear prediction, spectral music and min-norm algorithms are implemented. In the case of TF methods, the employed TFD, the selected sources and the number of

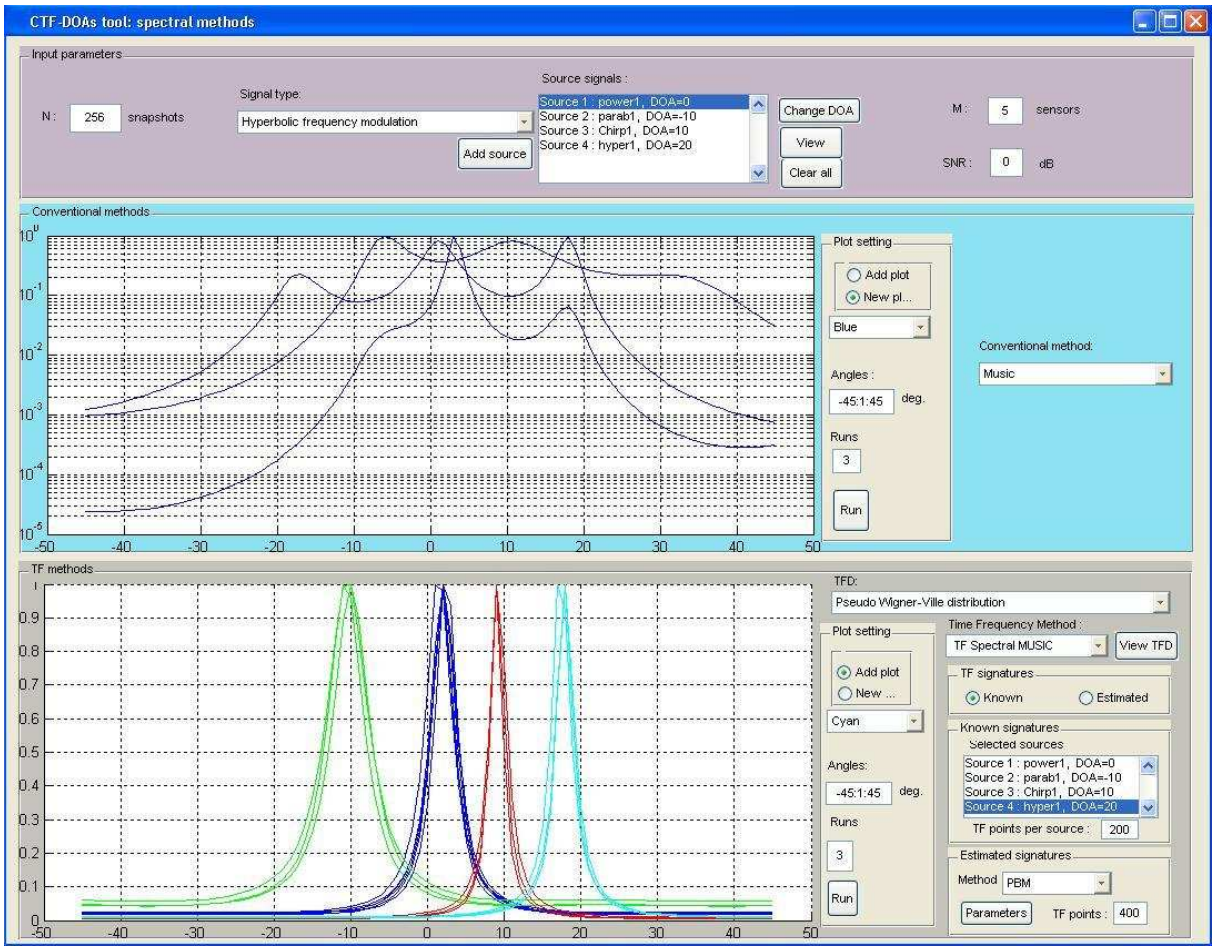

Figure 5.3: The layout of spectral methods module

(t, f) points considered can be customized. Furthermore, the user has an option to use directly the TF signal signatures or to estimate them using any one of the aforementioned algorithms. Fig. 5.3 gives the layout of this module.

5.2.3 Evaluation module

The evaluation module is designed to quantitatively compare the methods. The user can compare a conventional method with its corresponding TF version using the $RMSE$ as a performance index. In addition to the all previously mentioned parameters, the user can specify the SNR interval and the number of Monte-Carlo runs. Fig. 5.4 provides an example of comparison between root-MUSIC and TF-root-MUSIC when two chirp signals are considered.

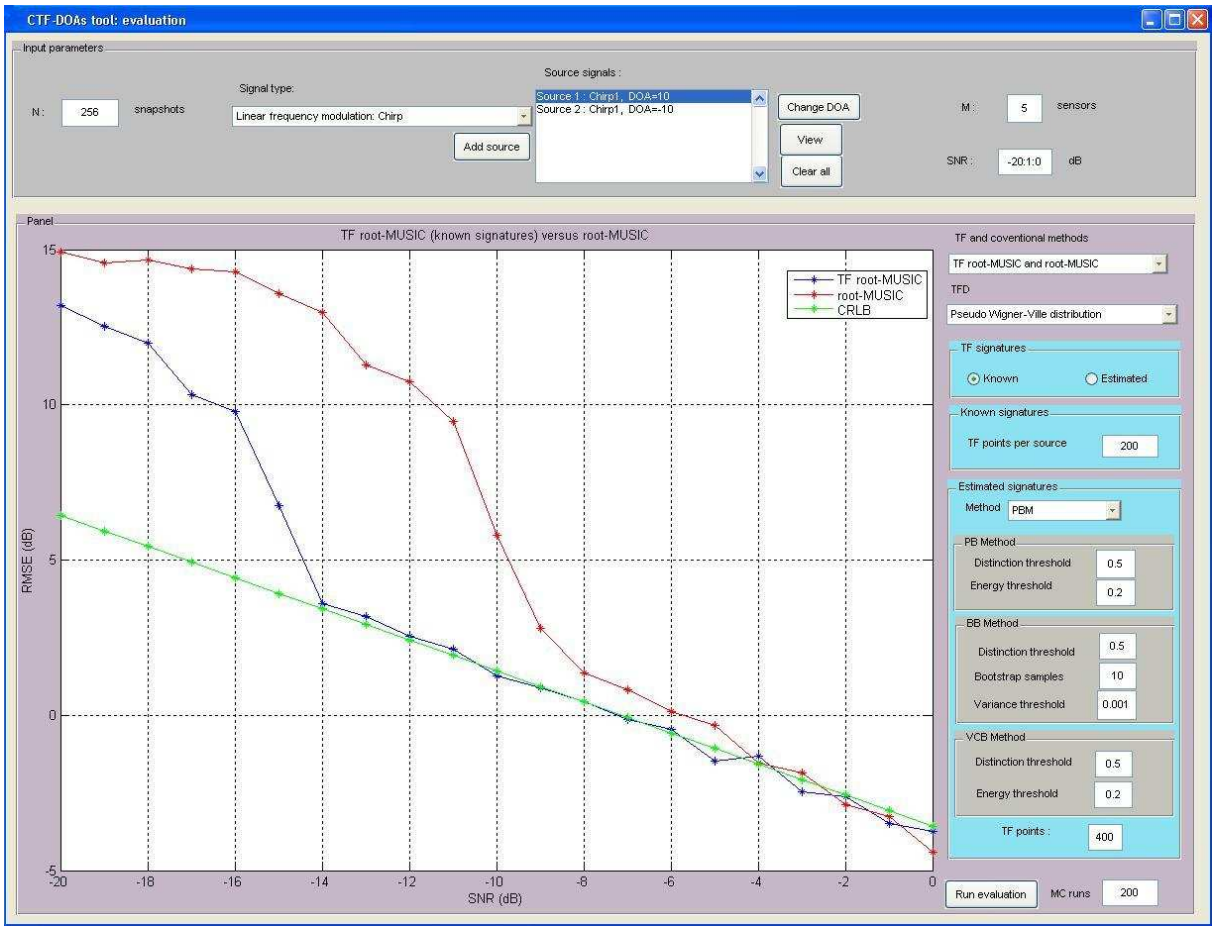

Figure 5.4: The layout of evaluation module

General conclusions and perspectives

General conclusions

The introduction of the time-frequency concept to the problem of DOAs estimation has improved the performance of the conventional methods such as beamforming, subspace, subspace fitting and maximum likelihood. The quantitative comparison done demonstrated that the time-frequency methods have better performance, in terms of both location accuracy and resolution, than the conventional methods. For example, we obtained an improvement of roughly $12dB$ in the location accuracy when we introduced the time-frequency concept to the MUSIC algorithm. However, we demonstrated that the application of the time-frequency analysis is only interesting for some parameter range (e.g. the number of sensors and SNR). Out of this parameter range, the conventional and time-frequency methods tend to have the same performance. In this case, the conventional methods are preferred as they have the lowest computational load.

We also compared the two methods of auto- and cross-terms integration, namely the TFA and JBD. The JBD method is the best for the integration of auto-terms as well as cross-terms, and its performance does not depend on the type of the selected (t, f) points (auto-terms or cross-terms regions). Nonetheless, we should mention that the execution time of JBD is much higher than that of the TFA. An improvement of approximatively $2dB$ in the location accuracy was obtained when we considered only the (t, f) points which belong to the signature of one specific signal.

Concerning the detection of auto- and cross-terms in the time-frequency domain, the bootstrap based method provides better performance than the methods based on projection or vector clustering in the detection of auto-terms and cross-terms. However, in the case of auto-terms detection the three methods tend to have similar performance when the number of sensors or the SNR increases. In such scenario, the two other methods are preferred since they are faster. Although the method based on vector clustering has the worst performance in the detection of cross-terms, it can be successfully employed for the separation of signal signatures which improves the performance of TF DOAs estimation methods and allows solving the underdetermined systems. We found that we can achieve similar performance to the optimal case of known TF signatures when we use the auto-terms detection methods.

Further work

This work has several perspectives. We can mention the derivation of analytic expressions which give the location accuracy and probability of resolution in the case of auto- and cross-terms for both the TFA and JBD methods. The variation of these two performance indices with respect to some parameters such

as the SNR, the number of sensors, the number of snapshots and the nature of the sources, would allow the prediction of the behavior of the TF estimators in a given scenario in order to compare them with the conventional estimators. A derivation of a analytic expression for the Cramer-Rao bound in the case of nonstationary signals is also interesting as it allows the determination of the limit that we can achieve. With regard to the detection of auto- and cross-terms, we can use the estimators of instantaneous frequency as auto-terms estimators in the time-frequency domain. The problem of auto- and cross-terms detection in the time-frequency plan can also be approached using image processing by considering the signatures of signals in the time-frequency plan as objects in image. The approach would avoid the false detection of isolated (t, f) points as auto- or cross-terms.

1 Introduction

L'estimation des directions d'arrivée (**D**irections **O**f **A**rrival) d'une onde plane (ou plusieurs ondes planes) est l'un des problèmes centrales du traitement de signal moderne. Cette estimation trouve son application dans plusieurs domaines tels que le radar, les communications mobiles exploitant la diversité spatiale, le sonar, le sismique, la surveillance électronique, le traitement et diagnostique médicales ainsi que la radio astronomie.

Les méthodes conventionnelles telles que la formation de voies (Beamforming), les méthodes de haute résolution (subspace methods), maximum de vraisemblance et les méthodes subspace fitting reposent toutes sur l'hypothèse de stationnarité des signaux émis par les sources. Cependant, dans la pratique la plupart de ces signaux sont non stationnaires. Dans le cas non stationnaire, ces méthodes peuvent être appliquées mais leurs performances se dégradent.

L'une des solutions à ce problème est l'utilisation des outils d'analyse temps-fréquence. Les distributions temps-fréquence quadratiques ont été initialement introduites au traitement d'antennes par A. Belouchrani et M. Amin pour l'analyse des signaux non stationnaires. Ces distributions ont été utilisées pour la séparation aveugle de sources [4]. En suite pour l'estimation des DOAs des sources non stationnaires en conjonction avec la bloc-diagonalisation conjointe [3]. Après, elles ont été largement exploitées pour l'analyse et la synthèse des signaux non stationnaires [7, 11].

L'étalement du bruit et la localisation des sources dans le domaine temps-fréquence permettent l'amélioration des performances des méthodes d'estimation des DOAs et de leur robustesse contre le bruit.

L'application des distributions quadratiques temps-fréquence au problème d'estimation des DOAs des sources non stationnaires est le sujet principal de ce mémoire de Magister.

On commence ce résumé de mémoire en rappelant la notion de non stationnarité, le modèle utilisé pour l'estimation, ainsi que les méthodes d'estimation conventionnelles basées sur les statistiques d'ordre deux. Ensuite, on introduira le concept temps-fréquence en décrivant les différentes distributions temps-fréquence et leurs propriétés intéressantes tout en mettant l'accent sur leur apport dans l'analyse des signaux non stationnaires. Après, on présentera les distributions temps-fréquence spatiales, les méthodes d'estimation des DOAs basées sur ces distributions ainsi que les méthodes de détection des auto- et cross-termes dans le domaine temps-fréquence. La dernière partie sera consacrée aux résultats d'évaluation des performances des algorithmes présentés.

1.1 Signaux non stationnaires

Un signal déterministe est dit stationnaire si l'on peut l'écrire comme une somme discrète de sinusoïdes :

$$x(t) = \sum_{k \in \mathbf{N}} A_k \cos[2\pi w_k t + \phi_k] \texttt{ pour un signal réel} \tag{1}$$

$$x(t) = \sum_{k \in \mathbf{N}} A_k \exp[j(2\pi w_k t + \phi_k)] \texttt{ pour un signal complexe} \tag{2}$$

Dans le cas aléatoire, le signal $x(t)$ est dit stationnaire au sense large si son espérance est indépendante du temps et sa fonction d'autocorrélation définie comme suit :

$$\mathcal{R}(t,\tau) = E\{x(t+\frac{\tau}{2})x^*(t-\frac{\tau}{2})\} \tag{3}$$

dépend seulement de la différence $(t_1 - t_2)$, où $t_1 = t + \tau/2$ et $t_2 = t - \tau/2$.
Alors un signal est dit non stationnaire si l'une des hypothèses fondamentales est non vérifiée. Les signaux non stationnaires peuvent être trouvés dans plusieurs domaines, entre autres le radar, le sonar, la physique astronomique, le sismique, l'analyse des vibrations, les systèmes de communications, la parole et traitement des signaux biologiques. La plupart des signaux non stationnaires peuvent être exprimés d'une manière générale comme un signal analytique complexe :

$$z(t) = a_0 \exp\{j\varphi(t)\} \tag{4}$$

avec a_0 et $\varphi(t)$, $t \in [T_1, T_2], T_1, T_2 < \infty$, sont l'amplitude et la phase du signal, respectivement.

La phase $\varphi(t)$ du signal $z(t)$ peut être écrite sous la forme

$$z(t) = a_0 \exp\{j \sum_{q=0}^{Q} b_q \psi_{t,q}\} \tag{5}$$

où $b_q, q = 0, ..., Q$, sont des paramètres réels inconnus, et $\psi_{t,q}$ est un ensemble de séquence de base arbitraire.

Dans le cas spéciale où $\psi_{t,q} = t^q$, $z(t)$ est dit signal à phase polynomial. Le signal à modulation linéaire de fréquence (chirp) obtenu pour $Q = 2$ et le signal à modulation quadratique de fréquence obtenu pour $Q = 3$ sont des exemples de ces signaux non stationnaires.

Dans ce mémoire de Magister, on utilise principalement les signaux chirp et les signaux à modulation quadratique de phase pour modéliser les signaux non stationnaires.

1.2 Modèle et hypothèses

On suppose que les L signaux à bande étroite dont les DOAs doivent être estimées ont la même fréquence centrale f_c et sont reçus comme des ondes planes par un réseau linéaire d'antennes (**U**niform **L**inear **A**rray) ayant M éléments espacés par une distance égale à la moitié de la longueur d'onde $(d = \lambda/2)$. Le milieu de propagation est supposé linéaire ; ce qui implique la validation du principe de superposition.

Le signal reçu par le deuxième élément du réseau est retardé par un retard $\tau = \frac{d}{c} sin(\theta)$ (voir Fig. 1), où c est la vitesse de propagation dans le milieu considéré.

Si τ est petit devant l'inverse de la bande passante de $s(t)$, alors

$$x_2(t) = s_\tau(t) = s(t)e^{-j2\pi f_c \tau} = s(t)e^{-j2\pi f_c \frac{d}{c} sin(\theta)} \tag{6}$$

Si tous les retards sont petits devant l'inverse de la bande passante de $s(t)$, i.e.

$$(M-1)\frac{d}{\lambda} sin(\theta) \ll \frac{f_c}{W}$$

Le signal reçu par le k^{ieme} élément peut être écrit sous la forme :

$$x_k(t) = s_{(k-1)\tau}(t) = s(t)e^{-j2\pi f_c (k-1)\tau} = s(t)e^{-j2\pi f_c (k-1)\frac{d}{c}}$$

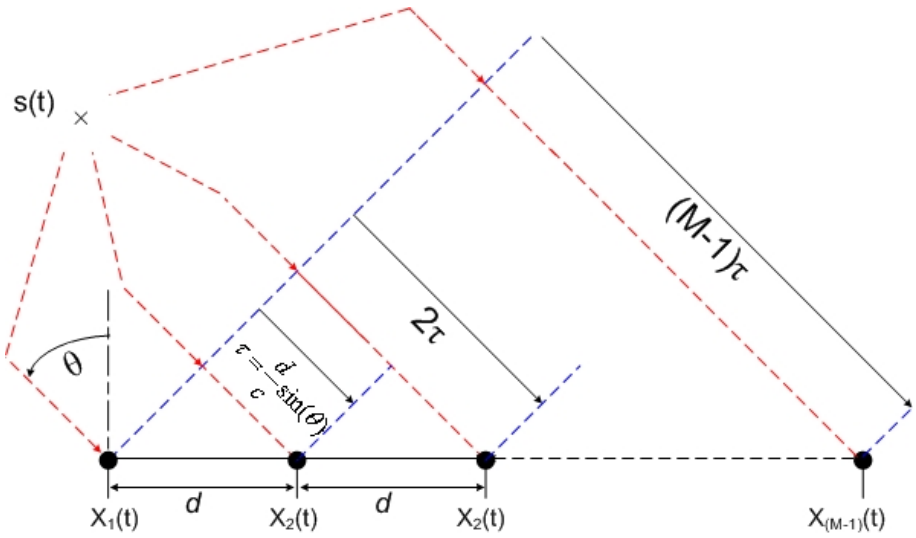

FIG. 1 – Le modèle utilisé pour l'estimation des DOAs

Les signaux reçus $x_1(t), x_2(t), \cdots, x_M(t)$ regroupés dans un vecteur $\mathbf{x}(t)$ donné par :

$$\mathbf{x}(t) = \begin{bmatrix} x_1(t) \\ x_2(t) \\ \vdots \\ x_M(t) \end{bmatrix} = \begin{bmatrix} 1 \\ e^{-j\phi} \\ \vdots \\ e^{-j(M-1)\phi} \end{bmatrix} a(\theta)s(t) = \mathbf{a}(\theta)s(t) \tag{7}$$

où $\phi = 2\pi\frac{d}{\lambda}sin(\theta)$ est l'angle électrique, $\mathbf{a}(\theta)$ est le vecteur de direction, et $\mathbf{x}(t)$ est appelé *snapshot*.

Dans le cas de plus d'une source, le modèle prend la forme suivante :

$$\mathbf{x}(t) = \mathbf{a}(\theta_1)s_1(t) + \mathbf{a}(\theta_2)s_2(t) + \cdots + \mathbf{a}(\theta_L)s_L(t) \tag{8}$$

$$= [\mathbf{a}(\theta_1)\mathbf{a}(\theta_2)\cdots\mathbf{a}(\theta_L)] \begin{bmatrix} s_1(t) \\ s_2(t) \\ \vdots \\ s_L(t) \end{bmatrix} = \mathbf{A}(\theta)\mathbf{s}(t) \tag{9}$$

avec

$$\mathbf{A}(\theta) = [\mathbf{a}(\theta_1)\mathbf{a}(\theta_2)\cdots\mathbf{a}(\theta_L)] \tag{10}$$

$$\theta = [\theta_1\theta_2\cdots\theta_L] \tag{11}$$

$$\mathbf{s}(t) = [s_1(t)s_2(t)\cdots s_L(t)]^T \tag{12}$$

En présence du bruit additif $\mathbf{n}(t)$, on obtient le modèle suivant :

$$\mathbf{x}(t) = \mathbf{A}(\theta)\mathbf{s}(t) + \mathbf{n}(t) \tag{13}$$

On suppose que le bruit est un processus temporellement et spatialement blanc à moyenne nulle, i.e.

$$E\{\mathbf{n}(t)\mathbf{n}^H(s)\} = \sigma_n^2\mathbf{I}_M\delta_{t,s}$$

2 Estimation des directions d'arrivée

Les méthodes décrites sont les méthodes de formation de voies, sous espace, maximum de vraisemblance et subspace fitting.

2.1 Technique de formation de voies

L'idée est de diriger la réponse du réseau d'antennes dans une direction donnée et mesurer la puissance reçue. Les directions qui donnent le maximum d'énergie correspondent aux DOAs. La réponse du réseau est dirigée en formant une combinaison linéaire des sorties des éléments du réseau.

$$\mathbf{y}(t) = \sum_{m=0}^{M} w_m^* x_m(t) = \mathbf{w}^H \mathbf{x}(t) \tag{14}$$

La puissance de sortie est mesurée par :

$$P(\mathbf{w}) = \frac{1}{N} \sum_{t=1}^{N} \mid \mathbf{y}(t) \mid^2 = \frac{1}{N} \sum_{t=1}^{N} \mathbf{w}^H \mathbf{x}(t) \mathbf{x}(t)^H \mathbf{w} = \mathbf{w}^H \hat{\mathbf{R}}_{\mathbf{xx}} \mathbf{w} \tag{15}$$

avec

$$\hat{\mathbf{R}}_{\mathbf{xx}} = \frac{1}{N} \sum_{t=1}^{N} \mathbf{x}(t) \mathbf{x}(t)^H \tag{16}$$

Plusieurs formateurs de voies correspondant aux différents choix du vecteur $\mathbf{w}$ existent dans la littérature.

Par exemple, le formateur de voies conventionnel (ou de Bartlett) maximise la puissance de sortie pour une certaine direction θ. Le problème de maximisation de la puissance de sortie peut être formulé comme suit :

$$\max_{\mathbf{w}} E\{\mathbf{w}^H \mathbf{x}(t) \mathbf{x}(t)^H \mathbf{w}\} = \max_{\mathbf{w}} \mathbf{w}^H E\{\mathbf{x}(t) \mathbf{x}(t)^H\} \mathbf{w} \tag{17}$$

$$= \max_{\mathbf{w}} E\{\mid s(t) \mid^2 \mid \mathbf{w}^H \mathbf{a}(\theta) \mid^2 + \sigma_n^2 \mid \mathbf{w} \mid^2\} \tag{18}$$

La maximisation de cette équation permet d'obtenir la solution suivante :

$$\mathbf{w}_{BF} = \frac{\mathbf{a}(\theta)}{\sqrt{\mathbf{a}^H(\theta) \mathbf{a}(\theta)}} \tag{19}$$

Dans ce cas, le spectre spatial classique est donné par :

$$P_{BF}(\theta) = \frac{\mathbf{a}^H(\theta) \hat{\mathbf{R}}_{\mathbf{xx}} \mathbf{a}(\theta)}{\mathbf{a}^H(\theta) \mathbf{a}(\theta)} \tag{20}$$

Le formateur de voies de Capon est un autre exemple. Pour ce formateur de voies, le problème d'optimisation est posé comme suit :

$$\min_{\mathbf{w}} P(\mathbf{w}) \qquad \textit{avec} \qquad \mathbf{w}^H \mathbf{a}(\theta) = 1 \tag{21}$$

où $P(\mathbf{w})$ est défini dans Eq. 15. Le vecteur $\mathbf{w}$ est donné par :

$$\mathbf{w}_{CAP} = \frac{\hat{\mathbf{R}}_{\mathbf{xx}}^{-1}\mathbf{a}(\theta)}{\mathbf{a}^H(\theta)\hat{\mathbf{R}}_{\mathbf{xx}}^{-1}\mathbf{a}(\theta)} \tag{22}$$

En insérant ce vecteur dans Eq. 15, on obtient le spectre spatial suivant :

$$P_{CAP}(\theta) = \frac{1}{\mathbf{a}^H(\theta)\hat{\mathbf{R}}_{\mathbf{xx}}^{-1}\mathbf{a}(\theta)} \tag{23}$$

Les formateurs de voies ne sont pas de très bons estimateurs des DOAs spécialement pour les signaux non stationnaires. Néanmoins, ils peuvent être utilisés pour indiquer le nombre des signaux présents ainsi que leurs DOAs et puissances approximatives.

2.2 Méthodes sous espace

Les méthodes sous espace exploitent la décomposition en valeurs propres de la matrice de covariance spatiale donnée par :

$$\mathbf{R}_{\mathbf{xx}} = E\{\mathbf{x}(t)\mathbf{x}^H(t)\} = \mathbf{A}(\theta)\mathbf{R}_{\mathbf{ss}}\mathbf{A}^H(\theta) + \mathbf{R}_{\mathbf{nn}} \tag{24}$$

Les vecteurs propres de $\mathbf{R}_{\mathbf{xx}}$ sont les mêmes que ceux de $\mathbf{A}\mathbf{R}_{\mathbf{ss}}\mathbf{A}^H$, et ses valeurs propres sont $\lambda_i = \alpha_i + \sigma_n^2$ pour $1 \leq i \leq L$ et $\lambda_i = \sigma_n^2$ pour $L+1 \leq i \leq M$. Les vecteurs propres peuvent être partitionnés en deux ensembles : $\mathbf{E}_s \triangleq [\mathbf{e}_1, \mathbf{e}_2, ..., \mathbf{e}_L]$ qui forme *le sous espace signal*, alors que $\mathbf{E}_n \triangleq [\mathbf{e}_{L+1}, \mathbf{e}_{L+2}, ..., \mathbf{e}_M]$ forme *le sous espace bruit*. Ces deux sous espaces sont orthogonaux. La matrice des valeurs propres du sous espace signal est $\Lambda_s = diag\{\lambda_1, \lambda_2, ..., \lambda_L\}$. La matrice des valeurs propres de sous espace bruit est $\Lambda_n = diag\{\lambda_{L+1}, \lambda_{L+2}, ..., \lambda_M\}$. Alors, on peut écrire :

$$\mathbf{R}_{\mathbf{xx}} = \mathbf{E}\Lambda\mathbf{E}^H = \mathbf{E}_s\Lambda_s\mathbf{E}_s^H + \mathbf{E}_n\Lambda_n\mathbf{E}_n^H = \mathbf{E}_s\Lambda_s\mathbf{E}_s^H + \sigma_n^2\mathbf{E}_n\mathbf{E}_n^H \tag{25}$$

où $\mathbf{E} \triangleq [\mathbf{e}_1, \mathbf{e}_2, ..., \mathbf{e}_M]$ et $\Lambda = diag\{\lambda_1, \lambda_2, ..., \lambda_M\}$. Puisque les vecteurs propres qui correspondent aux valeurs propres nulles satisfont $\mathbf{A}\mathbf{R}_{\mathbf{ss}}\mathbf{A}^H\mathbf{e}_i = 0$ pour $L+1 \leq i \leq M$; alors, $\mathbf{A}^H\mathbf{e}_i = 0$ pour $L+1 \leq i \leq M$ à condition que $\mathbf{A}$ et $\mathbf{R}_{\mathbf{ss}}$ soient de rang plein.

La dernière propriété implique que les vecteurs des directions sont orthogonaux aux vecteurs propres du sous espace bruit. A cause de l'orthogonalité entre les sous espaces bruit et signal, les vecteurs propres du sous espace signal et les vecteurs des directions d'arrivée engendrent le même sous espace.

2.2.1 MUSIC

Puisque les vecteurs propres en $\mathbf{E}_n$ sont orthogonaux à $\mathbf{A}(\theta)$, on a pour $\theta \in \{\theta_1, \theta_2, ..., \theta_L\}$

$$\mathbf{E}_n^H\mathbf{a}(\theta) = 0 \tag{26}$$

Il y a deux versions de l'algorithme MUSIC : MUSIC spectral et root-MUSIC.

L'algorithme MUSIC spectral consiste alors à chercher les maximums du spectre MUSIC suivant :

$$\mathbf{P}_{MU}(\theta) = \frac{1}{\mathbf{a}^H(\theta)\mathbf{E}_n\mathbf{E}_n^H\mathbf{a}(\theta)} = \frac{1}{\|\mathbf{E}_n^H\mathbf{a}(\theta)\|^2} \tag{27}$$

On résume l'algorithme root-MUSIC comme suit :

1. Estimer la matrice de corrélation en utilisant Eq. 16.
2. Diviser $\hat{\mathbf{E}}$ pour obtenir $\hat{\mathbf{E}}_n$.
3. Former le polynôme $Q_{MU}(z)$ défini comme suit :

$$Q_{MU}(z) = z^{M-1}\mathbf{p}^T(z^{-1})\hat{\mathbf{E}}_n\hat{\mathbf{E}}_n^H\mathbf{p}(z) \tag{28}$$

avec

$$\mathbf{p}(z) = [1, z, z^2, ..., z^{M-1}]^T \tag{29}$$

4. Trouver les racines du polynôme $Q_{MU}(z)$.
5. A partir des $(M-1)$ racines de $Q_{MU}(z)$ qui se trouvent à l'intérieur du cercle unité, choisir les L racines les plus proches du cercle unité $(z_k, k = 1, 2, ..., L)$.
6. Obtenir les directions d'arrivée en utilisant la formule suivante :

$$\theta_k = -\arcsin\{\frac{\angle z_k}{2\pi\frac{d}{\lambda}}\} \tag{30}$$

2.2.2 Min-Norm

Cet algorithme identifie un seul vecteur dans le sous espace bruit (vecteur de prediction $\mathbf{b}$ avec une norme minimale et premier élément unitaire). Si le sous espace bruit est partitionné comme suit :

$$\mathbf{E}_n = \begin{pmatrix} \mathbf{c}^H \\ --- \\ \mathbf{E}_n^{'} \end{pmatrix} \tag{31}$$

où $\mathbf{c}^H$ est la première ligne et $\mathbf{E}_n^{'}$ est le reste des lignes de $\mathbf{E}_n$, alors le vecteur de prédiction peut être exprimé de la manière suivante :

$$\mathbf{b} = \mathbf{E}_n\frac{\mathbf{c}}{\|\mathbf{c}\|^2} \triangleq \mathbf{E}_n\overline{\mathbf{c}} \tag{32}$$

Pour trouver les DOAs, on a besoin de chercher les L maximums en variant θ du spectre spatial suivant :

$$\mathbf{P}_{MN}(\theta) = \frac{1}{|\mathbf{a}^H(\theta)\hat{\mathbf{b}}|^2} \tag{33}$$

Un algorithme root-Min-Norm peut être aussi défini. L'orthogonalité est obtenue en mettant le polynôme suivant égal à zero.

$$Q_{MN}(z) = \mathbf{p}^T(z^{-1})\mathbf{b} = \sum_{k=1}^{M} b_k z^{-k+1} \tag{34}$$

où $\mathbf{p}(z)$ est défini dans Eq. 29. Les DOAs sont alors obtenues en applicant Eq. 30 sur les L racines les plus proches du cercle unité.

2.2.3 ESPRIT

Deux sous matrices $\mathbf{A}_1$ et $\mathbf{A}_2$ sont formées en éliminant les m premières et les m dernières lignes de $\mathbf{A}$ respectivement, i.e.,

$$\mathbf{A} = \begin{bmatrix} \mathbf{A}_1 \\ m \text{ première lignes} \end{bmatrix} = \begin{bmatrix} m \text{ dernières lignes} \\ \mathbf{A}_2 \end{bmatrix} \tag{35}$$

Pour un ULA, la matrice des directions prend une forme spéciale (matrice de Vandermonde)

$$\mathbf{A}(\theta) = \begin{pmatrix} 1 & 1 & \cdots & 1 \\ e^{-j\phi_1} & e^{-j\phi_2} & \cdots & e^{-j\phi_L} \\ \vdots & \vdots & & \vdots \\ e^{-j(M-1)\phi_1} & e^{-j(M-1)\phi_2} & \cdots & e^{-j(M-1)\phi_L} \end{pmatrix}, \phi_k = 2\pi\frac{d}{\lambda}\sin(\theta_k) \tag{36}$$

Les matrices $\mathbf{A}_1$ et $\mathbf{A}_2$ sont reliées par la formule :

$$\mathbf{A}_2 = \mathbf{A}_1\Phi \tag{37}$$

où Φ est une matrice diagonale ayant les racines $e^{-jm\phi_k}$,$k = 1, 2, ..., L$, dans sa diagonale. L'estimation des DOAs correspond à l'estimation de Φ. Si $\mathbf{E}_{1s}$ et $\mathbf{E}_{2s}$ sont deux matrices de dimension $(M - m) \times L$ ayant comme colonnes les L vecteurs propres qui correspondent aux plus grandes valeurs propres des matrices de corrélation $\mathbf{R}_1$ et $\mathbf{R}_2$ respectivement, il existe une matrice Ψ telle que :

$$\mathbf{E}_{1s}\Psi = \mathbf{E}_{2s} \tag{38}$$

On a aussi

$$\mathbf{T}\Psi\mathbf{T}^{-1} = \Phi \tag{39}$$

Puisque les matrices Ψ et Φ sont reliées par une transformation de similarité alors ils ont les mêmes valeurs propres. Ces valeurs propres sont données par $e^{-jm\phi_k}$,$k = 1, 2, ..., L$.

La solution de Eq. 38 en utilisant la version Least-Square est donnée par :

$$\hat{\Psi} = \hat{\mathbf{E}}_{s1}^{\dagger}\hat{\mathbf{E}}_{s2} \tag{40}$$

où $\hat{\mathbf{E}}_{s1}^{\dagger} = (\hat{\mathbf{E}}_{s1}^H\hat{\mathbf{E}}_{s1})^{-1}\hat{\mathbf{E}}_{s1}^H$ est la pseudo-inverse de $\hat{\mathbf{E}}_{s1}$.

La version Total Least-Square (TLS) de l'algorithme ESPRIT peut être résumée comme suit :

1. Former les matrices $\hat{\mathbf{E}}_{1s}$ et $\hat{\mathbf{E}}_{2s}$
2. Former la matrice

$$\mathbf{B} = \begin{bmatrix} \hat{\mathbf{E}}_{s1}^H \\ \hat{\mathbf{E}}_{s2}^H \end{bmatrix} \begin{bmatrix} \hat{\mathbf{E}}_{s1} & \hat{\mathbf{E}}_{s2} \end{bmatrix} \tag{41}$$

et réaliser sa décomposition spectrale

$$\mathbf{B} = \mathbf{V}\Lambda\mathbf{V}^H \tag{42}$$

où Λ est une matrice contenant les valeurs propres de $\mathbf{B}$ dans sa diagonale, et les colonnes de $\mathbf{V}$ sont les vecteurs propres de $\mathbf{B}$.

3. Diviser $\mathbf{V}$ en quatre matrices de dimension $L \times L$ comme suit :

$$\mathbf{V} = \begin{pmatrix} \mathbf{V}_{11} & \mathbf{V}_{12} \\ \mathbf{V}_{21} & \mathbf{V}_{22} \end{pmatrix} \tag{43}$$

4. Calculer les valeurs propres β_k,$k = 1, 2, ..., L$ de la matrice $-\mathbf{V}_{11}\mathbf{V}_{22}^{-1}$
5. Estimer les DOAs θ_k,$k = 1, 2, ..., L$ en utilisant :

$$\theta_k = -\arcsin(\frac{\angle\beta_k}{2m\pi\frac{d}{\lambda}}) \tag{44}$$

2.3 Maximum de vraisemblance

L'estimateur déterministe de maximum de vraisemblance est obtenu en résolvant le problème d'optimisation suivant :

$$\hat{\theta}_{DML} = \arg\min_{\theta}\{Tr\{\Pi_{\mathbf{A}}^{\perp}\hat{\mathbf{R}}_{\mathbf{xx}}\}\} = \arg\min_{\theta}\{f_{DML}(\theta)\} \tag{45}$$

avec

$$\mathbf{A}^{\dagger} = (\mathbf{A}^H\mathbf{A})^{-1}\mathbf{A}^H \tag{46}$$

$$\Pi_{\mathbf{A}} = \mathbf{A}\mathbf{A}^{\dagger} \tag{47}$$

$$\Pi_{\mathbf{A}}^{\perp} = \mathbf{I} - \Pi_{\mathbf{A}} \tag{48}$$

Pour calculer les estimateurs de maximum de vraisemblance, une optimisation non linéaire de L-dimension doit se faire numériquement. Cependant, la convergence des méthodes numériques vers un minimum global n'est pas garantie car elle dépend de la valeur initiale.

2.4 Subspace fitting

Les méthodes de subspace fitting ont les mêmes performances statistiques que les méthodes de maximum de vraisemblance. Cependant, le coût de calcul de ces méthodes est inférieur à celui des méthodes de maximum de vraisemblance.

L'estimateur de *signal subspace fitting* est obtenu en résolvant le problème d'optimisation non linéaire suivant :

$$\hat{\theta} = \arg\min_{\theta}\{Tr\{\Pi_{\mathbf{A}}^{\perp}\hat{\mathbf{E}}_s\hat{\Lambda}_s\hat{\mathbf{E}}_s^H\}\} \tag{49}$$

Une pondération des vecteurs propres peut être introduite

$$\hat{\theta}_{SSF} = \arg\min_{\theta}\{Tr\{\Pi_{\mathbf{A}}^{\perp}\hat{\mathbf{E}}_s\mathbf{W}\hat{\mathbf{E}}_s^H\}\} \tag{50}$$

Le choix optimal de $\mathbf{W}$ est donné par :

$$\mathbf{W}_{opt} = (\Lambda_s - \sigma_n^2\mathbf{I})^2\Lambda_s^{-1} \tag{51}$$

Puisque $\mathbf{W}_{opt}$ dépend des paramètres inconnus, on utilise alors :

$$\hat{\mathbf{W}}_{opt} = (\hat{\Lambda}_s - \hat{\sigma}_n^2\mathbf{I})^2\hat{\Lambda}_s^{-1} \tag{52}$$

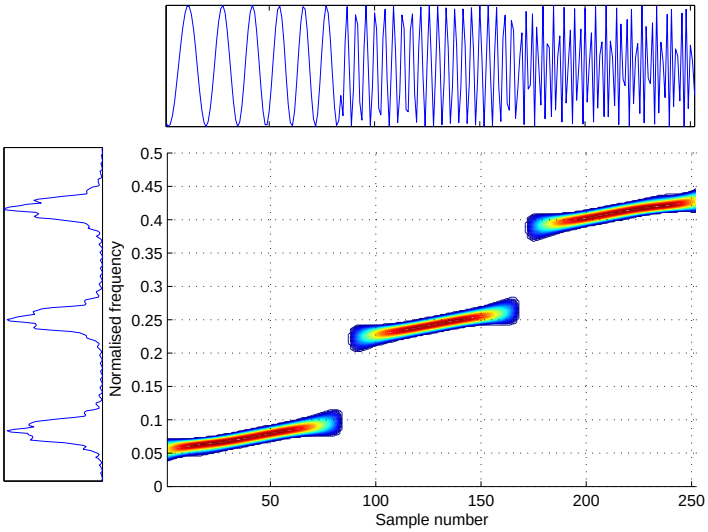

FIG. 2 – Représentation temps-fréquence d'un signal à trois composantes

L'estimateur défini par Eq. 50 avec les poids donnés par Eq. 52 est nommé estimateur de *Weighted Subspace Fitting* (WSF) :

$$\hat{\theta}_{WSF} = \arg\min_{\theta}\{Tr\{\Pi^{\perp}_{\mathbf{A}}\hat{\mathbf{E}}_s\mathbf{W}_{opt}\hat{\mathbf{E}}_s^H\}\} \tag{53}$$

3 Distributions temps-fréquence

Les distributions temps-fréquence (**T**ime-**F**requency **D**istributions) donnent la distribution d'énergie par rapport au temps et fréquence simultanément. Contrairement aux représentations conventionnelles (temporelle ou fréquentielle), ces distributions permettent la connaissance des instants de début et de fin de chaque composante du signal ainsi que la variation temporelle du contenu fréquentiel du signal comme indiqué dans la Fig. 2.

3.1 Distribution de Wigner-Ville

La distribution de Wigner-Ville (**W**igner-**V**ille **D**istribution) d'un signal $z(t)$ est donnée par :

$$W_z(t,f) = \int_{-\infty}^{+\infty} z(t+\tau/2)z^*(t-\tau/2)e^{-j2\pi f\tau}d\tau \tag{54}$$

La WVD est la distribution temps-fréquence de base puisque toutes les autres TFDs s'écrivent comme une distribution de Wigner-Ville filtrée. De plus, la WVD est optimale pour représenter les signaux chirp. Cependant la WVD a quelques limitations. Elle peut donner des grandes valeurs négatives. De plus, puisque la distribution est bilinéaire, elle génère des composantes additionnelles appelées "artifacts". Ces composantes apparaissent entre les vraies composantes dans le cas d'un signal à plusieurs composantes (Outer Artifact) ou un signal à une seule composante non linéaire (Inner Artifact). Fig.

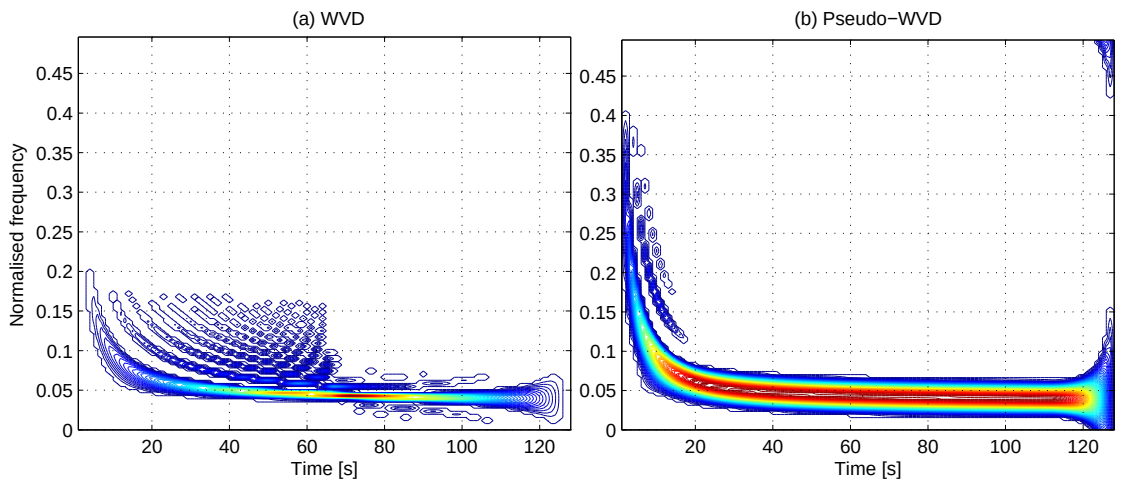

FIG. 3 – La WVD et la Pseudo-WVD d'un signal FM hyperbolique

3(a) donne la WVD d'un signal FM hyperbolique à une seule composante. Le maximum de la WVD est une approximation de la signature du signal mais il y a des composantes additionnelles qui représentent les inner artifacts. Les inner artifacts peuvent être atténués en appliquant la pseudo-WVD (Fig. 3 (b)) mais en réduisant la résolution. Fig. 4 donne la WVD de la somme de deux signaux chirp. Il y a une composante supplémentaire entre les deux chirps correspondant aux outer artifacts. Cette composante peut être atténuée en utilisant les distributions à interférence réduite (**R**educed **I**nterference **D**istributions).

3.2 Distributions temps-fréquence quadratiques

La classe de TFDs quadratiques peut être définie comme étant la classe des distributions obtenues en filtrant la distribution de Wigner-Ville.

Une distribution quadratique $\rho_z(t,f)$ est exprimée comme une double convolution de la WVD de $z(t)$, $W_z(t,f)$, et du noyau temps-fréquence $\gamma(t,f)$.

$$\rho_z(t,f) = W_z(t,f) \star_t \star_f \gamma(t,f) \tag{55}$$

$$= \int_{-\infty}^{+\infty} \int_{-\infty}^{+\infty} W_z(t-t^{'}, f-f^{'}) \gamma(t^{'}, f^{'}) dt^{'} df^{'} \tag{56}$$

Les distributions quadratiques peuvent être aussi exprimées en fonction du noyau Doppler-lag $g(t,\tau)$.

$$\rho_z(t,f) = \int\int\int g(\nu,\tau) z(u+\tau/2) z^*(u-\tau/2) e^{j2\pi(\nu t - \nu u + f\tau)} du d\nu d\tau \tag{57}$$

Le Tableau 1 liste quelques TFDs les plus utilisées ainsi que leurs noyaux exprimés dans les domaines Doppler-retard et temps-retard.

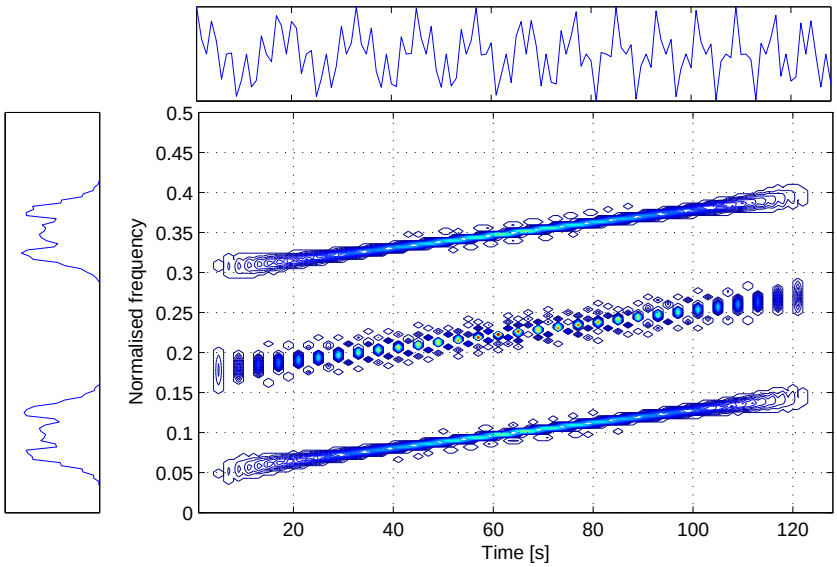

FIG. 4 – La WVD de la somme de deux signaux chirp

Distribution	**noyau Doppler-retard** : $g(\nu,\tau)$	**noyau temps-retard** : $G(t,\tau)$
Wigner-Ville	1	$\delta(t)$
PWV	$h(\tau)$	$\delta(t)h(\tau)$
Spectrogram	$\int_{-\infty}^{+\infty} h(u+\frac{\tau}{2})h^*(u-\frac{\tau}{2})e^{-j2\pi\nu u}du$	$h(t+\tau/2)h^*(t-\tau/2)$
Choi-Williams	$e^{-\nu^2\tau^2/\sigma}$	$\frac{\sqrt{\pi\sigma}}{\lvert\tau\rvert}e^{-\pi^2\sigma t^2/\tau^2}$
Born-Jordan	$sinc(2\alpha\nu\tau)$	$\frac{1}{\lvert 2\alpha\tau\rvert}rect\frac{t}{2\alpha\tau}$
ZAM	$h(\tau)\frac{a}{2\lvert\tau\rvert}sinc\frac{2\nu\tau}{a}$	$h(\tau)rect\frac{t}{2\tau/a}$
B	$\frac{\lvert\tau\rvert^\beta\lvert\Gamma(\beta+j\pi\nu)\rvert^2}{2^{1-2\beta}\Gamma(2\beta)}$	$\lvert\tau\rvert^\beta\cosh^{-2\beta}t$
MB	$\frac{\lvert\Gamma(\beta+j\pi\nu)\rvert^2}{\Gamma^2(\beta)}$	$\frac{\cosh^{-2\beta}t}{\int_{-\infty}^{+\infty}\cosh^{-2\beta}\zeta d\zeta}$
Rihaczek	$e^{-j\pi\nu\tau}$	$\delta(t-\tau/2)$
Page	$e^{-j\pi\nu\lvert\tau\rvert}$	$\delta(t-\lvert\tau/2\rvert)$
Levin	$\cos(\pi\nu\tau)$	$\frac{1}{2}[\delta(t+\tau/2)+\delta(t-\tau/2)]$

Tableau 1 : Quelques TFDs et leurs noyaux

4 Estimation des directions d'arrivée dans le domaine temps-fréquence

L'exploitation de la non stationnarité est faite à travers des distributions temps-fréquence spatiales (**S**patial **T**ime-**F**requency **D**istributions), qui représentent une généralisation des TFDs aux signaux reçus par un réseau d'antennes. Sous un modèle linéaire, les STFDs et la matrice de covariance spatiale ont la même structure spectrale (eigenstructure).

4.1 Distribution temps-fréquence spatiale

La classe quadratique de la matrice de STFD d'un vecteur de signal $\mathbf{x}(t)$ est obtenue à partir de Eq. 57 comme suit :

$$\mathbf{D_{xx}}(t,f) = \int_{-\infty}^{+\infty}\int_{-\infty}^{+\infty}\int_{-\infty}^{+\infty} g(\nu,\tau)\mathbf{x}(u+\tau/2)\mathbf{x}^H(u-\tau/2)e^{j2\pi(\nu t-\nu u-f\tau)}d\nu du d\tau \tag{58}$$

où $g(\nu,\tau)$ est le noyau défini dans le domaine Doppler-retard.

La matrice de cross-terme STFD entre deux vecteurs de signaux $\mathbf{x}_1$ et $\mathbf{x}_2$ est définie par la relation :

$$\mathbf{D_{x_1x_2}}(t,f) = \int_{-\infty}^{+\infty}\int_{-\infty}^{+\infty}\int_{-\infty}^{+\infty} g(\nu,\tau)\mathbf{x}_1(u+\tau/2){\mathbf{x}_2}^H(u-\tau/2)e^{j2\pi(\nu t-\nu u-f\tau)}d\nu du d\tau \tag{59}$$

4.2 Méthodes sous espace temps-fréquence

En appliquant la STFDs au vecteur $\mathbf{x}$ de Eq. 13 on obtient :

$$\tilde{\mathbf{D}}_{\mathbf{xx}}(t,f) = \mathbf{A}\tilde{\mathbf{D}}_{\mathbf{ss}}(t,f)\mathbf{A}^H + \sigma^2\mathbf{I}_M \tag{60}$$

avec

$$\tilde{\mathbf{D}}_{\mathbf{xx}}(t,f) = E\{\mathbf{D_{xx}}(t,f)\} \tag{61}$$

$$\tilde{\mathbf{D}}_{\mathbf{ss}}(t,f) = E\{\mathbf{D_{ss}}(t,f)\} \tag{62}$$

$$\sigma_n^2\mathbf{I}_M = E\{\mathbf{D_{nn}}(t,f)\} \tag{63}$$

Eq. 60 est similaire à l'Eq. 24 ; ceci implique que les méthodes basées sur la décomposition en valeurs propres peuvent être utilisées.

Eq. 60 est vérifiée pour tous les points (t,f). Dans le but de réduire l'effet du bruit et assurer que la matrice STFD est de rang plein, on considère plusieurs points (t,f) ; ceci permet la considération de plus d'information sur les sources. Cette dernière peut être faite selon deux méthodes : bloc-diagonalisation conjoint (**J**oint **B**lock-**D**iagonalisation)[3] et moyenne temps-fréquence (**T**ime-**F**requency **A**veraging)[9].

4.2.1 Bloc-diagonalisation conjointe

Si l'on réalise une décomposition en valeurs singulière de la matrice des directions $\mathbf{A}(\theta)$, on obtient :

$$\mathbf{A}(\theta) = [\mathbf{E}_s \quad \mathbf{E}_n][\mathbf{\Sigma} \quad \mathbf{0}]^T\mathbf{V}^H \tag{64}$$

En insérant cette équation dans Eq. 60 on obtient dans le cas d'absence du bruit :

$$\mathbf{D_{xx}}(t,f) = [\mathbf{E}_s \quad \mathbf{E}_n]\mathbf{B}(t,f)[\mathbf{E}_s \quad \mathbf{E}_n]^H \tag{65}$$

où $\mathbf{B}(t,f)$ est une matrice bloc-diagonale donnée par :

$$\mathbf{B}(t,f) = diag[\mathbf{\Sigma V}^H \mathbf{D_{ss}}(t,f)\mathbf{V\Sigma} \quad \mathbf{0}] \tag{66}$$

Si l'on considère un ensemble de K matrices, $\mathbf{D_{xx}}(t_k,f_k) \in \mathbb{C}^{M\times M}$, $k=1,...,K$, on a la décomposition suivante : pour $k=1,...,K$

$$\mathbf{D_{xx}}(t_k,f_k) = [\mathbf{E}_s \quad \mathbf{E}_n] \begin{bmatrix} \mathbf{A}_k & \mathbf{0} \\ \mathbf{0} & \mathbf{0} \end{bmatrix} \begin{bmatrix} \mathbf{E}_s^H \\ \mathbf{E}_n^H \end{bmatrix} = \mathbf{E}_s \mathbf{A}_k \mathbf{E}_s^H \tag{67}$$

où $\mathbf{E} = [\mathbf{E}_s \quad \mathbf{E}_n]$ est unitaire et $\mathbf{A}_k = \mathbf{\Sigma V}^H \mathbf{D_{ss}}(t_k,f_k)\mathbf{V\Sigma}$ sont des matrices de dimension $L \times L$.

Les matrices $\mathbf{D_{xx}}(t_k,f_k)$ sont conjointement bloc-diagonalisable, i.e. $\mathbf{E}^H\mathbf{D_{xx}}(t_k,f_k)\mathbf{E}$ pour $k=1,...,K$ sont des matrices bloc-diagonales.

Le problème de JBD consiste à estimer les matrices $\mathbf{E}$ (ou $\mathbf{E}_s$) et $\mathbf{A}_k$,$k=1,..,K$ à partir des matrices $\mathbf{D_{xx}}(t_k,f_k)$, $k=1,..,K$.

4.2.2 MUSIC, Min-Norm temps-fréquence

A titre d'exemple, on donne l'algorithme utilisé pour l'implémentation de MUSIC temps-fréquence (TF-MUSIC) pour montrer comment les algorithmes des méthodes sous espace temps-fréquence peuvent être développés. On résume l'algorithme comme suit :

- ÉTAPE 1 : Former K matrices $\mathbf{D_{xx}}(t_k,f_k)$ pour les points sélectionnés (t_k,f_k), $k=1,2,...,K$
- ÉTAPE 2 : Les vecteurs propres de $E\{\mathbf{D_{xx}}(t_k,f_k)\}$ qui correspondent aux plus petites valeurs propres $M-L$, qui forment le sous espace bruit $\mathbf{E}_n = [\mathbf{e}_{L+1}, \mathbf{e}_{L+2}, ..., \mathbf{e}_M]$, sont obtenus par JBD de la STFDs, ou TFA à travers la décomposition en valeurs propres de la matrice moyennée

$$\hat{\mathbf{D}}_{\mathbf{xx}} = \frac{1}{K}\sum_{k=1}^{K} \mathbf{D_{xx}}(t_k,f_k) \tag{68}$$

- ÉTAPE 3 : Estimer les DOAs à partir des maximums du spectre temps-fréquence défini par Eq. 27 pour obtenir l'estimateur MUSIC spectral temps-fréquence (**TF spectral MUSIC**), ou en résolvant le polynôme donné par Eq. 28 pour obtenir l'estimateur root-MUSIC temps-fréquence (**TF-root-MUSIC**).

Fig. 5 et 6 donnent les spectres obtenus pour MUSIC et Min-Norm dans leurs versions conventionnelles et temps-fréquence. L'amélioration apportée par l'application des STFDs est apparente.

4.3 Maximum de vraisemblance temps-fréquence

L'estimateur des DOAs de maximum de vraisemblance temps-fréquence est obtenu en résolvant le problème de minimisation donné dans Eq. 69 [10].

$$\hat{\theta}^{tf} = \arg\min_{\theta}\{Tr\{\Pi_{\mathbf{A}}^{\perp}\hat{\mathbf{D}}_{\mathbf{xx}}\}\} \tag{69}$$

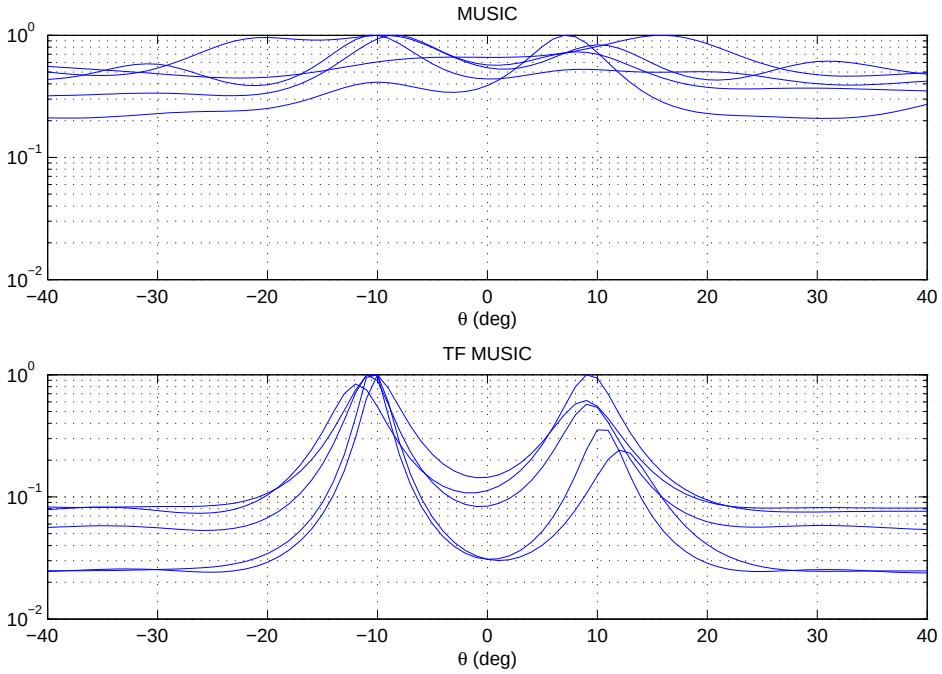

FIG. 5 – Le spectre spatial du MUSIC conventionnel et MUSIC temps-fréquence

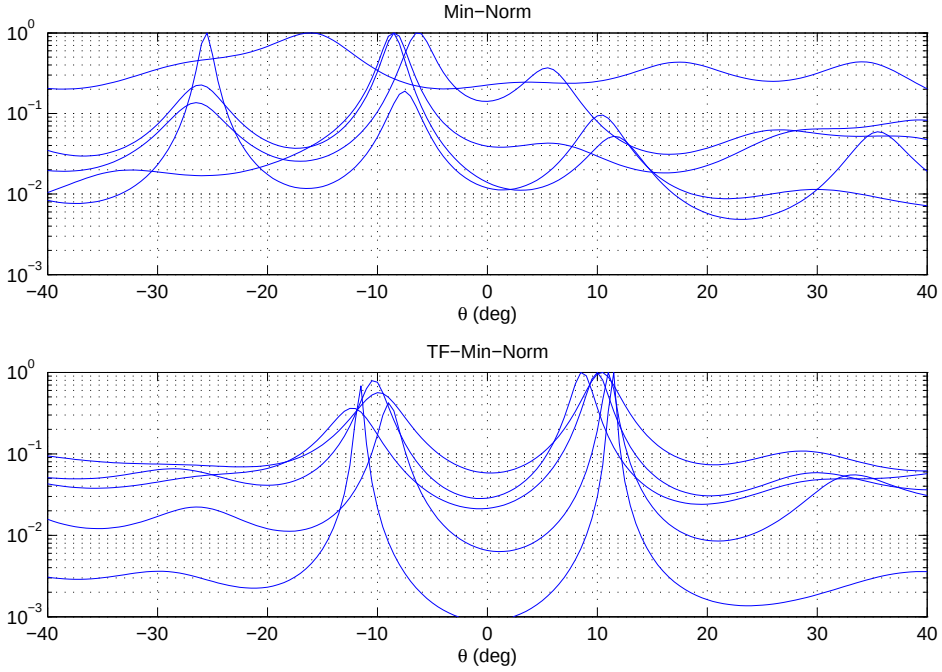

FIG. 6 – Le spectre spatial du Min-Norm conventionnel et Min-Norm temps-fréquence

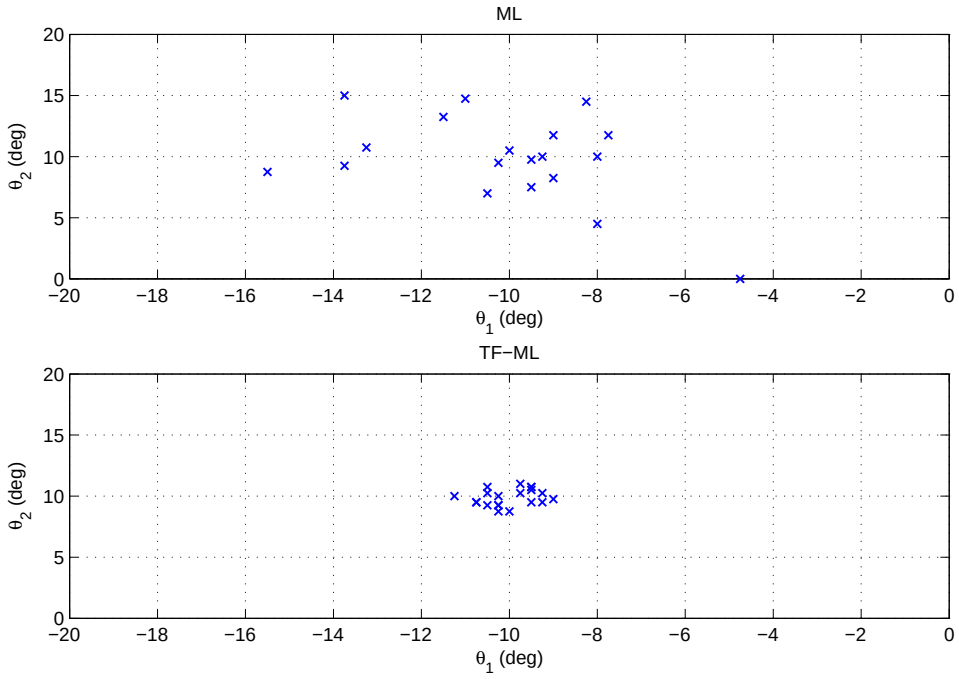

FIG. 7 – (θ_1, θ_2) qui maximisent les fonctions de ML conventionnel et temps-fréquence

Pour montrer l'avantage du maximum de vraisemblance temps-fréquence, Fig. 7 donne (θ_1, θ_2) qui maximisent la valeur des fonctions de maximum de vraisemblance temps-fréquence et conventionnel pour 20 réalisations indépendantes. Il est évident que la version temps-fréquence donne la plus petite variance ; d'où la meilleure performance.

4.4 Subspace fitting temps-fréquence

On obtient l'estimateur de subspace fitting temps-fréquence en remplaçant la matrice $\hat{\mathbf{R}}_{\mathbf{xx}}$ par la matrice $\hat{\mathbf{D}}_{\mathbf{xx}}$ dans les expressions des estimateurs conventionnels [6].

Fig. 8 donne (θ_1, θ_2) qui maximisent la valeur des fonctions de TF-WSF et WSF conventionnel pour 20 réalisations indépendantes. On montre par cet exemple, la supériorité de la version temps-fréquence par rapport à la version conventionnelle.

4.5 Sélection des auto- et cross-termes dans le domaine temps-fréquence

On présente quelques méthodes pour détecter les auto- et cross-termes dans le domaine temps-fréquence.

4.5.1 Méthode basée sur la projection

La méthode basée sur la projection (**P**rojection **B**ased **M**ethod) [2] utilise le critère de sélection suivant :

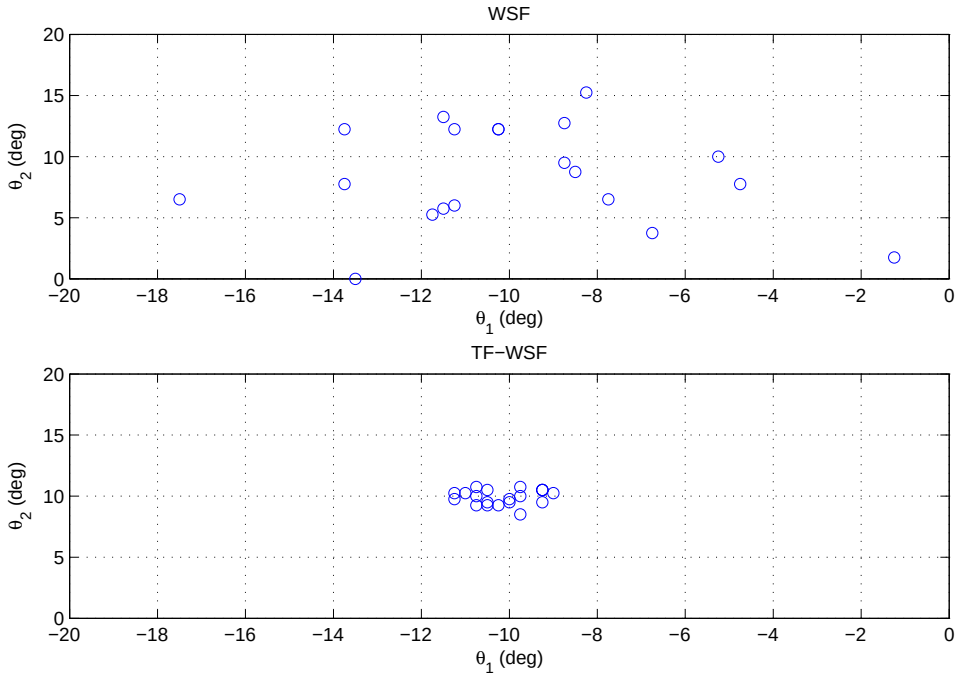

FIG. 8 – (θ_1, θ_2) qui minimisent les fonctions de TF-WSF et WSF conventionel

$$\text{si } \frac{Trace(\mathbf{D_{zz}}(t,f))}{norm(\mathbf{D_{zz}}(t,f))} < \epsilon \rightarrow \text{décider que } (t,f) \text{ est un cross-terme} \tag{70}$$

$$\text{si } \frac{Trace(\mathbf{D_{zz}}(t,f))}{norm(\mathbf{D_{zz}}(t,f))} > \epsilon \rightarrow \text{décider que } (t,f) \text{ est un auto-terme} \tag{71}$$

où ϵ est un scalaire réel positif (typiquement $\epsilon = 0.9$)

avec

$$\mathbf{D_{zz}}(t,f) = \mathbf{W}\mathbf{D_{xx}}(t,f)\mathbf{W}^H \tag{72}$$

où $\mathbf{W}$ est une matrice de blanchiment de dimension $L \times M$ [4] and [8].

4.5.2 Méthode basée sur le vecteur clustering

La méthode basée sur le vecteur clustering (**V**ector **C**lustering **B**ased **M**ethod) a été initialement utilisée pour la séparation des sources [1], on l'a adapté pour le problème d'estimation des directions d'arrivée.

Dans cette approche, on suppose que les sources sont orthogonales dans le domaine temps-fréquence. L'idée générale de cette méthode est de regrouper les points auto-termes associent à la même valeur propre principale. Les DOAs sont alors obtenus en utilisant les points auto-termes appartenant au signal sélectionné. Le diagramme bloc de cet algorithme proposé est donné dans Fig. 9.

Pour la distinction entre les auto- et cross-termes, on utilise le test suivant :

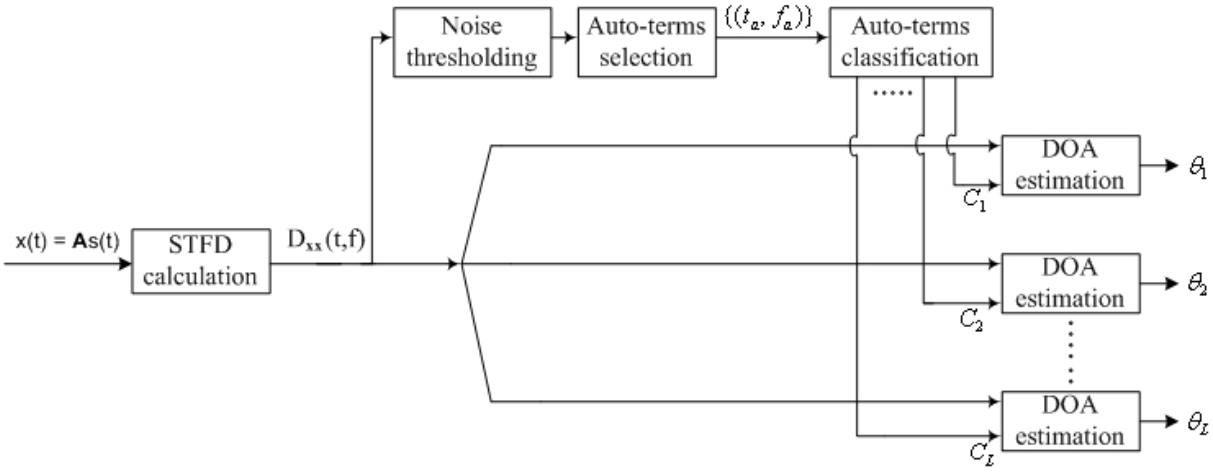

FIG. 9 – Diagramme bloc de l'algorithme

$$\text{si} \quad \left| \frac{\lambda_{max}\{\mathbf{D_{xx}}(t,f)\}}{norm\{\mathbf{D_{xx}}(t,f)\}} - 1 \right| > \epsilon_2 \rightarrow \quad \text{décider que le point } (t,f) \text{ est un cross-terme} \tag{73}$$

où ϵ_2 est un petit scalaire positif (typiquement $\epsilon_2 = 10^{-4}$), et $\lambda_{max}\{\mathbf{D_{xx}}(t,f)\}$ représente la plus grande valeur propre de $\mathbf{D_{xx}}(t,f)$.

4.5.3 Méthode basée sur le bootstrap

La méthode basée sur le bootstrap (**B**ootstrap **B**ased **M**ethod) permet la classification du bruit, auto- et cross-terme [5]. Cette méthode utilise un estimé de la variance du test statistique suivant :

$$T(t,f) = \frac{Trace(\mathbf{D_{zz}}(t,f))}{norm(\mathbf{D_{zz}}(t,f))} \tag{74}$$

Puisque une seule valeur du test statistique est disponible pour un point (t,f) donné, la variance ne peut pas être estimée directement mais elle est estimée en utilisant une technique de ré-échantillonnage (re-sampling) tel que le bootstrap. Après l'estimation de la variance du test statistique, σ_T^2, la procedure illustrée dans Fig. 10 peut être utilisée pour classer automatiquement les points (t,f) dans ces trois classes.

5 Résultats d'évaluation des performances

On évalue les performances des algorithmes temps-fréquence, les deux méthodes d'intégration des auto- et cross-termes ainsi que les méthodes de sélection des auto- et cross-termes.

5.1 Estimation conventionnelle et temps-fréquence des DOAs

Une évaluation des performances des méthodes root-MUSIC, TF-root-MUSIC, root-Min-Nrom et TF-root-Min-Nrom en terme de précision d'estimation et aussi en terme de

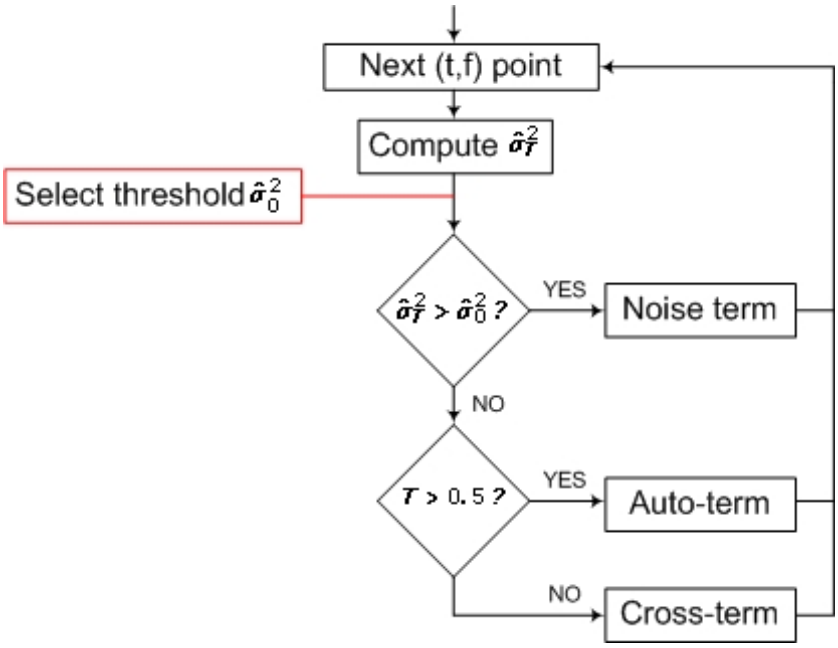

FIG. 10 – Classification automatique des points (t, f)

pouvoir de résolution est faite dans cette partie. Figs. 11 à 18 donnent les résultats qu'on a obtenu. La précision d'estimation est évaluée en utilisant l'erreur quadratique moyenne (**R**oot **M**ean-**S**quared **E**rror) alors que le pouvoir de résolution est mesuré en utilisant la probabilité de résolution. A partir de ces figures, il est claire que les algorithmes temps-fréquence offrent une meilleure performance que les algorithmes conventionnels plus particulièrement lorsque le SNR est faible ou le nombre d'éléments d'antenne est petit. La PWVD permet d'avoir la meilleure précision et résolution par rapport à BJD et CWD.

5.2 Intégration des auto- et cross-termes

L'effet d'intégration des auto- et cross-termes par les méthodes de JBD et TFA est étudié dans cette partie. L'apport obtenu en sélectionnant quelques signaux est aussi mesuré. Figs. 19 à 22 représentent les résultats. La JBD donne la meilleure précision par rapport à TFA dans les trois cas et sa performance est indépendante des régions sélectionnées (régions auto-terme, cross-terme ou les deux). Cependant, la TFA dégrade la performance lorsque des points (t, f) de la région cross-terme sont sélectionnés. La performance peut être améliorée davantage en sélectionnant des points appartenant à un signal particulier comme l'indique Fig. 22.

5.3 Sélection des auto- et cross-termes

On évalue les performances des algorithmes de détection des auto- et cross-termes en utilisant les courbes de probabilité de détection correcte en fonction de la probabilité de fausse alarme (**R**eceiver **O**perating **C**haracteristic). Figs. 23 à 26 donnent les résultats. A partir de ces résultats, on peut conclure que la BBM est la meilleure par rapport aux autres méthodes, plus particulièrement lorsque le SNR est faible. Cependant, cette méthode est la plus coûteuse puisque elle nécessite plus d'opérations de calcul.

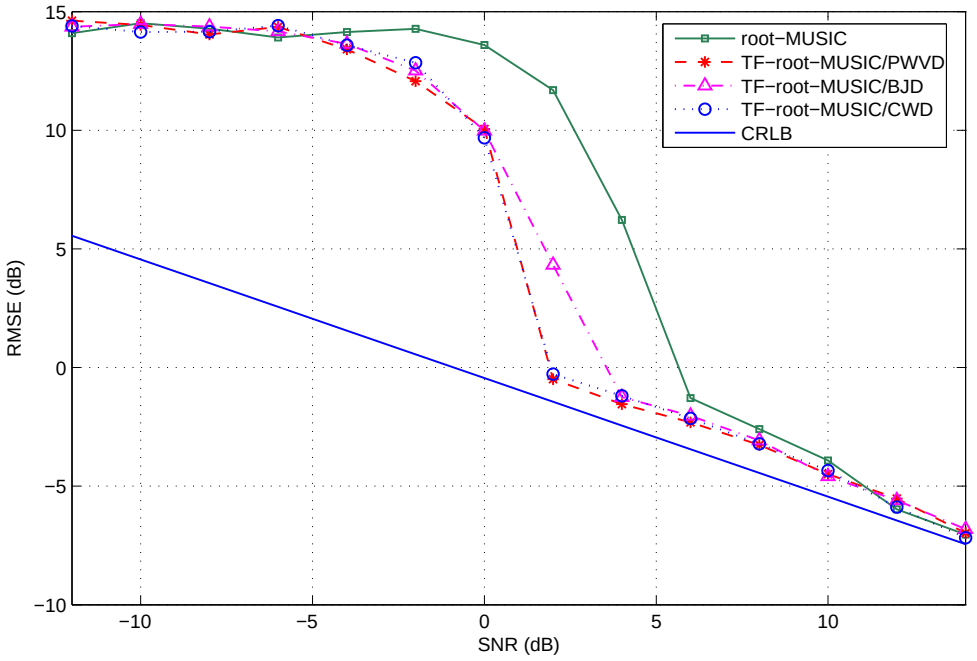

FIG. 11 – Root-MUSIC et TF-root-MUSIC : RMSE en fonction du SNR

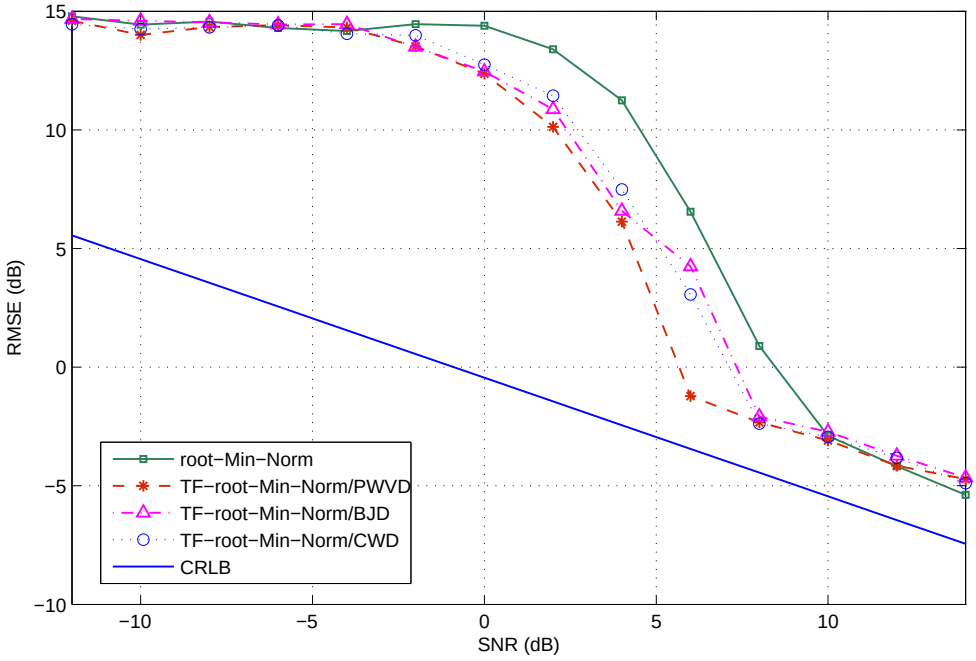

FIG. 12 – Root-Min-Norm et TF-root-Min-Norm : RMSE en fonction du SNR

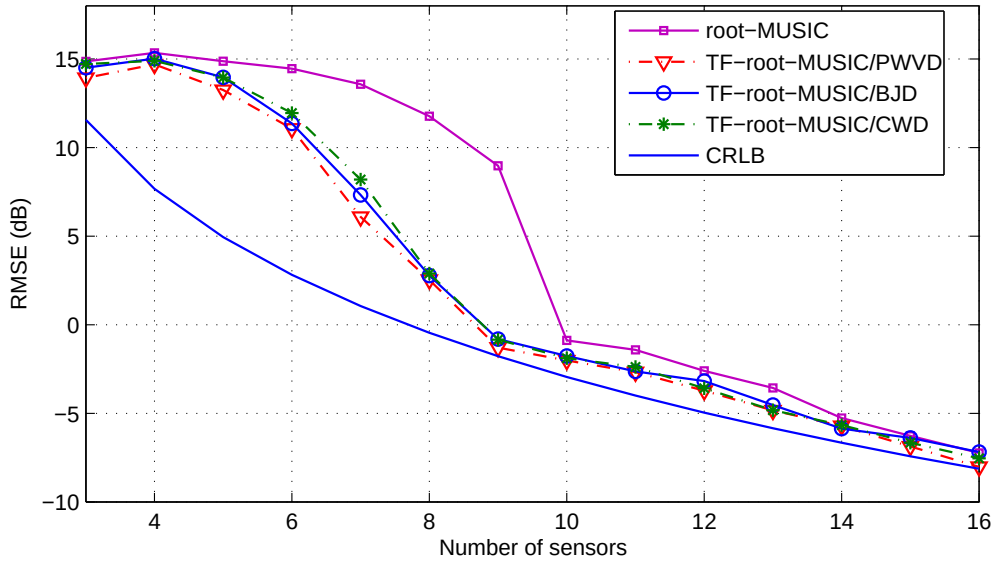

FIG. 13 – Root-MUSIC et TF-root-MUSIC : RMSE en fonction du nombre d'éléments

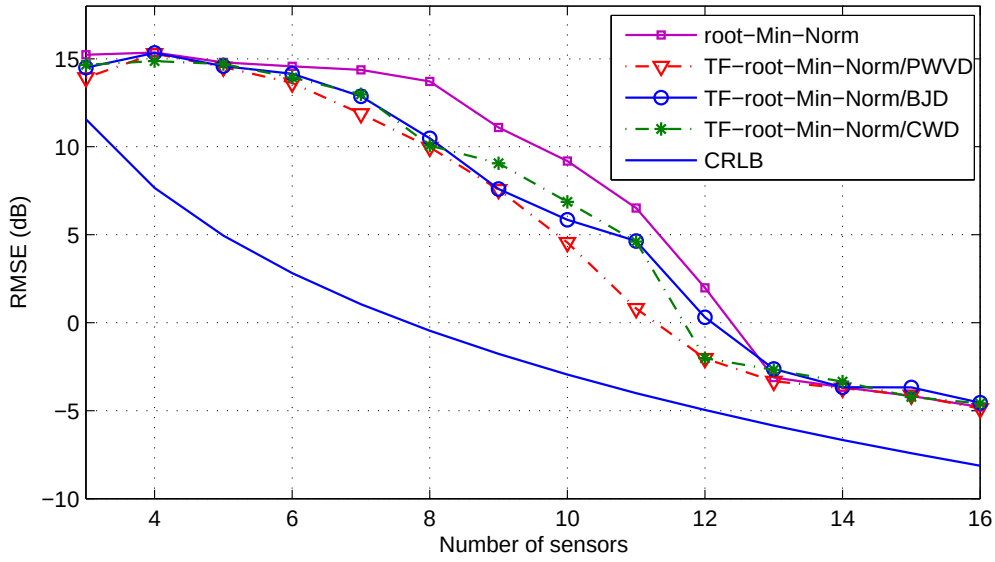

FIG. 14 – Root-Min-Norm et TF-root-Min-Norm : RMSE en fonction du nombre d'éléments

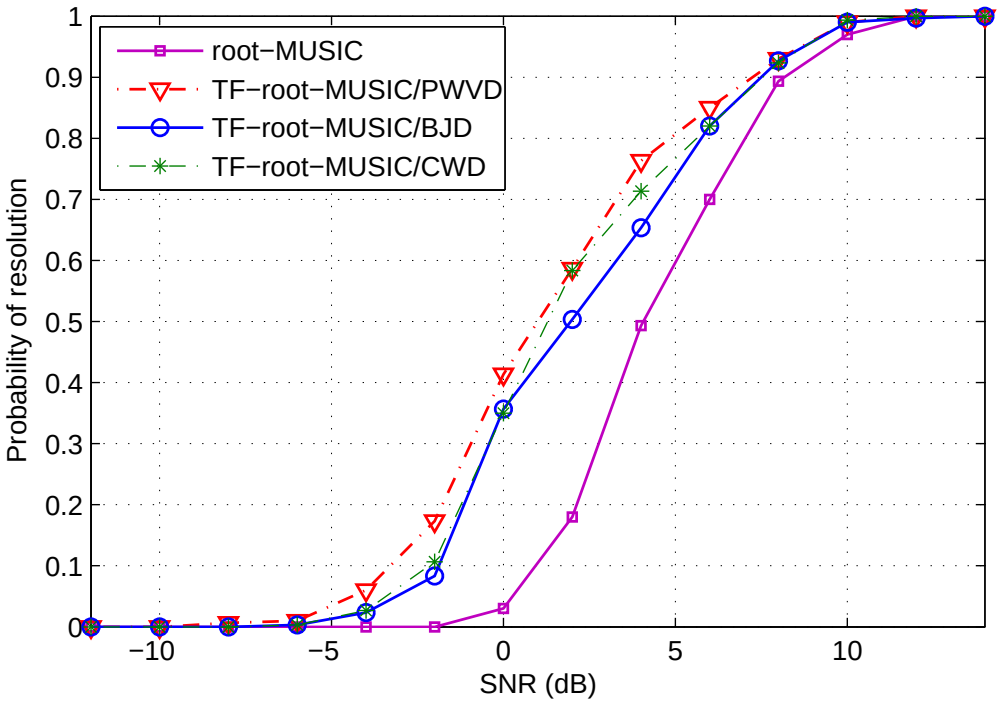

FIG. 15 – Root-MUSIC et TF-root-MUSIC : probabilité de résolution en fonction du SNR

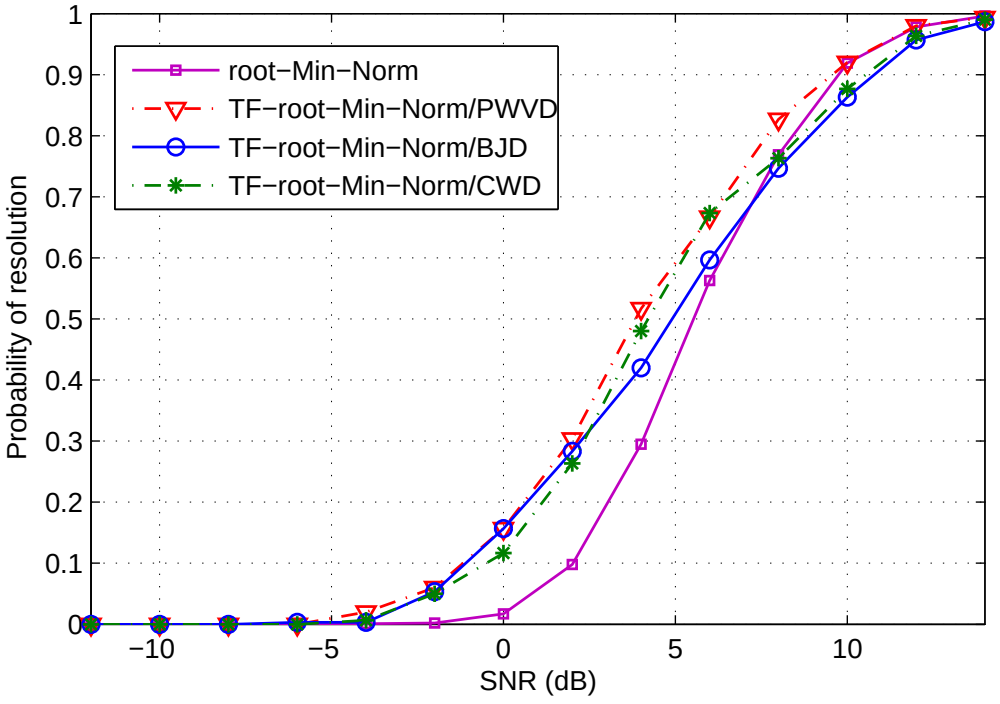

FIG. 16 – Root-Min-Norm et TF-root-Min-Norm : probabilité de résolution en fonction du SNR

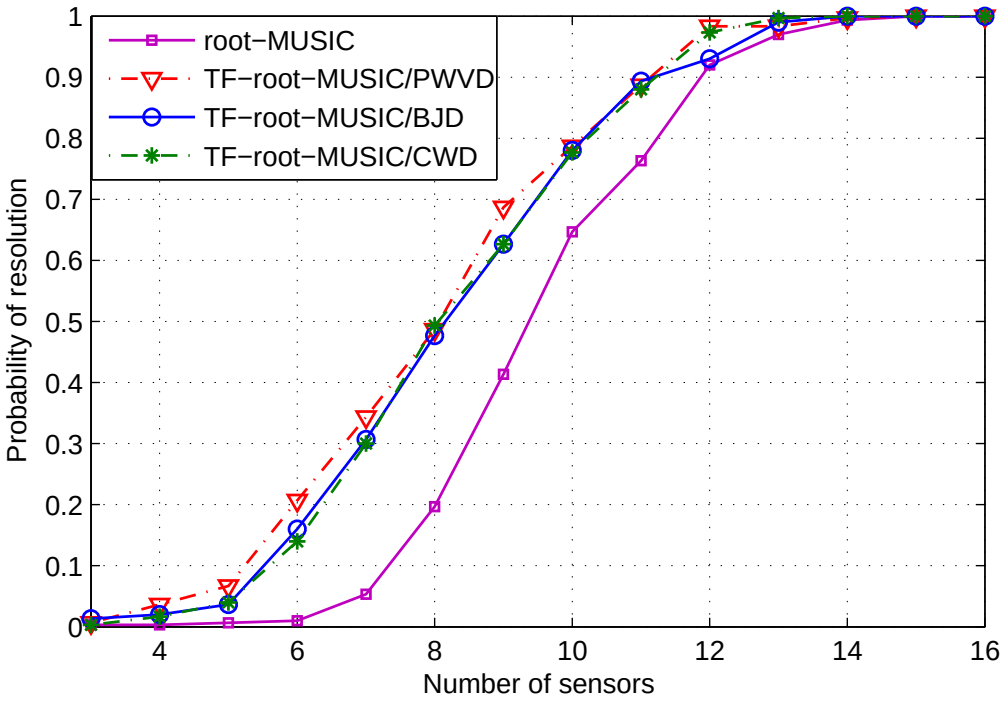

FIG. 17 – Root-MUSIC et TF-root-MUSIC : probabilité de résolution en fonction du nombre d'éléments

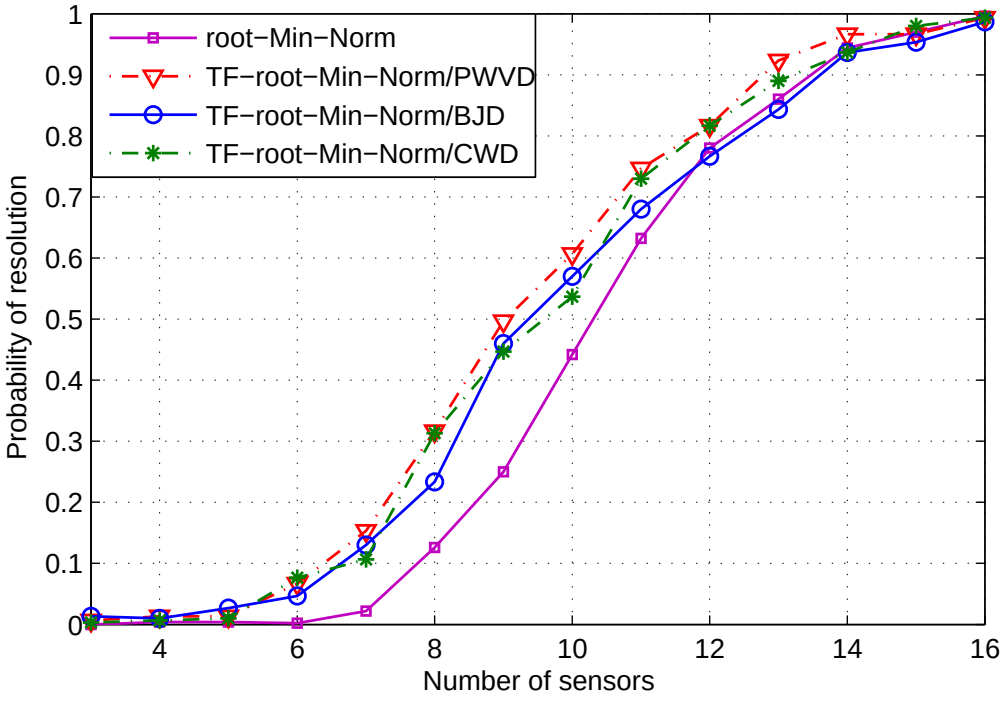

FIG. 18 – Root-Min-Norm et TF-root-Min-Norm : probabilité de résolution en fonction du nombre d'éléments

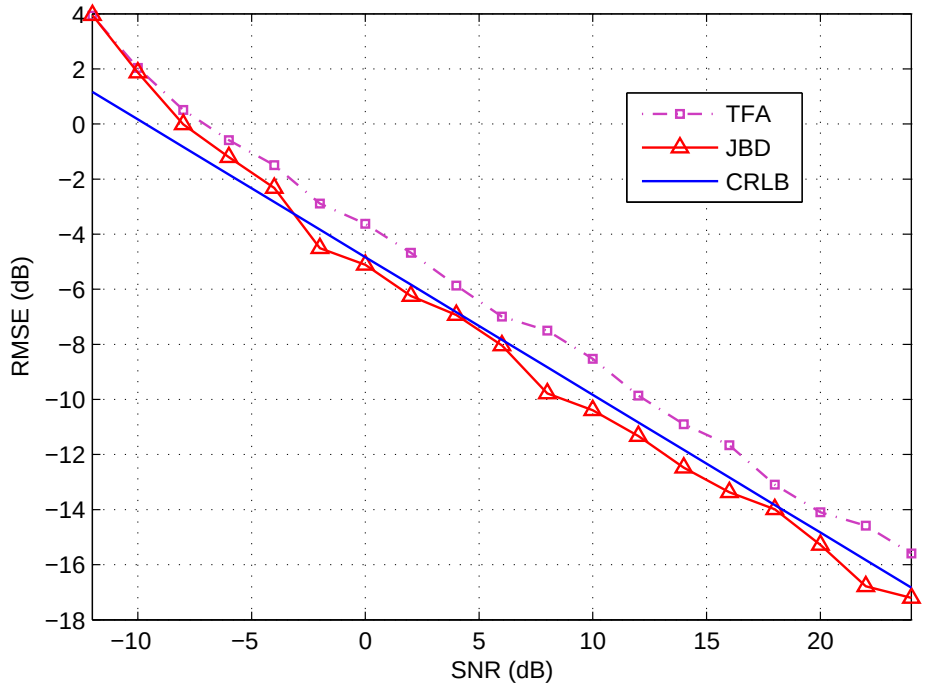

FIG. 19 – Régions des auto-termes : RMSE en fonction du SNR pour TF-TLS-ESPRIT (m=1)

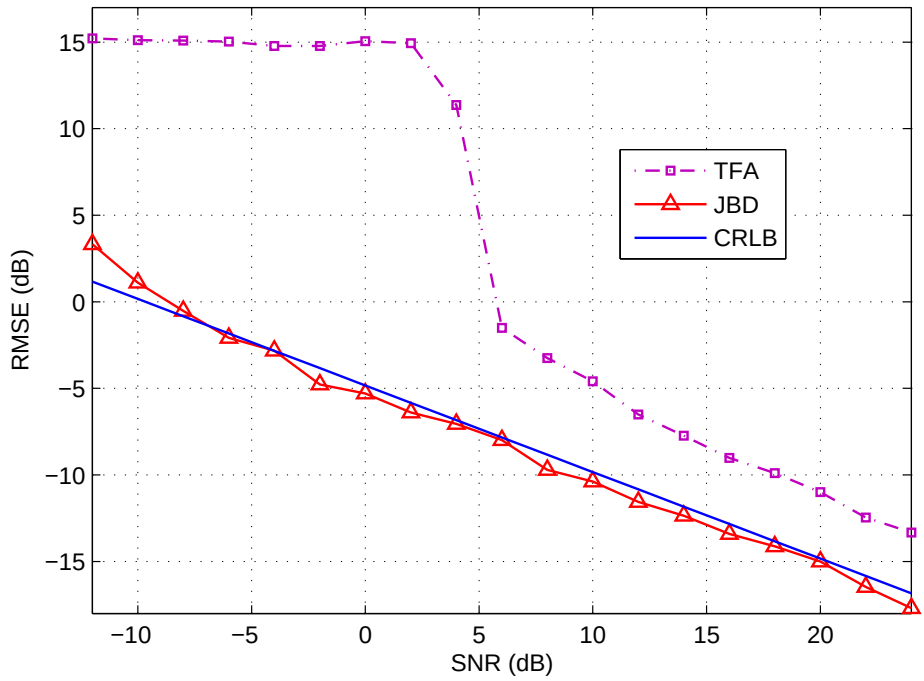

FIG. 20 – Région des cross-termes : RMSE en fonction du SNR pour TF-TLS-ESPRIT (m=1)

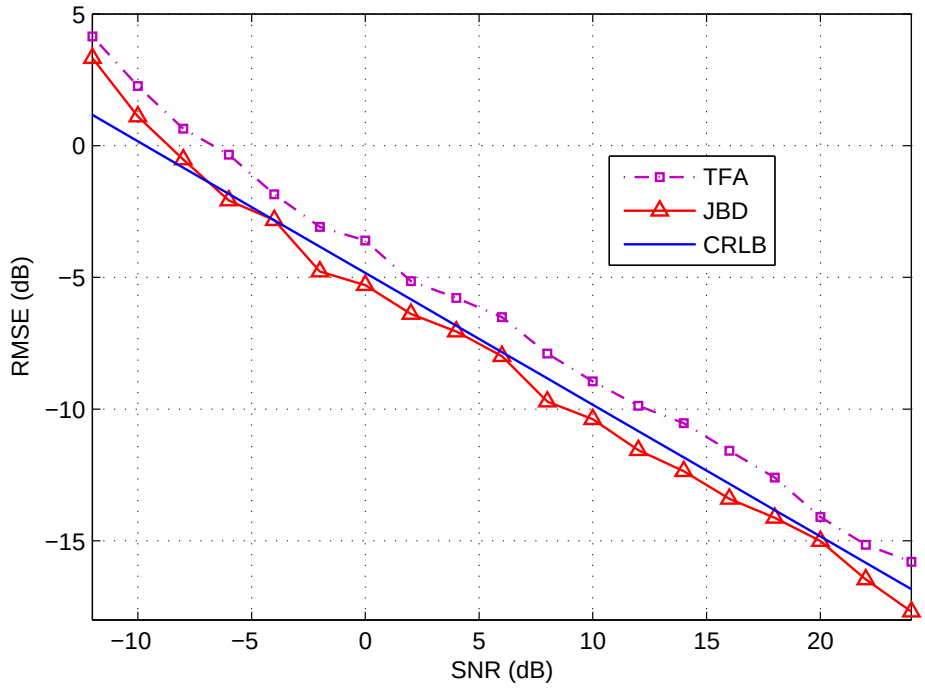

FIG. 21 – Régions des auto- et cross-termes : RMSE en fonction du SNR pour TF-TLS-ESPRIT (m=1)

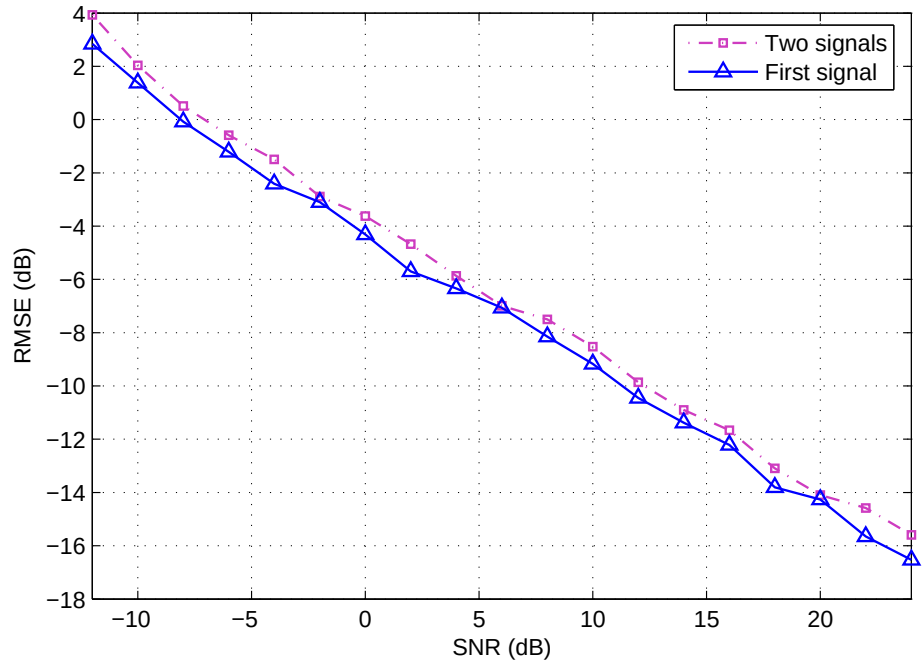

FIG. 22 – Sélection d'un signal particulier : RMSE en fonction du SNR pour TF-TLS-ESPRIT (m=1)

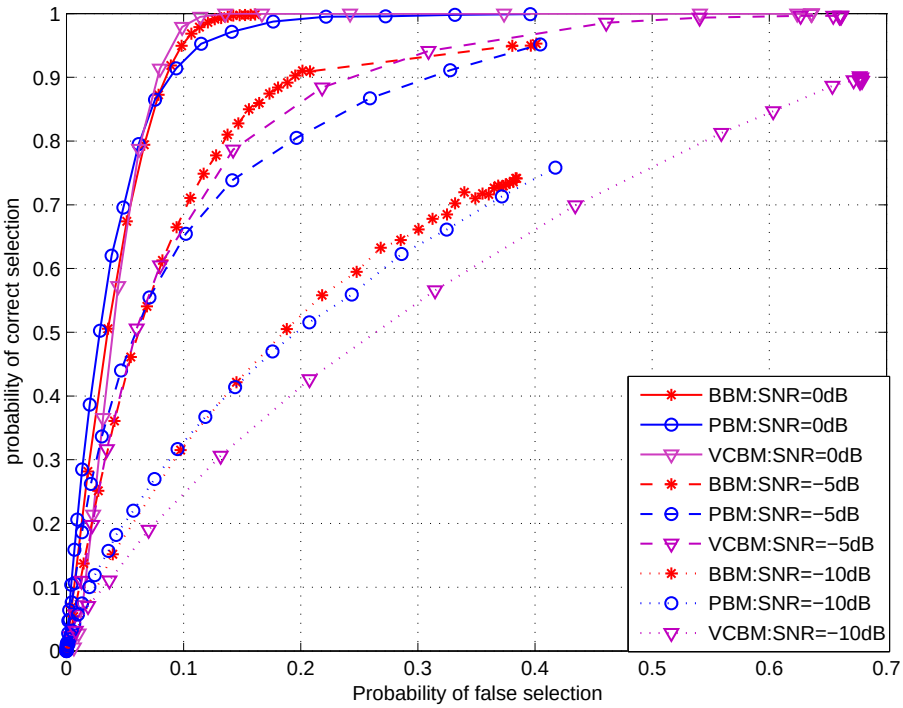

FIG. 23 – ROC des auto-termes : SNR=0, -5 and -10dB

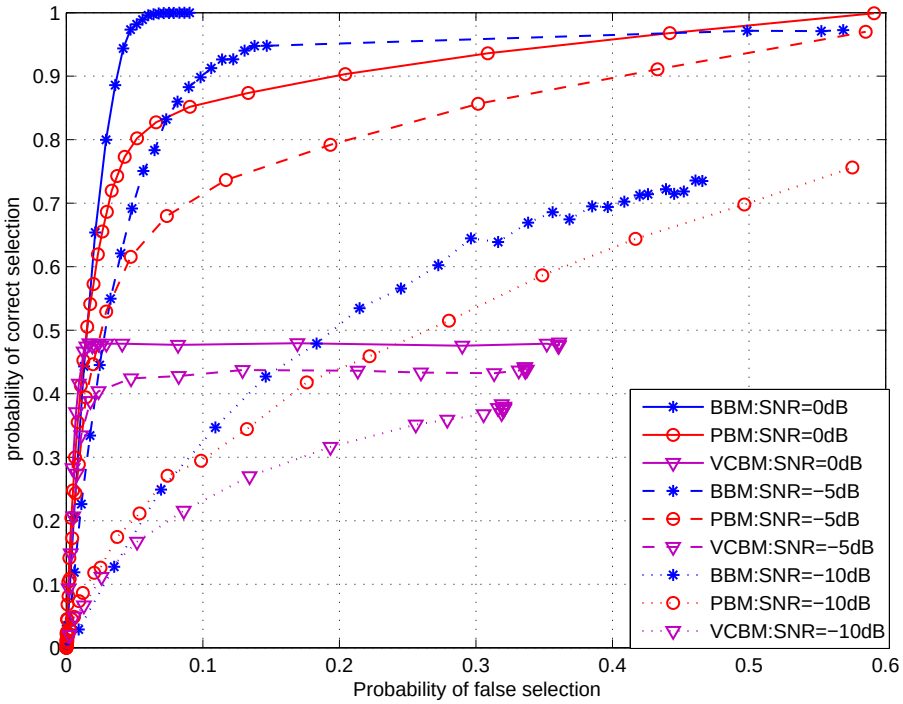

FIG. 24 – ROC des cross-termes : SNR=0, -5 and -10dB.

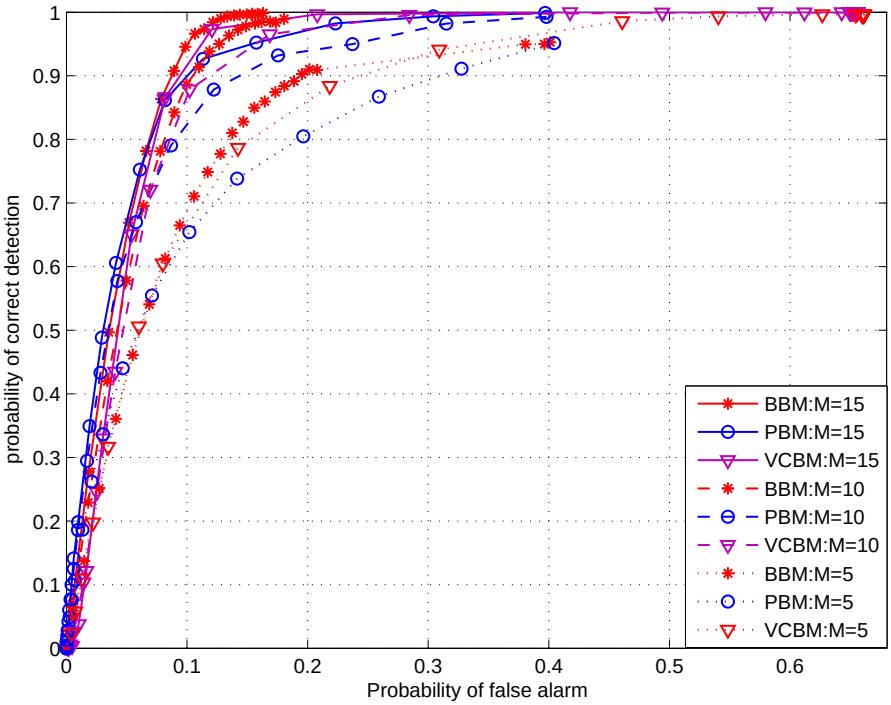

FIG. 25 – ROC des auto-termes : M=15, 10 and 5 éléments

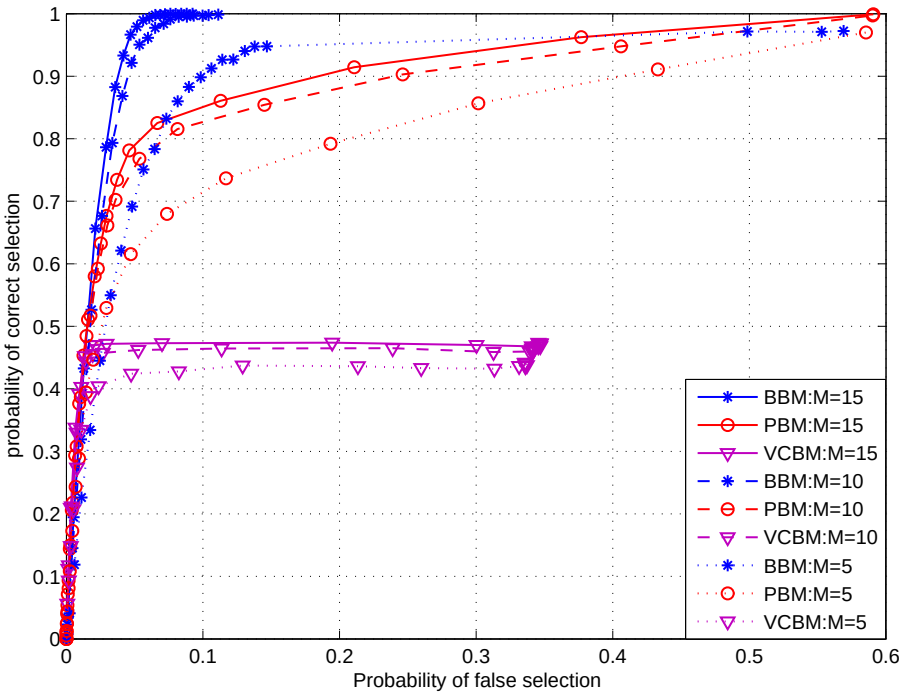

FIG. 26 – ROC des cross-termes : M=15, 10 and 5 éléments.

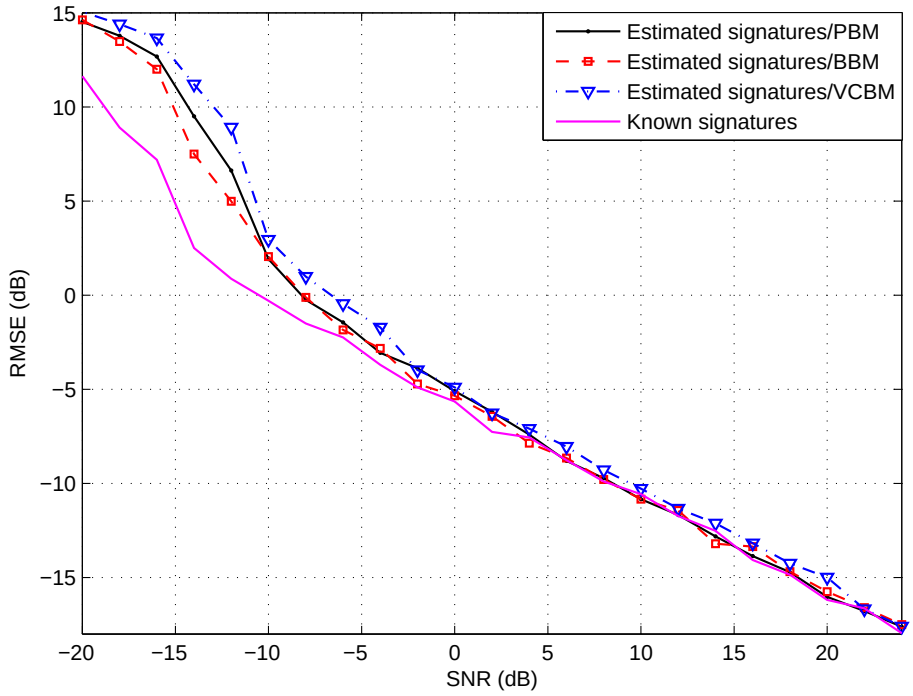

FIG. 27 – Signatures temps-fréquence estimées et inconnues : RMSE en fonction du SNR pour TF-TLS-ESPRIT (m=1)

5.4 Estimation des DOAs des signaux avec des signatures inconnues

Le but est de démontrer qu'on peut estimer les DOAs des signaux non stationnaires même si leurs signatures temps-fréquence sont complètement inconnues. Pour arriver à ce résultat, on applique deux estimations successives. On commence par l'estimation des signatures temps-fréquence de tous les signaux, ensuite on estime les DOAs en utilisant l'un des algorithmes précédemment décrits.

Deux signaux chirp sont reçus. Les fréquences de début et fin des deux signaux sont respectivement données par $(w_{1s}, w_{1e}) = (\pi, 0.2\pi)$rad et $(w_{2s}, w_{2e}) = (0.8\pi, 0)$rad. Les DOAs d'arrivée sont $\theta_1 = -10$ degrees et $\theta_2 = 10$ degrees respectivement. Un réseau linéaire d'antennes ayant six éléments, un intervalle d'observation N=256, une PWVD avec une fenêtre de Hamming sont considérés. Le TFA est utilisé comme méthode d'intégration des auto-termes. Fig. 27 illustre le RMSE de la première DOA lorsque les points (t, f) sélectionnés appartiennent aux régions auto-termes pour un l'algorithme TF-TLS-ESPRIT. Lorsque le SNR augmente, la précision d'estimation tend à être similaire à celle du cas optimal (signatures connues). A partir du $SNR = 5dB$, la précision obtenue est très proche de celle du cas optimal pour les trois méthodes simulées.

6 Conclusion générale et perspectives

L'introduction du concept temps-fréquence au problème d'estimation des directions d'arrivée a amélioré les performances des méthodes conventionnelles telles que le maximum de vraisemblance, sous espace et subspace fitting. La comparaison quantitative faite a montré que les algorithmes temps-fréquence possèdent de meilleures performances, en terme de précision et de résolution, que les méthodes conventionnelles. A titre d'exemple, une amélioration importante de la précision d'approximativement $12dB$ (pour un $SNR = 2dB$) est obtenu lorsqu'on introduit l'analyse temps-fréquence à l'algorithme MUSIC. Cependant, on a trouvé que l'application de l'analyse temps-fréquence n'est intéressante que dans des intervalles bien déterminés qui dépendent du SNR, nombre d'échantillons et nombre d'éléments de l'antenne. En dehors de ces intervalles, les méthodes temps-fréquence et conventionnelles tendent à avoir les mêmes performances. Dans ce cas, les méthodes conventionnelles sont préférées puisqu'elles possèdent le plus petit coût de calcul.

On a également comparé les deux méthodes d'intégration des auto- et cross-termes, à savoir JBD et TFA. La méthode JBD est la meilleure pour l'intégration des auto-termes et aussi des cross-termes et sa performance ne dépend pas de type des points considérés (région auto-terme ou cross-terme). Cependant, on doit mentionner que le temps de calcul de cette méthode est plus important que celui de TFA. Une amélioration de la précision d'environs $2dB$ a été obtenu lorsqu'on a considéré seulement les points appartenant à la signature d'un signal donné.

Concernant la détection des auto- et cross-termes, la méthode basée sur le bootstrap donne la meilleure performance que les méthodes basées sur la projection ou vecteur clustering dans la détection des auto-termes et aussi des cross-termes. Cependant, dans le cas des cross-termes les trois méthodes tendent à avoir les mêmes performances lorsque le SNR ou le nombre d'éléments de l'antenne augmente. Dans un tel scénario, les deux autres méthodes sont préférés puisqu'elles sont rapides. Bien que la méthode de vecteur clustering proposé possède la plus mauvaise performance pour la détection des cross-termes, elle peut être utilisée pour séparer les signatures des différents signaux.

Ce travail a énormément de perspectives. On peut citer la dérivation des expressions analytiques donnant la précision d'estimation, la probabilité de résolution dans le cas des auto-termes et des cross-termes pour les deux méthodes TFA et JBD. La variation de ces indices de performance en fonction de plusieurs paramètres tels que le SNR, le nombre d'éléments de l'antenne, le nombre d'échantillons et la nature de sources, permettrait de prédire le comportement des estimateurs temps-fréquence dans un scénario donnée afin de les comparer avec les estimateurs conventionnels pour voir si leur utilisation est intéressante. Une dérivation d'une expression analytique pour la borne de Cramer-Rao dans le cas des signaux non stationnaires est aussi intéressante puisque elle permet de déterminer la limite qu'on peut atteindre. Dans le problème de détection des auto- et cross-termes, on peut envisager l'utilisation des estimateurs de fréquence instantanée comme estimateurs des auto-termes. Le problème de la détection des auto- et cross-termes peut être aussi traité comme un problème de traitement d'image en considérant les signatures des signaux comme des objets dans une image. Cette approche permettrait d'éviter la sélection des points (t, f) isolés comme des auto- ou cross-termes.

Références

[1] K. Abed-Meraim, L.T. Nguyen, and A. Belouchrani, *Underdetermined blind source separation for fm-like signals*, Time frequency signal analysis and processing : a comprehensive reference, pp. 357-368 (Oct. 2003).

[2] A. Belouchrani, K. Abed-Meraim, M.G. Amin, and A. Zoubir, *Joint anti-diagonalisation for blind source separation*, In proceedings ICASSP, Utah, Vol.5, pp.2789-2792 (May. 2001).

[3] A. Belouchrani and M.G. Amin, *Time-frequency music*, IEEE Trans. on Signal Processing Lett,pp.109-110 (Jun. 1999).

[4] _____, *Blind source separation based on time-frequency signal representation*, IEEE Trans. on Signal Processing, Vol.46, pp.2888-2898 (Nov. 1998).

[5] L. Cirillo, A. Zoubir, and M.G. Amin, *Selection of auto- and cross-terms for blind non-stationary source separation*, in Proceedings of IEEE International Symposium of Signal Processing and Information Technology (ISSPIT), Cairo, Egypt (2001).

[6] L. Jim, Q.y. Yin, and W.j. Wang, *Time-frequency signal subspace fitting method for direction-of-arrival estimation*, ISCAS 2000-IEEE International Symposium on Circuits and Systems, Geneva, Switzerland (May 28-31,2000).

[7] Y. Zhang and M.G. Amin, *Spatial averaging of time-frequency ditribution for signal recovery in uniform linear arrays*, IEEE Trans. SP, vol. 48, no. 10, pp. 2892-2902 (2001).

[8] _____, *Blind separation of sources based on their time-frequency signatures*, In proceedings ICASSP, Istanbul, Turkey (Jun. 2000).

[9] Y. Zhang, W. Mu, and M.G. Amin, *Subspace analysis of spatial time-frequency distribution matrices*, IEEE transaction on signal processing, Vol.49, NO. 4 (Apr. 2001).

[10] _____, *Time-frequency maximum likelihood methods for direction finding*, Journal of Franklin Institute. Vol. 337(4), pp. 483-497 (Jul. 2000).

[11] _____, *Bilinear signal synthesis in array processing*, in Proceedings of ICCASP'2001, Salt Lake, UT, pp. 3577-3580 (May. 2001).

Appendix B: Cramer-Rao Bound

The likelihood function of the data is given by

$$\mathcal{L}(\mathbf{x}(1),\mathbf{x}(2),...,\mathbf{x}(N)) = \frac{1}{(2\pi)^{MN}(\sigma_n^2/2)^{MN}} \exp\left\{-\frac{1}{\sigma_n^2}\sum_{t=1}^{N}[\mathbf{x}(t)-\mathbf{A}\mathbf{s}(t)]^H[\mathbf{x}(t)-\mathbf{A}\mathbf{s}(t)]\right\}$$

Thus the log-likelihood function is

$$\ln\mathcal{L} = const - MN\ln\sigma_n^2 - \frac{1}{\sigma_n^2}\sum_{t=1}^{N}[\mathbf{x}^H(t)-\mathbf{s}^H(t)\mathbf{A}^H][\mathbf{x}(t)-\mathbf{A}\mathbf{s}(t)] \tag{1}$$

First, we evaluate the derivatives of Eq. 1 w.r.t. σ_n^2, $\{\bar{\mathbf{s}}(t)=\Re(\mathbf{s}(t))\}, \{\tilde{\mathbf{s}}(t)=\Im(\mathbf{s}(t))\}$ and θ. We have:

$$\frac{\eth \ln\mathcal{L}}{\eth\sigma_n^2} = -\frac{MN}{\sigma_n^2} + \frac{1}{\sigma_n^4}\sum_{t=1}^{N}\mathbf{n}(t)^H\mathbf{n}(t) \tag{2}$$

$$\frac{\eth \ln\mathcal{L}}{\eth\bar{\mathbf{s}}(t)} = \frac{1}{\sigma_n^2}[\mathbf{A}^H\mathbf{n}(k)+\mathbf{A}^T\mathbf{n}^*(k)] = \frac{2}{\sigma_n^2}\Re[\mathbf{A}^H\mathbf{n}(k)] \qquad k=1,2,...,N \tag{3}$$

$$\frac{\eth \ln\mathcal{L}}{\eth\tilde{\mathbf{s}}(t)} = \frac{1}{\sigma_n^2}[-j\mathbf{A}^H\mathbf{n}(k)+j\mathbf{A}^T\mathbf{n}^*(k)] = \frac{2}{\sigma_n^2}\Im[\mathbf{A}^H\mathbf{n}(k)] \qquad k=1,2,...,N \tag{4}$$

and

$$\begin{aligned}\frac{\eth \ln\mathcal{L}}{\eth w_i} &= \frac{2}{\sigma_n^2}\sum_{t=1}^{N}\Re\left[\mathbf{s}^H(t)\frac{d\mathbf{A}^H}{dw_i}\mathbf{n}(t)\right] \\ &= \frac{2}{\sigma_n^2}\sum_{t=1}^{N}\Re\left[s_i^*(t)\mathbf{d}^H(w_i)\mathbf{n}(t)\right] \qquad i=1,2,...,L\end{aligned} \tag{5}$$

where $\mathbf{d}(w)=\frac{d\mathbf{a}(w)}{dw}$ and $\mathbf{a}(w)=[1,e^{jw},...,e^{j(M-1)w}]^T$

Eq. 5 can be written more compactly as

$$\frac{\eth \ln\mathcal{L}}{\eth\theta} = \frac{2}{\sigma_n^2}\sum_{t=1}^{N}\Re\left[\mathbf{S}^H(t)\mathbf{D}^H\mathbf{n}(t)\right] \tag{6}$$

where

$$\mathbf{S}(t) = \begin{bmatrix} s_1(t) & & 0 \\ & \ddots & \\ 0 & & s_L(t) \end{bmatrix}$$

$$\mathbf{D} = [\mathbf{d}(w_1), \mathbf{d}(w_2), ..., \mathbf{d}(w_L)]$$

To proceed, we need a number of results. These are stated and proven in the following.

R1 :

$$E\left\{\mathbf{n}^H(k_1)\mathbf{n}(k_1)\mathbf{n}^H(k_2)\mathbf{n}(k_2)\right\} = \begin{cases} M^2\sigma_n^4 & \text{for} \quad k_1 \neq k_2 \\ M(M+1)\sigma_n^4 & \text{for} \quad k_1 = k_2 \end{cases} \tag{7}$$

Proof of **R1**:

For $k_1 \neq k_2$

$$E\left\{\mathbf{n}^H(k_1)\mathbf{n}(k_1)\mathbf{n}^H(k_2)\mathbf{n}(k_2)\right\} = [E\left\{\bar{\mathbf{n}}^T(k_1)\bar{\mathbf{n}}(k_1)\right\} + E\left\{\tilde{\mathbf{n}}^T(k_1)\tilde{\mathbf{n}}(k_1)\right\}]^2 = M^2\sigma_n^4$$

For $k_1 = k_2$

$$\begin{aligned} E\left\{\mathbf{n}^H(k_1)\mathbf{n}(k_1)\mathbf{n}^H(k_2)\mathbf{n}(k_2)\right\} &= E[\bar{\mathbf{n}}^T(k_1)\bar{\mathbf{n}}(k_1) + \tilde{\mathbf{n}}^T(k_1)\tilde{\mathbf{n}}(k_1)]^2 \\ &= E[\bar{\mathbf{n}}^T(k_1)\bar{\mathbf{n}}(k_1)]^2 + 2E[\tilde{\mathbf{n}}^T(k_1)\tilde{\mathbf{n}}(k_1)]E[\bar{\mathbf{n}}^T(k_1)\bar{\mathbf{n}}(k_1)] \\ &\quad + E[\tilde{\mathbf{n}}^T(k_1)\tilde{\mathbf{n}}(k_1)]^2 \\ &= 2E[\bar{\mathbf{n}}^T(k_1)\bar{\mathbf{n}}(k_1)]^2 + \frac{1}{2}M^2\sigma_n^4 \end{aligned}$$

Since

$$\begin{aligned} E[\bar{\mathbf{n}}^T(k_1)\bar{\mathbf{n}}(k_1)]^2 = E\sum_{i_1=1}^{M}\sum_{i_2=1}^{M}\bar{n}_{i_1}^2(k_1)\bar{n}_{i_2}^2(k_1) &= \sum_{i_1=1}^{M}\sum_{i_2=1, i_2\neq i_1}^{M} E\bar{n}_{i_1}^2(k_1)E\bar{n}_{i_2}^2(k_1) \\ &\quad + \sum_{i_1=1}^{M}\bar{n}_{i_1}^4(k_1) \\ &= (M-1)M\frac{\sigma_n^4}{4} + 3M\frac{\sigma_n^4}{4} = M(M+2)\frac{\sigma_n^4}{4} \end{aligned}$$

The proof is finished.

R2 :

$$E\left\{\mathbf{n}^H(k_1)\mathbf{n}(k_1)\mathbf{n}^T(k_2)\right\} = 0 \qquad \text{for all} \quad k_1 \quad \text{and} \quad k_2 \tag{8}$$

Proof of **R2**:

For $k_1 \neq k_2$, the result is immediate since $\mathbf{n}(k_1)$ and $\mathbf{n}(k_2)$ are independent. For $k_1 = k_2$, it follows from the fact that the third-order moments of Gaussian random variables are also equal to zero.

R3:

$$\begin{aligned}
\Re(\mathbf{s})\Re(\mathbf{x}^T) &= \frac{1}{2}[\Re(\mathbf{s}\mathbf{x}^T) + \Re(\mathbf{s}\mathbf{x}^H)] \\
\Im(\mathbf{s})\Im(\mathbf{x}^T) &= -\frac{1}{2}[\Re(\mathbf{s}\mathbf{x}^T) - \Re(\mathbf{s}\mathbf{x}^H)] \\
\Re(\mathbf{s})\Im(\mathbf{x}^T) &= \frac{1}{2}[\Im(\mathbf{s}\mathbf{x}^T) - \Im(\mathbf{s}\mathbf{x}^H)]
\end{aligned} \tag{9}$$

Proof of **R3**: the result follows from some straightforward calculations.

R4: Let $\mathbf{H}$ be a nonsingular complex matrix, and denote its inverse by $\mathbf{G} \triangleq \mathbf{H}^{-1}$. Then

$$\begin{bmatrix} \bar{\mathbf{H}} & -\tilde{\mathbf{H}} \\ \tilde{\mathbf{H}} & \bar{\mathbf{H}} \end{bmatrix}^{-1} = \begin{bmatrix} \bar{\mathbf{G}} & -\tilde{\mathbf{G}} \\ \tilde{\mathbf{G}} & \bar{\mathbf{G}} \end{bmatrix} \tag{10}$$

Proof of **R4**: the equality Eq. 10 can equivalently written as

$$\begin{aligned}
\bar{\mathbf{H}}\bar{\mathbf{G}} - \tilde{\mathbf{H}}\tilde{\mathbf{G}} &= \mathbf{I} \\
\bar{\mathbf{H}}\tilde{\mathbf{G}} + \tilde{\mathbf{H}}\bar{\mathbf{G}} &= \mathbf{0}
\end{aligned}$$

which certainly must hold since

$$\begin{aligned}
\mathbf{I} = \mathbf{H}\mathbf{G} &= (\bar{\mathbf{H}} + j\tilde{\mathbf{H}})(\bar{\mathbf{G}} + j\tilde{\mathbf{G}}) \\
&= (\bar{\mathbf{H}}\bar{\mathbf{G}} - \tilde{\mathbf{H}}\tilde{\mathbf{G}}) + j(\bar{\mathbf{H}}\tilde{\mathbf{G}} - \tilde{\mathbf{H}}\bar{\mathbf{G}})
\end{aligned}$$

We turn now to the evaluation of the CRB covariance matrix, which is given by

$$\mathbf{\Omega} = (E\left\{\psi\psi^T\right\})^{-1} \tag{11}$$

where

$$\psi^T = \mathfrak{d} \ln \mathcal{L}/\mathfrak{d}[\sigma, \bar{\mathbf{s}}^T(1), \tilde{\mathbf{s}}^T(1), \bar{\mathbf{s}}^T(2), \tilde{\mathbf{s}}^T(2), ..., \bar{\mathbf{s}}^T(N), \tilde{\mathbf{s}}^T(N), \theta^T] \tag{12}$$

Using **R1**, we get

$$\begin{aligned} E\left[\frac{\mathfrak{d} \ln \mathcal{L}}{\mathfrak{d}\sigma_n^2}\right]^2 &= \frac{M^2N^2}{\sigma_n^4} - 2\frac{MN}{\sigma_n^6}\sum_{k_1=1}^{N} \mathbf{n}(k_1)^H \mathbf{n}(k_1) \\ &\quad + \frac{1}{\sigma_n^8}\sum_{k_1=1}^{N}\sum_{k_2=1}^{N} E\left\{\mathbf{n}^H(k_1)\mathbf{n}(k_1)\mathbf{n}^H(k_2)\mathbf{n}(k_2)\right\} \\ &= \frac{M^2N^2}{\sigma_n^4} - 2\frac{M^2N^2}{\sigma_n^4} \\ &\quad + \frac{MN}{\sigma_n^4}[(N-1)M + (M+1)] \\ &= \frac{MN}{\sigma_n^4} \end{aligned} \tag{13}$$

Using **R2**, we note that $\frac{\mathfrak{d} \ln \mathcal{L}}{\mathfrak{d}\sigma_n^2}$ is not correlated with any of the other derivatives in Eqs. 3,4 and 6. Next, we use **R3** and the fact that $E\left\{\mathbf{n}(k_1)\mathbf{n}^T(k_2)\right\} = 0$ for all k_1 and k_2, to obtain

$$\begin{aligned} E\left[\frac{\mathfrak{d} \ln \mathcal{L}}{\mathfrak{d}\bar{\mathbf{s}}(k)}\right]\left[\frac{\mathfrak{d} \ln \mathcal{L}}{\mathfrak{d}\bar{\mathbf{s}}(p)}\right]^T &= \frac{4}{\sigma_n^4}\frac{1}{2}\Re[E\mathbf{A}^H\mathbf{n}(k)\mathbf{n}^H(p)\mathbf{A}] \\ &= \frac{2}{\sigma_n^2}\Re[\mathbf{A}^H\mathbf{A}]\delta_{k,p} \end{aligned} \tag{14}$$

$$\begin{aligned} E\left[\frac{\mathfrak{d} \ln \mathcal{L}}{\mathfrak{d}\bar{\mathbf{s}}(k)}\right]\left[\frac{\mathfrak{d} \ln \mathcal{L}}{\mathfrak{d}\tilde{\mathbf{s}}(p)}\right]^T &= -\frac{4}{\sigma_n^4}\frac{1}{2}\Im[E\mathbf{A}^H\mathbf{n}(k)\mathbf{n}^H(p)\mathbf{A}] \\ &= -\frac{2}{\sigma_n^2}\Im[\mathbf{A}^H\mathbf{A}]\delta_{k,p} \end{aligned} \tag{15}$$

$$\begin{aligned} E\left[\frac{\mathfrak{d} \ln \mathcal{L}}{\mathfrak{d}\bar{\mathbf{s}}(k)}\right]\left[\frac{\mathfrak{d} \ln \mathcal{L}}{\mathfrak{d}\theta}\right]^T &= \frac{4}{\sigma_n^4}\sum_{t=1}^{N}\frac{1}{2}\Re[E\mathbf{A}^H\mathbf{n}(k)n^H(t)\mathbf{DS}(t)] \\ &= \frac{2}{\sigma_n^2}\Re[\mathbf{A}^H\mathbf{DS}(k)] \end{aligned} \tag{16}$$

$$E\left[\frac{\partial \ln \mathcal{L}}{\partial \tilde{\mathbf{s}}(k)}\right]\left[\frac{\partial \ln \mathcal{L}}{\partial \tilde{\mathbf{s}}(p)}\right]^T = \frac{4}{\sigma_n^4}\frac{1}{2}\Re[E\mathbf{A}^H\mathbf{n}(k)\mathbf{n}^H(p)\mathbf{A}]$$
$$= \frac{2}{\sigma_n^2}\Re[\mathbf{A}^H\mathbf{A}]\delta_{k,p} \tag{17}$$

$$E\left[\frac{\partial \ln \mathcal{L}}{\partial \tilde{\mathbf{s}}(k)}\right]\left[\frac{\partial \ln \mathcal{L}}{\partial \theta}\right]^T = \frac{4}{\sigma_n^4}\sum_{t=1}^{N}\left(-\frac{1}{2}\right)\Im[E\mathbf{S}^H(t)\mathbf{D}^H\mathbf{n}(t)\mathbf{n}^H(k)\mathbf{A}]^T$$
$$= -\frac{2}{\sigma_n^2}\Im[\mathbf{S}^H(k)\mathbf{D}^H\mathbf{A}]^T \tag{18}$$

$$E\left[\frac{\partial \ln \mathcal{L}}{\partial \theta}\right]\left[\frac{\partial \ln \mathcal{L}}{\partial \theta}\right]^T = \frac{4}{\sigma_n^4}\frac{1}{2}\sum_{k_1=1}^{N}\sum_{k_2=1}^{N}\Re[E\mathbf{S}(k_1)\mathbf{D}^H\mathbf{n}(k_1)\mathbf{n}^H(k_2)\mathbf{D}\mathbf{S}(k_2)]$$
$$= \frac{2}{\sigma_n^2}\sum_{k=1}^{N}\Re[\mathbf{S}^H(k)\mathbf{D}^H\mathbf{D}\mathbf{S}(k)] = \mathbf{\Gamma} \tag{19}$$

Introduce the following notations:

$$Var_{CR}(\sigma_n^2) = \sigma_n^4/MN$$
$$\mathbf{H} = \frac{2}{\sigma_n^2}\mathbf{A}^H\mathbf{A}$$
$$\mathbf{G} = \mathbf{H}^{-1}$$
$$\mathbf{\Delta}_k = \frac{2}{\sigma_n^2}\mathbf{A}^H\mathbf{D}\mathbf{S}(k) \tag{20}$$

Observe that since the matrix $\mathbf{H}$ is Hermitian, its imaginary part must be skew-symmetric $\tilde{\mathbf{H}}^T = -\tilde{\mathbf{H}}$. Inserting Eqs. 13 to 19 into Eqs. 11 and 12, we get

$$\Omega = \begin{bmatrix} Var_{CR}^{-1}(\sigma_n^2) & & & & \mathbf{0} & & \\ & \bar{\mathbf{H}} & -\tilde{\mathbf{H}} & & & & \bar{\mathbf{\Delta}}_1 \\ & \tilde{\mathbf{H}} & \bar{\mathbf{H}} & & \mathbf{0} & & \tilde{\mathbf{\Delta}}_1 \\ & & & \ddots & & & \vdots \\ \mathbf{0} & & \mathbf{0} & & \bar{\mathbf{H}} & -\tilde{\mathbf{H}} & \tilde{\mathbf{\Delta}}_N \\ & & & & \tilde{\mathbf{H}} & \bar{\mathbf{H}} & \tilde{\mathbf{\Delta}}_N \\ & \bar{\mathbf{\Delta}}_1^T & \tilde{\mathbf{\Delta}}_1^T & \cdots & \bar{\mathbf{\Delta}}_N^T & \tilde{\mathbf{\Delta}}_N^T & \mathbf{\Gamma} \end{bmatrix} \tag{21}$$

We note that Eq. 21 is a standard result on the inverse of a partitioned matrix. Using **R4**, we get

$$CRB^{-1}(\theta) = \mathbf{\Gamma} - [\bar{\mathbf{\Delta}}_1^T \tilde{\mathbf{\Delta}}_1^T \cdots \bar{\mathbf{\Delta}}_N^T \tilde{\mathbf{\Delta}}_N^T] \begin{bmatrix} \bar{\mathbf{G}} & -\tilde{\mathbf{G}} & & & & \\ & & & & \mathbf{0} & \\ \tilde{\mathbf{G}} & \bar{\mathbf{G}} & & & & \\ & & \ddots & & & \\ & & & & \bar{\mathbf{G}} & -\tilde{\mathbf{G}} \\ & \mathbf{0} & & & & \\ & & & & \tilde{\mathbf{G}} & \bar{\mathbf{G}} \end{bmatrix} \begin{bmatrix} \bar{\mathbf{\Delta}}_1^T \\ \tilde{\mathbf{\Delta}}_1^T \\ \vdots \\ \bar{\mathbf{\Delta}}_N^T \\ \tilde{\mathbf{\Delta}}_N^T \end{bmatrix} \tag{22}$$

Next, observe that

$$\begin{bmatrix} \bar{\mathbf{G}} & -\tilde{\mathbf{G}} \\ \tilde{\mathbf{G}} & \bar{\mathbf{G}} \end{bmatrix} \begin{bmatrix} \bar{\mathbf{\Delta}} \\ \tilde{\mathbf{\Delta}} \end{bmatrix} = \begin{bmatrix} \bar{\mathbf{G}}\bar{\mathbf{\Delta}} - \tilde{\mathbf{G}}\tilde{\mathbf{\Delta}} \\ \tilde{\mathbf{G}}\bar{\mathbf{\Delta}} + \bar{\mathbf{G}}\tilde{\mathbf{\Delta}} \end{bmatrix} = \begin{bmatrix} \overline{\mathbf{G}\mathbf{\Delta}} \\ \widetilde{\mathbf{G}\mathbf{\Delta}} \end{bmatrix} \tag{23}$$

And that

$$[\bar{\mathbf{\Delta}}^T \tilde{\mathbf{\Delta}}^T] \begin{bmatrix} \overline{\mathbf{G}\mathbf{\Delta}} \\ \widetilde{\mathbf{G}\mathbf{\Delta}} \end{bmatrix} = \Re[\mathbf{\Delta}^H \mathbf{G}\mathbf{\Delta}] \tag{24}$$

From Eqs. 22, 23 and 24, it follows that

$$
\begin{aligned}
CRB^{-1}(\theta) &= \mathbf{\Gamma} - \sum_{t=1}^{N} \Re[\mathbf{\Delta}_t^H \mathbf{G} \mathbf{\Delta}_t] = \frac{2}{\sigma_n^2} \sum_{t=1}^{N} \Re[\mathbf{S}^H(t)\mathbf{D}^H\mathbf{D}\mathbf{S}(t) - \mathbf{S}^H(t)\mathbf{D}^H\mathbf{A}(\mathbf{A}^H\mathbf{A})^{-1}\mathbf{A}^H\mathbf{S}(t)] \\
&= \frac{2}{\sigma_n^2} \sum_{t=1}^{N} \Re\left\{\mathbf{S}^H(t)\mathbf{D}^H[\mathbf{I} - \mathbf{A}(\mathbf{A}^H\mathbf{A})^{-1}\mathbf{A}^H]\mathbf{D}\mathbf{S}(t)\right\} \\
&= \frac{2}{\sigma_n^2} \sum_{t=1}^{N} \Re\left\{\mathbf{S}^H(t)\mathcal{D}\mathbf{S}(t)\right\} \\
&= \frac{2N}{\sigma^2}\{\Re[\mathcal{D} \odot \hat{\mathbf{R}}_{\mathbf{ss}}^T]\} \qquad (25)
\end{aligned}
$$

where

$$
\mathcal{D} = \mathbf{D}^H[\mathbf{I} - \mathbf{A}(\mathbf{A}^H\mathbf{A})^{-1}\mathbf{A}^H]\mathbf{D}
$$

and

$$
\hat{\mathbf{R}}_{\mathbf{ss}} = \frac{1}{N} \sum_{t=1}^{N} \mathbf{s}(t)\mathbf{s}(t)^H
$$

which completes the proof of the deterministic CRB expression.

Appendix C: Joint Block Diagonalisation Algorithm

Using equations Eq. 3.20 and the equalities $c^2 = (\cos(2\gamma)+1)/2, |s|^2 = (1-\cos(2\gamma))/2$, and $cs = \sin(2\gamma)e^{i\alpha}/2$, we obtain

$$|\mathbf{D}_k^{'}(p,j)|^2 - constant = -\mathbf{x}_{kj}^T\mathbf{v} \qquad j \neq p \tag{1}$$

$$|\mathbf{D}_k^{'}(j,p)|^2 - constant = -\mathbf{y}_{kj}^T\mathbf{v} \qquad j \neq p \tag{2}$$

$$|\mathbf{D}_k^{'}(j,p)|^2 - constant = \mathbf{v}^T\mathbf{G}_k\mathbf{v} + \mathbf{g}_k^T\mathbf{v} \tag{3}$$

where *constant* denotes terms independent from (γ, α), thus

$$\mathbf{G} = \sum_{k=1}^{K}\mathbf{G}_k, \quad \mathbf{g} = \sum_{k=1}^{K}(\mathbf{g}_k - \sum_{j=1, j\neq p}^{L}(\mathbf{x}_{kj} + \mathbf{y}_{kj}))$$

$\mathbf{G}_k$, $\mathbf{g}_k$, $\mathbf{x}_{kj}$, and $\mathbf{y}_{kj}$ are given by:

$$\mathbf{G}_k = \Re(\mathbf{z}_k\mathbf{z}_k^H)$$

$$\mathbf{g}_k = \Re((\mathbf{D}_k^H(p,p) + \mathbf{D}_k^H(q,q))\mathbf{z}_k)$$

$$\mathbf{z}_k = \frac{1}{2}\begin{bmatrix} \mathbf{D}_k(p,p) - \mathbf{D}_k(q,q) \\ \mathbf{D}_k(q,p) + \mathbf{D}_k(p,q) \\ i(\mathbf{D}_k(q,p) - \mathbf{D}_k(p,q)) \end{bmatrix}$$

$$\mathbf{x}_{kj} = \begin{bmatrix} (|\mathbf{D}_k(q,j)|^2 - |\mathbf{D}_k(p,j)|^2)/2 \\ \Re(\mathbf{D}_k(p,j)\mathbf{D}_k^H(q,j)) \\ \Im(\mathbf{D}_k(p,j)\mathbf{D}_k^H(q,j)) \end{bmatrix}$$

$$\mathbf{y}_{kj} = \begin{bmatrix} (|\mathbf{D}_k(j,q)|^2 - |\mathbf{D}_k(j,p)|^2)/2 \\ \Re(\mathbf{D}_k^H(j,p)\mathbf{D}_k(j,q)) \\ \Im(\mathbf{D}_k^H(j,p)\mathbf{D}_k(j,q)) \end{bmatrix}$$

Using Eqs. 2 and 3, we obtain

$$\tilde{\mathbf{g}} = -\sum_{k=1}^{K}\sum_{j=1}^{L}(\mathbf{x}_{kj}\mathbf{y}_{kj})$$

The partial derivatives of $\mathcal{C}(\gamma,\alpha)$ are null when Eq. 3.28 is maximised.

$$\frac{\partial}{\partial\alpha}\mathcal{C}(\gamma,\alpha) = \tilde{\mathbf{g}}^T\frac{\partial\mathbf{v}}{\partial\alpha} = 0 \tag{4}$$

$$\frac{\partial}{\partial\gamma}\mathcal{C}(\gamma,\alpha)=\tilde{\mathbf{g}}^T\frac{\partial\mathbf{v}}{\partial\gamma}=0 \tag{5}$$

With

$$\frac{\partial\mathbf{v}}{\partial\alpha}=\sin(2\gamma)\begin{bmatrix}0\\-\sin(\alpha)\\\cos(\alpha)\end{bmatrix}$$
$$\frac{\partial\mathbf{v}}{\partial\gamma}=2\begin{bmatrix}-\sin(2\gamma)\\\cos(2\gamma)\cos(\alpha)\\\cos(2\gamma)\sin(\alpha)\end{bmatrix} \tag{6}$$

When we replace Eq. 6 into Eq. 4 and 5, we obtain

$$\tan(\alpha)=\frac{\Im(a)}{\Re(a)} \tag{7}$$
$$\tan(2\gamma)=-2\frac{\Re(e^{-i\alpha}a)}{b} \tag{8}$$

Then, α and γ can be expressed as follows

$$\alpha=\arctan(\frac{\Im(a)}{\Re(a)}) \tag{9}$$
$$\gamma=\frac{1}{2}\arctan(-2\frac{\Re(e^{-i\alpha}a)}{b}) \tag{10}$$

Bibliography

[1] K. Abed-Meraim, L.T. Nguyen, and A. Belouchrani, *Underdetermined blind source separation for fm-like signals*, Time frequency signal analysis and processing: a comprehensive reference, pp. 357-368 (Oct. 2003).

[2] R. Altes, *Sonar for generalized target description and its similarity to animal echolocation systems*, J. Acoust. Soc. Amer., vol. 59, pp.97105 (1976).

[3] F. Auger, O. Lemoine, and P. Gonçalvés, *The time-frequency toolbox*, http://tftb.nongnu.org/.

[4] A. Belouchrani, K. Abed-Meraim, M.G. Amin, and A. Zoubir, *Joint anti-diagonalisation for blind source separation*, In proceedings ICASSP, Utah, Vol.5, pp.2789-2792 (May. 2001).

[5] A. Belouchrani, K. Abed-Meriam, and Y. Hua, *Jacobi-like algorithms for joint block diagonalisation: application to source localisation*, Special session on: sensor array multichannel processing (Jan. 2006).

[6] A. Belouchrani and M.G. Amin, *Source separation based on the diagonalisation of a combined set of spatial time-frequency ditribution matrices*, in Proceeding ICASSP, Munich, Germany (Apr.1997).

[7] ———, *Blind source separation using the spatial ambiguity functions*, in Proceeding IEEE Int. Symp. Time-frequency and Time-Scale Analysis,pp.413-416 (Aug. 1997).

[8] ———, *A new approach for blind source separation using time-frequency distributions*, in Proceeding SPIE Conference on Advanced Algorithms and Architectures for signal processing, Denver, Colorado (Aug.1996).

[9] ———, *Time-frequency music*, IEEE Trans. on Signal Processing Lett,pp.109-110 (Jun. 1999).

[10] ———, *Blind source separation based on time-frequency signal representation*, IEEE Trans. on Signal Processing, Vol.46, pp.2888-2898 (Nov. 1998).

[11] A. Belouchrani, M.G. Amin, and K. Abed-Meraim, *Direction finding in correlated noise fields based on joint block-diagonalisation of spatio-temporal correlation matrices*, IEEE Signal Processing Lett., Vol.4, pp. 266-269 (Apr. 1997).

[12] B. Boashash, *Time frequency signal analysis and processing: A comprehensive reference*, Elsevier Science Publ, San Diego, Oct. 2003.

[13] L. Cirillo, A. Zoubir, and M.G. Amin, *Selection of auto- and cross-terms for blind non-stationary source separation*, in Proceedings of IEEE International Symposium of Signal Processing and Information Technology (ISSPIT), Cairo, Egypt (2001).

[14] L. Cirillo, A.M. Zoubir, and A.B. Gershman, *Direction of arrival estimation for uncorrelated fm signals*, IEEE Trans. SP (2002).

[15] L. Giulieri, H. Ghennioui, N. Thirion-Moreau, and E. Moreau, *Nonorthogonal joint diagonalisation of spatial quadratique time-frequency matrices for source separation*, IEEE Trans. SP, vol. 12, no. 5 (2005).

[16] L. Giulieri, N. Thirion-Moreau, and P.Y. Arques, *Blind source separation based on bilinear time-frequency representations: a performance analysis*, in Proceedings of ICCASP, Vol. 2, 2002, pp.1649-1652 (2002).

[17] ———, *Blind source separation using bilinear and quadratic time-frequency representations*, in ICA'2001, San Diego (Dec. 2001).

[18] A. Hassanien, A.B. Gershman, and M.G. Amin, *Time-frequency esprit for direction of arrival estimation of chirp signals*, in Proceedings sensor array and multichannel workshop (SAM) (2002).

[19] L. Jim, Q.y. Yin, and W.j. Wang, *Time-frequency signal subspace fitting method for direction-of-arrival estimation*, ISCAS 2000-IEEE International Symposium on Circuits and Systems, Geneva, Switzerland (May 28-31,2000).

[20] E. Kreyszig, *Introductory functional analysis with applications*, Wiley, New York, 1989.

[21] H. Krim and M. Viberg, *Two decades of array signal processing research*, IEEE Signal processing magazine (Jul.1996).

[22] F. Li, H. Liu, and R.J. Vaccaro, *Performance analysis for doa estimation algorithms: Unification, simplification, and observations*, IEEE transaction on aerospace and electronic systems, Vol. 29, NO. 4 (Oct.1993).

[23] L.T. Nguyen, A. Belouchrani, K. Abed-Meraim, and B. Boashash, *Separation of more sources than sensors using time-frequency distributions*, International symposium on signal processing and its applications, Kuala Lumpur, Malaysia (Aug. 2001).

[24] S. Peleg and B. Friedlander, *Multicomponent signal analysis using the polynomial-phase transform*, IEEE Trans. Aerosp. Electron. Syst., vol.32, pp. 378387 (1996).

[25] A.W. Rihaczek, *Principles of high-resolution radar*, Boca Raton, FL: Peninsula, 1985.

[26] R.O. schmidt, *Multiple emitter location and signal parameter estimation*, IEEE transaction on antennas and propagation, Vol. AP-34, NO. 3 (Mar.1986).

[27] P. Stoica and A. Nehorai, *Mode, maximum likelihood and cramer-rao bound: conditional and unconditional results*, Report No. 891, Center for Systems Science, Yale University, New Haven, CT (Jan. 1989).

[28] M.R. Winkler, *Chirp signals for communications*, WESCON convention record, Paper 14.2 (1962).

[29] Y. Zhang and M.G. Amin, *Spatial averaging of time-frequency ditribution for signal recovery in uniform linear arrays*, IEEE Trans. SP, vol. 48, no. 10, pp. 2892-2902 (2001).

[30] ———, *Blind separation of sources based on their time-frequency signatures*, In proceedings ICASSP, Istanbul, Turkey (Jun. 2000).

[31] Y. Zhang, W. Mu, and M.G. Amin, *Subspace analysis of spatial time-frequency distribution matrices*, IEEE transaction on signal processing, Vol.49, NO. 4 (Apr. 2001).

[32] ———, *Time-frequency maximum likelihood methods for direction finding*, Journal of Franklin Institute. Vol. 337(4), pp. 483-497 (Jul. 2000).

[33] ———, *Bilinear signal synthesis in array processing*, in Proceedings of ICCASP'2001, Salt Lake, UT, pp. 3577-3580 (May. 2001).

[34] A.M. Zoubir and B. Boashash, *The bootstrap and its application in signal processing*, IEEE signal processing magazine (Jan. 1998).